

Dirac Monopoles Embedded in $SU(N)$ Gauge Theory with the θ Term

M. A. Zubkov

Institute of Theoretical and Experimental Physics, ul. Bol'shaya Cheremushkinskaya 25, Moscow, 117259 Russia

e-mail: zubkov@itep.ru

Received October 1, 2002

Dirac monopoles embedded in $SU(N)$ gauge theory with the θ term are considered. For $\theta = 4\pi M$ (where M is half-integer and integer for $N = 2$ and $N > 2$, respectively), these monopoles acquire an $SU(N)$ charge due to the θ term and become dyons. They belong to various (but not any) irreducible representations of the $SU(N)$ group. The admissible representations are listed. Their minimum dimension increases with N . The basic result of the study is the representation of the partition function of any $SU(N)$ model involving the θ term and complemented by singular gauge fields corresponding to the indicated monopoles in the form of a vacuum average of the product of Wilson loops viewed along the world lines of the monopoles. This vacuum average must be calculated in the corresponding model without the θ term. © 2002 MAIK "Nauka/Interperiodica".

PACS numbers: 11.15.-q; 14.80.Hv; 12.10.-g; 02.20.Qs

The concept of monopole proposed by Dirac [1] was originally associated with singular field configurations in electrodynamics, which have a magnetic charge due to the presence of a singularity. The self-energy of Dirac monopoles in $U(1)$ gauge theory diverges, which hinders their physical interpretation.

In non-Abelian gauge theories, monopoles first appear as solutions of the classical equations of motion in a model involving the scalar product from the adjoint representation of the gauge group [2]. These objects are referred to as t'Hooft–Polyakov monopoles and are associated with the regular configurations of the gauge field that carry finite energy. Nevertheless, t'Hooft–Polyakov monopoles retain many properties of Dirac monopoles that are primarily related to the quantization of the magnetic charge.

More recently, similar objects were found in many models (see, e.g., [3]). Quantum objects corresponding to these solutions to the classical equations of motion are topological defects, i.e., topologically nontrivial field configurations. In a particular case of a topological defect whose position is time-independent, the solution to the classical equations of motion, which are considered in the space with "cut" trajectory of the monopole and topologically nontrivial boundary conditions, reproduces the classical monopole solution. In this way, Dirac monopoles arise from the topological defects of the $U(1)$ gauge theory [4], and t'Hooft–Polyakov monopoles arise from the topological defects of the Georgi–Glashow model. In what follows, both the solution to the classical equations of motion and the corresponding topological defect will be referred to as monopole. We note that two-dimensional objects can

be considered similarly. In particular, Abrikosov–Nielsen–Olesen strings correspond to quantum topological defects of the Abelian Higgs model [5].

According to topological concepts, classical monopole solutions are absent in pure $SU(N)$ gauge theory. However, in view of analysis of the confinement mechanism in Abelian projections of gluodynamics and phenomena in the model of electroweak interactions at finite temperature, interest in topological objects of other models that are embedded in non-Abelian gauge theory arose recently [6]. We note that embedded monopoles, in contrast to "true" monopoles, are unstable in most cases [6, 7]. Nevertheless, their relation to dynamics is very substantial. In particular, their behavior in lattice electroweak theory at finite temperature is associated with the nature of electroweak phase transition [8]. After the fixation of the Abelian projection in gluodynamics, monopoles corresponding to the $U(1)^{N-1}$ residual symmetry group [9] are responsible for confinement [10]. We note that there are fundamentally different methods of embedding Abelian monopoles in a non-Abelian model. The distinction is in the method used to extract Abelian variables from $SU(N)$ fields.

More than 20 years ago, considering a model with an additional scalar field in the semiclassical approximation, Witten showed that t'Hooft–Polyakov monopoles in gauge theory with the θ term become dyons [11].

In this study, the effect of the θ term on the dynamics of quantum monopoles is analyzed for pure $SU(N)$ gauge theory by considering a direct generalization of the Dirac construction to $SU(N)$ gauge theory. Objects arising in such a way are Dirac monopoles correspond-

ing to the factors of the $U(1)^{N-1}$ group that are definitely embedded in $SU(N)$ gauge theory. The problems of their possible instability and divergence of self-energy are beyond the scope of this study. (Some remarks on these problems are discussed in the conclusion of this work.)

It is shown that monopoles thus defined are charged with respect to the $SU(N)$ group and belong to its various irreducible representations. It is remarkable that the θ term is “seen” only in that part of this construction which imparts the $SU(N)$ charge to monopoles. The topological part associated with the behavior of fields at infinity and proportional to the integer number of instantons vanishes in the partition function for those θ values for which the θ term imparts an integer $SU(N)$ charge to monopoles. More exactly, the partition function of any theory including the θ term and configurations corresponding to the constructed monopoles (and not including other singular gauge fields) is equal in the theory without the θ term to the vacuum average of the product of Wilson loops corresponding to monopole lines. Wilson loops are considered in those irreducible $SU(N)$ -group representations whose Young tableaux are uniquely determined by the form of the corresponding singularities of the field along the world lines of monopoles.

In this study, the definition of embedded monopoles will differ from the definition of monopoles with even Q_m [12]. The latter monopoles can be treated as arising under the application of a certain singular gauge transformation. As will be seen below, this is not the case for the gauge-field singularities considered here.

Dirac monopoles in four-dimensional $U(1)$ gauge theory (treated as topological defects) are defined as follows [4]. Let A_i be the gauge field that has strength F_{ij} and can have a singularity along surface Σ whose boundary is the world line of a Dirac monopole. The field strength is determined by the expression

$$i \int_s F_{\mu\nu}(y) dx^\mu dx^\nu = \exp\left(i \int_{\partial s} A dx_i\right) - 1, \quad (1)$$

where s is an infinitesimal area and the translation operator is defined along the boundary of this area ($y \in \partial s$). At points where A is regular, $F_{ij} = \partial_{[i} A_{j]}$, whereas this expression along surface Σ is distorted by the subtraction of the singularity corresponding to the Dirac string. In a certain gauge, the field corresponding to the world line of the monopole j and its Dirac string Σ is represented as $A^i = \bar{A}^i + A_s^i[\Sigma]$, where \bar{A} is the regular part of the gauge field and

$$A_s^i = \frac{1}{2} \epsilon^{ijkl} \Delta^{-1} \partial^j \Omega^{kl} 2\pi. \quad (2)$$

Here,

$$\Omega^{ij}(x) = \int_\Sigma \epsilon_{\alpha\beta} \frac{\partial z^i(\tau)}{\partial \tau_\alpha} \frac{\partial z^j(\sigma)}{\partial \tau_\beta} \delta(x - z(\tau)) d^2\tau,$$

where the points z of integration surface Σ are parameterized by the variable τ_α , $\alpha = 1, 2$; $z = z(\tau)$.

The field strength corresponding to this field configuration is equal to $F^{ij} = \partial^i A^j - \pi \epsilon^{ijkl} \Omega^{kl}$. The singularity of $\partial_{[i} A_{j]}$ along Σ cancels with the term involving Ω . Thus, the strength is singular only along the boundary of this surface.

Such singular gauge fields satisfy the identity

$$\partial^i (*F)^{ik} = 2\pi \mathcal{F}^k, \quad (3)$$

where

$$(*F)^{ik} = \frac{1}{2} \epsilon^{iklm} F^{lm}, \quad \mathcal{F}^k = \int_j \frac{dz^k}{ds} \delta(x - z(s)) ds.$$

(The points $z(s)$ of the monopole world line j are parameterized by variable s .) Expression (3) shows that the indicated singular configurations are actually Dirac monopoles, because \mathcal{F} is the magnetic current and $*F$ is the tensor dual to the field strength.

For generalizing this construction to the $SU(N)$ theory, we begin with the generalization of identity (3) to the non-Abelian case. We consider $SU(N)$ gauge theory in the 4-dimensional Euclidean space and denote the gauge field as $A_i = A_i^b T_b \in su(N)$, where the generators T_b ($b = 1, \dots, N^2 - 1$) of the $su(N)$ algebra are normalized by the condition $\text{Tr} T_b^2 = 1$. The strength R_{ij} of regular fields A is equal to $\partial_{[i} A_{j]} + i[A_i, A_j]$. Similar to the Abelian case, the definition of the strength of a field involving a singularity along a certain two-dimensional surface is based on the expression $i \int_s R_{\mu\nu}(y) dx^\mu dx^\nu = \text{Pexp}(i \int_{\partial s} A_i dx_i) - 1$, where s is the infinitesimal area and the translation operator is defined along the boundary of this area.

Regular fields satisfy the Bianchi identity $\partial^i (*R)^{ik} + i[A^i, (*R)^{ik}] = 0$, where $(*R)^{ik} = \frac{1}{2} \epsilon^{iklm} R^{lm}$, which is similar to the Abelian identity $\partial^i (*F)^{ik} = 0$. It can be modified to the form involving the monopole current in the case, where fields are singular and the definition of the gauge-field strength is appropriately modified.

Thus, our aim is to find field- A configurations whose strength satisfies the anomalous Bianchi identity

$$\partial^i (*R)^{ik} + i[A^i, (*R)^{ik}] = 2\pi \mathcal{F}^k \mathbf{n}, \quad (4)$$

where the matrix \mathbf{n} is an element of the $SU(N)$ algebra and transformed under the gauge transformations g as $\mathbf{n} \rightarrow g\mathbf{n}g^+$. If j has no self-intersections, one can always choose a gauge in which \mathbf{n} is a Cartan element. Therefore, monopoles determined by Eq. (4) are Abelian. They must correspond to the $U(1)^{N-1}$ -group factors, whose generators are Cartan elements of the $SU(N)$ algebra, and must be, therefore, Dirac monopoles embedded in $SU(N)$ gauge theory.

Below, we present the construction of such objects. Similar to $U(1)$ monopoles, they arise under the assumption that the gauge field can be singular along surface Σ , whereas the field strength R can be singular only along the boundary j (the world line of the monopole) of this surface. Both j and Σ are supposed to be smooth and free of self-intersections.

Let S_1 be an infinitesimal circle that has radius r and intersects Σ . This circle lies in the plane orthogonal to Σ and intersects Σ at the center of the circle. Gauge transformations can reduce fields along all such circles to the diagonal form

$$A^i s^i = \mathbf{A}\mathbf{n}, \quad (5)$$

where $\mathbf{A} \in R$ and \mathbf{n} is the diagonal matrix, both these quantities being independent of their positions in S_1 , and s^i are the components of unit vector directed along S_1 . The regularity of the field strength in Σ leads to the condition $P \exp(i \int_{S_1} A^i dx^i) = 1$, which is satisfied if the field A behaves as

$$\mathbf{A} \sim 1/r \quad (6)$$

for $r \rightarrow 0$. In this case, the diagonal elements n_i of matrix \mathbf{n} must be integer.

We consider field configurations such that the field in other directions is regular in Σ . Surface Σ generally consists of several parts, each corresponding to its own \mathbf{n} . We can write the symbolic equality $\Sigma = \sum_n \Sigma_n$.

Let us consider the plane (ij) such that (i) and (j) are directed along S_1 and Σ , respectively. Then the requirement for the regularity of R leads to the equation

$$[A_k, \mathbf{n}] = 0 \quad (7)$$

on Σ . Equation (7) shows that fields are effectively Abelian along Σ . In what follows, we will assume that this requirement extends to the Σ boundary. This additional requirement is very stringent. Due to it, the commutator cannot contain any singularity that could cancel the monopole singularity corresponding to the monopole in the Abelian part of field strength and leading to the anomalous Bianchi identity given by Eq. (4).

We arrive at the definition of singular gauge field corresponding a $U(1)^{N-1}$ topological defect embedded

in $SU(N)$ theory. Similar to the $U(1)$ case, this field can be represented in the form

$$A^i = \bar{A}^i + \sum_n A_s^i[\Sigma_n]\mathbf{n}, \quad (8)$$

where the gauge is fixed so that Eq. (5) is valid, \bar{A} is the regular part of the gauge field, and $A_s(\Sigma_n)$ is given by Eq. (2).

The monopoles under consideration are determined by Eq. (8) and additional condition (7) in a gauge where fields in all infinitesimal circles intersecting surface Σ are diagonal. A direct check shows that such configurations cannot be obtained from regular fields by any gauge transformations including singular ones.

Taking Eq. (7) into account, we can represent the field strength corresponding to such a field configuration in the form

$$R^{ij} = \partial^{[i} A^{j]} + i[A^i, A^j] - \pi \epsilon^{ijkl} \Omega^{kl} \mathbf{n}. \quad (9)$$

Similar to the Abelian case, the singularity $\partial_{[i} A_{j]} + i[A_i, A_j]$ along Σ cancels with the term involving Ω . A direct calculation shows that the singular gauge fields given by Eq. (8) satisfy Bianchi identity (4).

Now, we can consider the effect of the θ term on the dynamics of the monopoles constructed above. We have

$$\begin{aligned} Q &= \frac{1}{32\pi^2} \int d^4x \epsilon_{\mu\nu\rho\sigma} \text{Tr} R_{\mu\nu} R_{\rho\sigma} \\ &= \frac{1}{16\pi^2} \int d^4x \text{Tr} G^* G - \frac{1}{4\pi} \int_{\Sigma} d^2\tau \text{Tr} G_{ij} \mathbf{n} t_{ij}, \end{aligned} \quad (10)$$

where

$$G_{ij} = \partial_{[i} A_{j]} + i[A_i, A_j], \quad t^{ij} = \epsilon_{\alpha\beta} \frac{\partial z^i(\tau)}{\partial \tau_\alpha} \frac{\partial z^j(\sigma)}{\partial \tau_\beta}.$$

Using Eq. (7), we obtain $\text{Tr}[A_i, A_j]\mathbf{n} = 0$. Therefore,

$$Q = \frac{1}{16\pi^2} \int d^4x \text{Tr} G^* G - \frac{1}{4\pi} \int_j dx_i \text{Tr} A_i \mathbf{n}. \quad (11)$$

A thorough analysis of the regularization of the first term in Eq. (11) indicates that it depends only on A values at infinity. Assuming that the field strength vanishes at infinity, we conclude that this term is nothing else but the integer number of instantons. Thus,

$$\exp(4\pi M i Q) = \exp\left(-i \sum_n \int_{j_n} dx_i M \text{Tr} A_i^{g[A, \Sigma]} \mathbf{n}\right) \quad (12)$$

for integer and half-integer M , where $g[A, \Sigma]$ is the transformation modifying A to Eq. (5) along Σ .

We consider an arbitrary $SU(N)$ model with regular fields and artificially supplement it with the monopole singularities indicated above. In this case, the partition function of the theory with added monopole singularities in the presence of the θ term can be expressed as a vacuum average of $\exp(i\theta Q)$ in the corresponding $SU(N)$ theory without θ term. For $\theta = 4\pi M$, we obtain

$$Z = \langle \exp(4\pi M i Q) \rangle = \left\langle \prod_{\mathbf{n}} \exp \left(-i \int_{j_n} dx_i M \text{Tr} A_i^{g[A, \Sigma]} \mathbf{n} \right) \right\rangle. \tag{13}$$

Below, we will use the following Abelian representation for the world line [13]:

$$\mathbf{W}_{[q]}[j] = \int Dg \exp \left(i \int_j dx_i \text{Tr} [A^g]_i \mathcal{H}^{[q]} \right). \tag{14}$$

Here, $\mathcal{H}^q = \sum_i m_i \mathbf{H}_i$, where m_i is the highest weight of the corresponding representation and \mathbf{H}_i is the definitely normalized basis of the Cartan elements of $SU(N)$ algebra. The Wilson loop $\mathbf{W}_q[j]$ is considered in the irreducible representation of the $SU(N)$ group. The space of this representation consists of tensors $\Psi_{i_1 i_2 \dots i_r}$, whose symmetry with respect to the index permutation is determined by a set of integers (describing the Young tableau) q_i ($i = 1, \dots, N - 1$) ($\sum_i q_i = r, q_i \geq 0$).

A direct calculation yields nonzero elements of the diagonal matrix \mathcal{H}^q in the form ($q_N = 0$)

$$\mathcal{H}_{ii}^q = q_i - \frac{1}{N} \sum_k q_k \quad (i = 1, \dots, N). \tag{15}$$

We can introduce the correspondence between any matrix $\mathbf{n} = \text{diag}(n_1, \dots, n_N)$ defined in the world line of the monopole and the $SU(N)$ -group representation as follows. Let the elements n_i be ordered such that $n_N \geq n_{N-1} \geq \dots \geq n_1$. The corresponding representation of the group is determined by the set of numbers

$$q_i(\mathbf{n}) = M(n_N - n_i). \tag{16}$$

This representation is denoted as $[q(\mathbf{n})]$. In this case, $\mathcal{H}^{[q(\mathbf{n})]}$ coincides with $-M\mathbf{n}$ except for the permutation of elements. As a result,

$$Z = \langle \exp(4\pi i M Q) \rangle = \langle \prod_{\mathbf{n}} \mathbf{W}_{[q(\mathbf{n})]}[j_{\mathbf{n}}] \rangle, \tag{17}$$

where the monopole world line $j_{\mathbf{n}}$ carries matrix \mathbf{n} . For q to be an integer, M must generally be an integer. However, σ_3 is the only Cartan element in the $SU(2)$ group. Therefore, $q = M \text{Tr}(\mathbf{n} \sigma_3)$ is an integer for any half-integer M . For this reason, we consider here $\theta = 4\pi M$, where M is a half-integer and integer for $N = 2$ and $N > 2$, respectively.

Expression (17) indicates that monopoles become dyons. An interesting feature of this expression is that the topological term does not enter into the partition function. The only meaning of this term in this case is that monopoles become charged with respect to the gauge group.

Expression (17) can include only certain representations that are determined by sets (q_1, \dots, q_{N-1}) such that $\sum_i q_i = NML$, where L is an integer. In particular, the complete set of irreducible representations of the $SU(2)$ group is admissible for $N = 2$ and $M = 1/2$. The lowest admissible representations for $N = 3$ and $M = 1$ are $(3, 0), (2, 1), (6, 0), (5, 1), (4, 2), \dots$. The lowest admissible symmetric representation for the $SU(5)$ group is $(5, 0, 0, 0)$.

Thus, our analysis of Dirac monopoles embedded in the $SU(N)$ gauge theory with the θ term has demonstrated that these monopoles are dyons. It was shown that the partition function of the theory with artificially introduced Abelian monopole singularities can be expressed as a vacuum average of Wilson loops corresponding to the world lines of monopoles, which is determined in theory without the θ term. This expression involves an infinite set of irreducible representations of the gauge group. An interesting feature of the theory is that the topological term does not enter into the partition function. Another surprising result is that the lowest dimension of representations thus appearing increases with N .

As was mentioned above, we treated monopole singularities as external ones and artificially introduced them into the functional integral. At the current level of understanding, we cannot consider these objects as arising dynamically, because (similar to the case of the Dirac monopole) we did not determine a model where the corresponding singularity of the gauge field led to the finite action. Moreover, arguments presented in [12] indicates that such configurations can be unstable. However, we note that many properties of unreal (from the standpoint of Abelian theories) Dirac monopoles proved to be inherent in objects with finite energy, namely, in t'Hooft–Polyakov monopoles arising in a more complex model. Similarly, the properties of the above-analyzed Dirac monopoles embedded in $SU(N)$ theory with the θ term can likely be inherent in realistic objects of a certain more complex physical model.

I am grateful to M.I. Polikarpov, V.I. Zakharov, and F.V. Gubarev for stimulating discussions. This work was supported by INTAS (project no. 00-00111) and the U.S. Civilian Research and Development Foundation for the Independent States of the former Soviet Union (grant no. RP1-2364-MO-02).

REFERENCES

1. P. A. M. Dirac, Proc. R. Soc. London, Ser. A **133**, 60 (1931).

2. A. M. Polyakov, Pis'ma Zh. Éksp. Teor. Fiz. **20**, 430 (1974) [JETP Lett. **20**, 194 (1974)].
3. *Monopoles. Topological and Variation Methods*, Ed. by M. I. Monastyrskii and A. G. Sergeev (Mir, Moscow, 1989).
4. A. M. Polyakov, *Gauge Fields and Strings* (Harwood Academic, Chur, Switzerland, 1987).
5. M. I. Polikarpov, U. J. Wiese, and M. A. Zubkov, Phys. Lett. B **309**, 133 (1993).
6. M. Barriola, T. Vachaspati, and M. Bucher, Phys. Rev. D **50**, 2819 (1994).
7. R. A. Brandt and F. Neri, Nucl. Phys. B **161**, 253 (1979).
8. M. N. Chernodub, F. V. Gubarev, E. M. Ilgenfritz, *et al.*, Phys. Lett. B **434**, 83 (1998).
9. G. t'Hooft, Nucl. Phys. B **190**, 455 (1981).
10. M. I. Polikarpov, Nucl. Phys. (Proc. Suppl.) **53**, 134 (1997).
11. E. Witten, Phys. Lett. B **86B**, 283 (1979).
12. M. N. Chernodub, F. V. Gubarev, M. I. Polikarpov, *et al.*, Nucl. Phys. B **592**, 107 (2001).
13. D. Diakonov and V. Petrov, Phys. Lett. B **224**, 131 (1989).

Translated by R. Tyapaev

Operationalistic Orthogonality Condition for Single-Mode Biphotons (Qutrits)

A. A. Zhukov, G. A. Maslennikov, and M. V. Chekhova

Moscow State University, Vorob'evy gory, Moscow, 119899 Russia

e-mail: postmast@qopt.phys.msu.su

Received October 24, 2002

An arbitrary polarization state of a single-mode biphoton is considered. The operationalistic criterion is formulated for the orthogonality of these states. It can be used to separate a biphoton with an arbitrary degree of polarization from a set of biphotons orthogonal to it. This is necessary for the implementation of quantum cryptography protocol based on the three-level systems. The experimental test of this criterion amounts to the observation of the anticorrelation effect for a biphoton with an arbitrary polarization state. © 2002 MAIK "Nauka/Interperiodica".

PACS numbers: 03.67.Hk; 42.25.Ja; 42.50.Dv

In recent years, considerable interest has been shown in multilevel systems with dimensionality higher than two, because they provide a way for more dense data recording, as compared to the traditional two-level systems. This is particularly important for quantum cryptography, because it enables one to increase the data-exchange rate [1] and enhance security against eavesdropping attacks of a certain class [2]. However, the transition to higher-dimensionality systems inevitably gives rise to experimental difficulties associated with the implementation and the adequate measurement of parameters. The solution of these problems requires the design of a data output device, error-correction protocols, repeaters, and other quantum communication devices. After the two-level system, the three-level system is the simplest. Its state in quantum information is called "qutrit" by analogy with qubit. The wave function of an arbitrary three-level system can be written as

$$\Psi = c_1|1\rangle + c_2|2\rangle + c_3|3\rangle, \quad (1)$$

where $|1\rangle$, $|2\rangle$, and $|3\rangle$ are the orthogonal basis states. The complex coefficients c_i are called the amplitudes of basis states $|i\rangle$ and related to each other by the normalization condition

$$\sum_{i=1}^3 |c_i|^2 = 1. \quad (2)$$

At present, the use of qutrits in quantum information is not an exotic thing. For example, the authors of [3] have proposed a quantum cryptography protocol based on the three-level systems, and the interferometric method of preparing multilevel systems was considered in [1]. The theoretical analysis of state restoration from the

measured quantities was carried out for an arbitrary multilevel system in [4].

Biphoton fields have been used in many experiments of quantum optics practically since its inception. These fields are fluxes of photon pairs strongly correlated in coordinate and time of their creation. In the great majority of experiments, spontaneous parametric down-conversion (SPDC) is used as a source of biphoton field. It will be shown below that, in the case where a photon pair is emitted into the same spatial and frequency mode, the state polarization characteristics of the biphoton allow it to be considered as a qutrit [5]. The use of single-mode biphotons as qutrits in quantum communication protocols, e.g., in quantum cryptography poses the problem of separating a certain biphoton from the subset of biphotons with polarizations orthogonal to the polarization of the former. In this work, the operationalistic biphoton orthogonality condition is formulated for an arbitrary degree of polarization, and the experimental scheme is proposed that allows unambiguous separation of a certain biphoton polarization state from a set of states orthogonal to it. This is a fundamental problem, and its solution can be used, e.g., in the practical implementation of quantum cryptography protocol for the three-level systems.

Biphotons and qutrits. The use of the polarization states of single-mode biphotons for data recording was proposed in [5], and the polarization characteristics of these fields were discussed in [6, 7]. A pure polarization state of a biphoton in the collinear frequency-degenerate regime can be written as [5]

$$|\Psi\rangle = c_1|2, 0\rangle + c_2|1, 1\rangle + c_3|0, 2\rangle. \quad (3)$$

Here, $|n, m\rangle$ denote the state with n photons in the horizontal (H) polarization mode and m photons in the vertical (V) mode ($n + m = 2$) and $c_i = |c_i|\exp(i\phi_i)$ is the

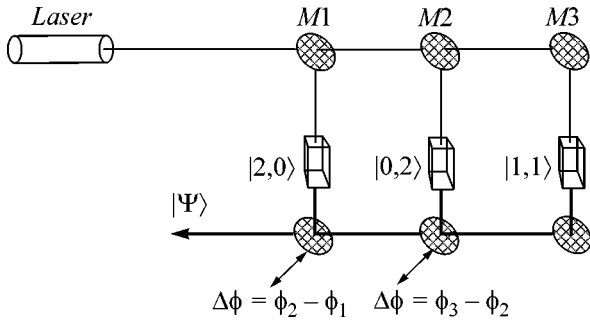


Fig. 1. Scheme of a nonlinear three-arm Mach-Zehnder interferometer. Nonlinear crystals oriented so as to produce the appropriate state are placed in each of the arms. By introducing (with the use of mirrors) phase difference between the states, one can change the phases of coefficients c_i in the desired way and, by varying the pump power, one can change their amplitudes in a desired way. Mirrors are denoted by $M1$, $M2$, and $M3$.

complex amplitude of the probability of finding biphoton in the corresponding state. The states $|2, 0\rangle$, $|1, 1\rangle$, and $|0, 2\rangle$ constitute the orthogonal basis set in so-called HV representation. By analogy with Eq. (1), this state can be used for the ternary information coding. To visualize the polarization states of a biphoton light, it is convenient to use the Poincaré sphere [7]. One can show that state vector (3) can be represented as

$$|\Psi\rangle = \frac{a^\dagger(\vartheta, \varphi)a^\dagger(\vartheta', \varphi')|\text{vac}\rangle}{\|a^\dagger(\vartheta, \varphi)a^\dagger(\vartheta', \varphi')|\text{vac}\rangle\|}, \quad (3a)$$

where $a^\dagger(\vartheta, \varphi)$ and $a^\dagger(\vartheta', \varphi')$ are the operators of photon creation and annihilation in an arbitrary polarization mode, e.g.,

$$a^\dagger(\vartheta, \varphi) = \cos \frac{\vartheta}{2} a_H^\dagger + e^{i\varphi} \sin \frac{\vartheta}{2} a_V^\dagger,$$

where $a_{H,V}^\dagger$ are the operators of photon creation in the linear polarization modes H and V , and $\varphi, \varphi' \in [0, 2\pi]$ and $\vartheta, \vartheta' \in [0, \pi]$ are, respectively, the azimuthal and polar angles on the Poincaré sphere. In this case,

$$\begin{aligned} \varphi, \varphi' &= \frac{\varphi_3}{2} \pm \frac{1}{2} \arccos \left[\frac{|c_2|^2}{2|c_1||c_3|} \right. \\ &\quad \left. - \sqrt{1 + \frac{|c_2|^4}{4|c_1|^2|c_3|^2} - \frac{|c_2|^2}{|c_1||c_3|} \cos(2\varphi_2 - \varphi_3)} \right], \\ \theta, \theta' &= \arccos \{ [|c_1|^2 - |c_3|^2 \\ &\quad \pm 2\sqrt{[|c_2|^2 - |c_1||c_3| \cos(2\varphi - \varphi_3)]^2 - |c_1|^2|c_3|^2}] \\ &\quad \times [1 + |c_2|^2 - 2|c_1||c_3| \cos(2\varphi - \varphi_3)]^{-1} \}, \end{aligned}$$

where the unprimed and primed quantities relate, respectively, to the first and the second photon of the

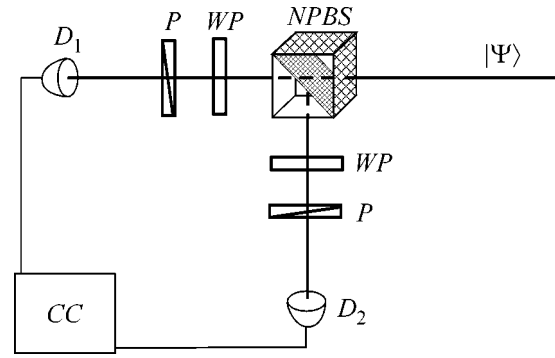


Fig. 2. Scheme for measuring arbitrary polarization state of a biphoton field. $NPBS$ is the nonpolarizing beam splitter, WP is a set of wave plates, P is the analyzer, D is a single-photon detector, and CC is the coincidence counting scheme.

pair. It is also convenient to introduce the degree of biphoton polarization. This quantity was calculated in [6] and, in the new representation, takes the form

$$P = \frac{2 \cos(\alpha/2)}{1 + \cos^2(\alpha/2)},$$

where α is the angle at which the pair of points mapping biphoton onto the Poincaré sphere is seen from its center.

The generation of a biphoton field in an arbitrary polarization state with given coefficients c_i can be accomplished in a three-arm interferometer of the Mach-Zehnder type with three nonlinear crystals. Each of them produces one of the basis states in the corresponding arm to prepare a linear superposition of type (3) at the output. The amplitudes and phases of the complex coefficients c_i can be varied in a desired way in each of the arms (Fig. 1). In particular, all states used in the quantum cryptography protocol proposed in [3] can be prepared in the interferometer of this type.

To adequately measure the polarization characteristics of single-mode biphoton fields, the Braun-Twiss scheme is used with arbitrary polarizing filters in the arms (Fig. 2). Each filter includes a polarization transformer and a linear polarization analyzer to separate a certain polarization state. Upon measuring a certain set of fourth-order field moments in this scheme, one can determine the real and imaginary parts of coefficients c_i by varying the transformer characteristics. For some pure states $|\Psi\rangle$ this was done in [8]. However, this scheme can be used to measure an arbitrary polarization state of biphoton field in the HV basis. We will refer to the measuring scheme as “tuned” to the particular polarization biphoton state (3a) if the polarization state with parameters (ϑ, φ) is separated in one channel and the state with parameters (ϑ', φ') in the other.

Orthogonality of single-mode biphotons. Assume that the polarization states corresponding to modes a_1 and b_2 (letters denote the polarization states and index denotes the spatial mode) are separated in channels 1 and 2 of a device illustrated in Fig. 2. Let us write the orthogonality condition for a certain input state $|\Psi_{cd}\rangle$ and the state $|\Psi_{ab}\rangle$ to which the detector device is tuned. Let

$$|\Psi_{ab}\rangle = \frac{a^\dagger b^\dagger |\text{vac}\rangle}{\|a^\dagger b^\dagger |\text{vac}\rangle\|}, \quad |\Psi_{cd}\rangle = \frac{c^\dagger d^\dagger |\text{vac}\rangle}{\|c^\dagger d^\dagger |\text{vac}\rangle\|},$$

where $a^\dagger, b^\dagger, c^\dagger,$ and d^\dagger are the creation operators for the polarization modes $a, b, c,$ and $d,$ respectively. We emphasize that, in the general case, the modes $a, b, c,$ and d are not mutually orthogonal. The condition for the orthogonality of the input biphoton and the biphoton to which the device is tuned has the form

$$\langle \Psi_{ab} | \Psi_{cd} \rangle = 0$$

or, equivalently,

$$\langle \text{vac} | abc^\dagger d^\dagger | \text{vac} \rangle = 0. \quad (4)$$

Since the creation and annihilation operators before and after a 50% beam splitter are related to each other as $a^\dagger = \frac{1}{\sqrt{2}}(a_1^\dagger + ia_2^\dagger)$, Eq. (4) can be rewritten as

$$\langle \text{vac} | (a_1 - ia_2)(b_1 - ib_2)(c_1^\dagger + ic_2^\dagger)(d_1^\dagger + id_2^\dagger) | \text{vac} \rangle = 0. \quad (5)$$

Neglecting the terms $\langle \text{vac} | a_i b_j c_i^\dagger d_j^\dagger | \text{vac} \rangle$, which are equal to zero according to Eq. (4), and the terms of the form $\langle \text{vac} | a_i b_j c_j^\dagger d_i^\dagger | \text{vac} \rangle$, which are also equal to zero because they correspond to the creation of a photon pair in the mode j and annihilation of a photon pair in the mode i , etc., one gets

$$\begin{aligned} & \langle \text{vac} | a_1 b_2 (c_1^\dagger d_2^\dagger + c_2^\dagger d_1^\dagger) \\ & + a_2 b_1 (c_1^\dagger d_2^\dagger + c_2^\dagger d_1^\dagger) | \text{vac} \rangle = 0. \end{aligned} \quad (6)$$

Note that

$$\begin{aligned} & \langle \text{vac} | a_1 b_2 (c_1^\dagger d_2^\dagger + c_2^\dagger d_1^\dagger) | \text{vac} \rangle \\ & = \langle |a_1 c_1^\dagger\rangle \langle |b_2 d_2^\dagger\rangle + \langle |a_1 d_1^\dagger\rangle \langle |b_2 c_2^\dagger\rangle \\ & = \langle |ac^\dagger\rangle \langle |bd^\dagger\rangle + \langle |ad^\dagger\rangle \langle |bc^\dagger\rangle, \\ & \langle \text{vac} | a_2 b_1 (c_1^\dagger d_2^\dagger + c_2^\dagger d_1^\dagger) | \text{vac} \rangle \\ & = \langle |a_2 c_2^\dagger\rangle \langle |b_1 d_1^\dagger\rangle + \langle |a_2 d_2^\dagger\rangle \langle |b_1 c_1^\dagger\rangle \\ & = \langle |ac^\dagger\rangle \langle |bd^\dagger\rangle + \langle |ad^\dagger\rangle \langle |bc^\dagger\rangle; \end{aligned}$$

i.e., the mean values of both terms in Eq. (6) are equal, because they differ only in the spatial indices and, hence,

$$\langle \text{vac} | a_1 b_2 (c_1^\dagger d_2^\dagger + c_2^\dagger d_1^\dagger) | \text{vac} \rangle = 0. \quad (7)$$

Note that the state vectors of the form $a_i b_j c_i^\dagger d_j^\dagger | \text{vac} \rangle$ in Eq. (7) contain two creation and two annihilation operators; hence, their sum is a vacuum state multiplied by a numerical factor. It follows from Eq. (7) that this factor is zero. Therefore, the orthogonality condition for the biphotons $|\Psi_{ab}\rangle$ and $|\Psi_{cd}\rangle$ finally takes the form

$$a_1 b_2 (c_1^\dagger d_2^\dagger + c_2^\dagger d_1^\dagger) | \text{vac} \rangle = 0. \quad (8)$$

After the beam splitter, the input state $|\Psi_{cd}\rangle$ becomes

$$\begin{aligned} |\Psi'_{cd}\rangle &= \frac{i}{2\|c^\dagger d^\dagger |\text{vac}\rangle\|} \\ &\times \{c_1^\dagger d_2^\dagger + d_1^\dagger c_2^\dagger + c_1^\dagger d_1^\dagger + c_2^\dagger d_2^\dagger\} | \text{vac} \rangle. \end{aligned}$$

The last two terms make no contribution to the coincidences, because they correspond to the situation where both photons are led to the same photodetector. For this reason, the coincidence counting rate is determined by the second-order correlation function

$$G^{(2)} = \frac{1}{4\|c^\dagger d^\dagger |\text{vac}\rangle\|^2} \quad (9)$$

$$\times \langle \text{vac} | \{c_1 d_2 + d_1 c_2\} a_1^\dagger b_2^\dagger a_1 b_2 \{c_1^\dagger d_2^\dagger - d_1^\dagger c_2^\dagger\} | \text{vac} \rangle.$$

The absence of photocount coincidences for detectors D_1 and D_2 is equivalent to the zero value of the correlator in Eq. (9). The condition for the absence of coincidences can be written as

$$\langle \text{vac} | \{c_1 d_2 + d_1 c_2\} a_1^\dagger b_2^\dagger a_1 b_2 \{c_1^\dagger d_2^\dagger + d_1^\dagger c_2^\dagger\} | \text{vac} \rangle = 0, \quad (10)$$

which is equivalent to condition (8).

Therefore, the condition for the orthogonality of two biphotons is equivalent to the condition for the absence of coincidences in the scheme in Fig. 2, provided that one biphoton is fed into the input, while the device is tuned to the second biphoton. This procedure can be regarded as the projection of one polarization state onto the other, with the number of photocount coincidences playing the role of an observable quantity. In the case that the second state is orthogonal to the initial state, the coincidence counting rate should drop to the level of accidental coincidences. It should also be noted that the rate of single photocounts in both detectors will be, generally, nonzero upon changing the characteristics of polarization transformers, e.g., upon analyzer rotation. In this case, the character of changing the number of single photocounts takes the form of interference pattern with the visibility equal to the degree of polarization of a measured biphoton [9].

The experimental data [5] presented in the table illustrate the biphoton orthogonality criterion. For example, if the recording scheme is tuned to the $|H, V\rangle$ state, while the input state is $|R, L\rangle$ (a pair of right- and

Experimental dependence of the coincidence counting rate on the input polarization state of a biphoton and the state to which the device is tuned

Input state	Degree of polarization, P	Detected state	Degree of polarization, P	Coincidence counting rate (s^{-1})
$ H, V\rangle$	0	$ H, V\rangle$	0	4.0 ± 0.4
$ R, L\rangle$	0	$ H, V\rangle$	0	0.5 ± 0.25
$ D, \bar{D}\rangle$	0	$ H, V\rangle$	0	0.25 ± 0.1
$ H, V\rangle$	0	$ D, \bar{D}\rangle$	0	0.25 ± 0.1
$ D, \bar{D}\rangle$	0	$ D, \bar{D}\rangle$	0	3.8 ± 0.4
$ H, V\rangle$	0	$ H, H\rangle$	1	0.15 ± 0.05
$ D, \bar{D}\rangle$	0	$ H, H\rangle$	1	1.9 ± 0.2

Note: The following notation is used for the polarization modes: H is the horizontal direction of mode polarization; V is the vertical direction; D, \bar{D} is the linear polarization with angles of $+45^\circ$ and -45° to the vertical direction; and R and L are the right- and left-hand circular polarizations, respectively.

left-hand circularly polarized photons) or $|D\bar{D}\rangle$ (a pair of photons linearly polarized at $\pm 45^\circ$) is orthogonal to it, the coincidence counting rate is an order of magnitude lower than for the same input state $|H, V\rangle$. Likewise, a low coincidence counting rate is observed in the case where the input state is $|H, V\rangle$, while the device is tuned to the orthogonal state $|H, H\rangle$. At the same time, if the device is tuned to the $|H, H\rangle$ state and $|D\bar{D}\rangle$ is the input state, whose projection onto the $|H, H\rangle$ equals $1/\sqrt{2}$, the coincidence counting rate is half as high as for the case where the device is tuned to the input state.

Thus, the biphoton orthogonality criterion suggested in this work allows one to unambiguously separate a biphoton in an arbitrary polarization state from a set of biphotons orthogonal to it. The experimental test of this criterion amounts to the observation of anticorrelation [10, 11] for an arbitrary biphoton polarization state, in contrast to works [10, 11], where the directions of photon polarization in a pair were identical, or work [12], where they were mutually orthogonal.

In practice, this criterion can be used for the implementation of a quantum cryptography protocol [3]. The possibility of unambiguously separating the desired biphoton polarization state from a set of states orthog-

onal to it allows a certain logical value used in the secret key to be assigned to this biphoton with assurance. Nevertheless, this scheme is not free from losses. For instance, both photons in a pair may be led into the same arm after beam splitter and, hence, may make no contribution to the coincidences. These processes alone halve the amount of useful information. Another loss source appears because, despite the fact that the suggested scheme filters out only one biphoton $|\Psi_{cd}\rangle = c^\dagger d^\dagger |\text{vac}\rangle / \|c^\dagger d^\dagger |\text{vac}\rangle\|$ from a set of biphotons orthogonal to it, the probability that this biphoton will make no contribution at the output is nonzero even if the detectors are ideal. This may occur if a photon in mode c is led to the arm tuned to mode d , and vice versa. Clearly, since the modes c and d are generally different, each of these photons may not be detected separately and, as a result, no coincidence will occur.

We are grateful to S.P. Kulik and P.A. Prudkovskii for discussions. This work was supported by the Russian Foundation for Basic Research (project nos. 02-02-16664, 00-15-96541) and INTAS (grant no. 01-2122).

REFERENCES

1. H. Bechmann-Pasquinnucci and W. Tittel, Phys. Rev. A **61**, 062308 (2000).
2. D. Bruss and C. Machiavello, Phys. Rev. Lett. **88**, 127901 (2002).
3. H. Bechmann-Pasquinnucci and A. Peres, Phys. Rev. Lett. **85**, 3313 (2000).
4. R. T. Thew, K. Nemoto, A. G. White, and W. J. Munro, Phys. Rev. A **66**, 012303 (2002).
5. A. V. Burlakov, M. V. Chekhova, O. A. Karabutova, *et al.*, Phys. Rev. A **60**, 4209 (1999).
6. A. V. Burlakov and D. N. Klyshko, Pis'ma Zh. Éksp. Teor. Fiz. **69**, 795 (1999) [JETP Lett. **69**, 839 (1999)].
7. A. V. Burlakov and M. V. Chekhova, Pis'ma Zh. Éksp. Teor. Fiz. **75**, 505 (2002) [JETP Lett. **75**, 432 (2002)].
8. A. V. Burlakov, L. A. Krivitskiy, S. P. Kulik, *et al.*, e-print quant-ph/0207096 (17 Sept. 2002), Vol. 2.
9. D. N. Klyshko, Zh. Éksp. Teor. Fiz. **111**, 1955 (1997) [JETP **84**, 1065 (1997)].
10. C. K. Hong, Z. Y. Ou, and L. Mandel, Phys. Rev. Lett. **59**, 2044 (1987).
11. Y. H. Shih and C. O. Alley, Phys. Rev. Lett. **61**, 2921 (1988).
12. Y. H. Shih and A. V. Sergienko, Phys. Lett. A **186**, 29 (1994).

Translated by V. Sakun

On the Theory of X-ray Refractive Optics: Exact Solution for a Parabolic Medium

V. G. Kohn

Russian Research Centre Kurchatov Institute, pl. Kurchatova 1, Moscow, 123182 Russia

e-mail: kohn@kurm.polyn.kiae.su

Received October 24, 2002

The exact solution is obtained for a propagator describing x-ray propagation through a refractive parabolic medium. Such a medium arises in compound many-element refractive x-ray lenses that are used in synchrotron radiation sources. The solution obtained allows one to analyze such lenses in detail to predict their operation in particular applications (beam focusing, microobject imaging, and Fourier transform). © 2002 MAIK “Nauka/Interperiodica”.

PACS numbers: 41.50.+h; 07.85.Qe; 42.79.Bh; 42.30.-d

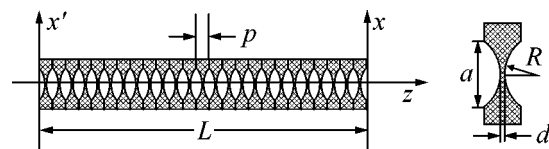
For a hundred years after the discovery of x-ray radiation, it was thought that refractive lenses could not be used for focusing hard x-rays because, at least, of two reasons. First, the refractive index for electromagnetic radiation with energy E ranging from 10 to 50 keV differs only slightly from unity. Second, the absorption coefficient for this radiation is nonzero. When writing the complex refractive index in the form $n = 1 - \delta + i\beta$, one has, e.g., for aluminum at $E = 25$ keV $\delta = 8.643 \times 10^{-7}$ and $\beta = 1.747 \times 10^{-9}$.

This problem was solved in 1996 [1] with the use of compound lenses, i.e., lenses composed of a large number of relatively thin elements. It proved to be quite fortunate that the x-ray phase velocity in a material is higher than the velocity of light in free space. For this reason, the focusing lens was taken to be biconcave and the thickness of a material in the central part of the lens was smaller than the absorption length. To date, many publications have been devoted to various methods of fabricating compound refractive x-ray lenses. Among them, of primary interest are lenses with circular aperture and parabolic profile. Elements of these prisms are obtained by pressing out parabolic profile in aluminum plates (see, e.g., [2]) or plates of organic materials (see, e.g., [3]). Each element focuses a parallel beam into the point at distance $F_1 = R/2\delta$, where R is the radius of curvature of the parabolic profile (see figure). In this case, the focal length of a block with N elements is $F \approx F_1/N$. Let, e.g., $F_1 = 100$ m. The focal length of a block with 100 elements will be 1 m, which is quite appropriate for the experiments at synchrotron radiation stations.

A lens containing 1000 or more elements can rather easily be fabricated. The length $L = Np$ of the compound lens increases with the number N of elements, while the focal length F decreases. Clearly, the focal length in the case $L \ll F$ can be estimated from the formula $F \approx R/2N\delta$ for a thin lens. However, in this case

the linear corrections in the small parameter L/F may be quite appreciable when imaging microobjects with extreme resolution. The theoretical analysis of the operation of a compound lens with length L comparable to the focal length F was performed only in the geometrical optics approximation (see, e.g., [4]), which is, clearly, insufficient for the estimation of focal spot size and for the analysis of image transfer using this lens.

A complete solution to the problem of radiation transfer through a long compound lens must have the form of an integral relationship of the Kirchhoff integral type. In this case, the problem amounts to determining the kernel of integral transformation (propagator) by solving the Maxwell equation with initial condition in the form of the Dirac delta function. It is shown in this work that, under certain conditions, this problem has an exact solution; i.e., the propagator can be calculated analytically in a form close to the Gaussian function with complex parameters, for which one can write the exact recurrence formulas. It is assumed that the synchrotron radiation (SR) is preliminarily monochromatized and has a rather high degree of spatial coherence. These conditions are fulfilled, e.g., in the third-generation SR sources [5].



(left) Compound refractive x-ray lens and (right) parameters of its individual elements.

We choose the optical axis along the z axis (figure) and represent the general solution to the Maxwell equation as $E(x, y, z) = \exp(ikz)A_t(x, y, z)$, where $k = \omega/c$ is the wave number in vacuum. The function $A_t(x, y, z)$ describes the transfer, along the z axis, of the transverse dependence of the wave field. Since the radiation is hard and interacts weakly with a material, one can use, with a high accuracy, the paraxial approximation, i.e., ignore the second derivative of A_t with respect to the coordinate z , as compared to the first derivative. As a result, one arrives at the parabolic equation for the function $A_t(x, y, z)$

$$\frac{dA_t}{dz} = -ik\eta s(x, y, z)A_t + \frac{i}{2k} \left(\frac{d^2 A_t}{dx^2} + \frac{d^2 A_t}{dy^2} \right), \quad (1)$$

where $\eta = 1 - n = \delta - i\beta = \delta(1 - i\gamma)$. In the radiation-transfer problem, the wave field at the entrance surface of the lens is a given function $A_t(x, y, 0) = A_0(x, y)$, where the coordinate z is measured from the outset of the lens. In the compound lens, the function $s(x, y, z)$ is unity in the regions inside the material and zero outside it (figure).

In what follows, I consider only the case where the thickness p of an individual element of a compound lens is smaller than the characteristic scale of changing the transverse dependence of the wave field. In other words, the thin-lens approximation is assumed to be fulfilled for an individual element. This is always true for a compound lens with many elements. This restriction can be used for averaging the function $s(x, y, z)$ over its period and replacing it by a function depending only on the transverse coordinates:

$$\bar{s}(x, y) = \frac{d}{p} + \frac{x^2}{pR} + \frac{y^2}{pR}. \quad (2)$$

This dependence is valid only inside the lens geometrical aperture with diameter $a = 2[R(p - d)]^{1/2}$ (figure). However, the effective operation area (effective aperture) of the lens is determined by the x-ray absorption in its material and is almost always smaller than the geometrical aperture. Because of this, one can formally assume that dependence (2) holds everywhere over the region of transverse plane (X, Y) considered.

Let us represent the initial wave field as a Fourier integral

$$A_0(x, y) = \int \frac{dq_x dq_y}{(2\pi)^2} \exp(iq_x x + iq_y y) \tilde{A}_0(q_x, q_y) \quad (3)$$

and consider the solution $\tilde{P}_t(x, y, q_x, q_y, z)$ with the initial function in the form of plane wave $\tilde{P}_t(x, y, q_x, q_y, 0) = \exp(iq_x x + iq_y y)$. The solution can be represented as the

product $\tilde{P}_t = \exp(-ik\eta[d/p]z) \tilde{P}(x, q_x, z) \tilde{P}(y, q_y, z)$, with the partial function $\tilde{P}(x, q, z)$ satisfying the equation

$$\frac{d\tilde{P}}{dz} = -i \frac{k\eta}{pR} x^2 \tilde{P} + \frac{i}{2k} \frac{d^2 \tilde{P}}{dx^2}, \quad (4)$$

$$\tilde{P}(x, q, 0) = \exp(iqx).$$

This equation coincides formally with the Schrödinger equation for a particle in a parabolic potential. Nevertheless, the expansion in terms of the stationary states will not be considered in this work.

Taking into account the character of the initial function, it is reasonable to seek a solution in the form of a Gaussian function with complex coefficients

$$\begin{aligned} \tilde{P}(x, q, z) &= \exp(ia_0(z) + ia_1(z)x + ia_2(z)x^2), \\ a_0(0) &= a_2(0) = 0, \quad a_1(0) = q. \end{aligned} \quad (5)$$

Inserting Eq. (5) into Eq. (4) and equating the coefficients of the terms for the same x powers, one arrives at the system of ordinary differential equations

$$\begin{aligned} \frac{da_0}{dz} &= \frac{i}{k} a_2 - \frac{1}{2k} a_1^2, \\ \frac{da_1}{dz} &= -\frac{2}{k} a_1 a_2, \quad \frac{da_2}{dz} = -\frac{k\eta}{pR} - \frac{2}{k} a_2^2. \end{aligned} \quad (6)$$

This system has an analytic solution for any initial condition. It can be written as

$$\begin{aligned} a_2(z) &= a_2(0) \frac{\tan(\alpha - z/z_c)}{\tan(\alpha)}, \\ a_1(z) &= a_1(0) \frac{\cos(\alpha)}{\cos(\alpha - z/z_c)}, \\ a_0(z) &= a_0(0) - \frac{i}{2} \ln \left(\frac{\cos(\alpha)}{\cos(\alpha - z/z_c)} \right) \\ &\quad - \frac{a_1^2(0) z_c \tan(z/z_c)}{2k[1 + \tan \alpha \tan(z/z_c)]}, \\ \tan \alpha &= \frac{z_c}{z_0}, \quad z_0 = \frac{k}{2a_2(0)}, \quad z_c = \left(\frac{pR}{2\eta} \right)^{1/2}. \end{aligned} \quad (7)$$

The validity of this solution can be checked by direct substitution. Using initial conditions (5) and recurrence relations (7), one gets for the function $\tilde{P}(x, q, z)$

$$\tilde{P}(x, q, z) = \exp\left(-i \frac{kt_z}{2z_c} x^2\right) c_z^{-1/2} \exp\left(i \frac{x}{c_z} q - i \frac{z_c t_z}{2k} q^2\right). \quad (8)$$

Hereinafter, the notation $s_z = \sin(z/z_c)$, $c_z = \cos(z/z_c)$, and $t_z = \tan(z/z_c)$ is used.

Let us represent the general solution to the problem (for an arbitrary initial function) in the form of integral

$$A_t(x, y, z) = \int \frac{dq_x dq_y}{(2\pi)^2} \tilde{P}_t(x, y, q_x, q_y, z) \tilde{A}_0(q_x, q_y). \quad (9)$$

Substituting the expression for $\tilde{A}_0(q_x, q_y)$ in the form of the inverse Fourier transform and integrating with respect to q_x and q_y , one obtains the desired integral transformation for a compound x-ray lens with the parabolic profile

$$A_t(x, y, z) = \int dx' dy' P_t(x, y, x', y', z) A_t(x', y', 0), \quad (10)$$

whose propagator is factorized

$$P_t(x, y, x', y', z) = \exp(-ik\eta[d/p]z) P(x, x', z) P(y, y', z), \quad (11)$$

and the partial propagator is determined by the expression

$$P(x, x', z) = \exp\left(-i\frac{\pi t_z}{\lambda z_c} x^2\right) \times \frac{1}{(i\lambda z_c s_z)^{1/2}} \exp\left(i\pi \frac{(x - x' c_z)^2}{\lambda z_c s_z c_z}\right). \quad (12)$$

Here, $\lambda = 2\pi/k$ is the x-ray wavelength.

This expression is the main result of the work. One can readily verify that this function transforms to the Dirac delta function $\delta(x - x')$ at $z = 0$. Evidently, integral (10) must transform to the Kirchhoff integral in the limit $|\eta| \rightarrow 0$. Indeed, after passing to the limit $|z_c| \rightarrow \infty$ in Eq. (12), one obtains the following expression for the transverse part of the spherical wave in the paraxial approximation:

$$P(x, x', z) \xrightarrow{|\eta| \rightarrow 0} P_K(x - x', z) = \frac{1}{(i\lambda z)^{1/2}} \exp\left(i\pi \frac{(x - x')^2}{\lambda z}\right). \quad (13)$$

The expression for the propagator in a more complex problem of radiation transfer in air at a distance of r_o before the lens, through a lens of length L , and at a distance of r_i in air after the lens can be written as a convolution

$$G(x, x', r_o, L, r_i) = \int dx_2 dx_1 P_K(x - x_2, r_i) P(x_2, x_1, L) P_K(x_1 - x', r_o). \quad (14)$$

Note that the integrals in Eq. (14) are calculated analytically to give an analytic expression for the propagator G . However, the same result can be obtained by the method developed above, namely, by triply using recurrence relations (7), with the limiting transition $|\eta| \rightarrow 0$

being used for air. The method of recurrence relations (7) is particularly suitable in the development of algorithms for computer simulation of imaging formation using a lens. Although this computer program was developed by us, the analysis of particular results is beyond the scope of this brief communication. Moreover, this method can also be applied to a system of lenses with different parameters.

Below, main features following from Eq. (12) for the operation of a compound refractive lens are considered. Taking into account that $\gamma = \beta/\delta \ll 1$, the complex parameter z_c can be written as $z_c = (pF_1)^{1/2}(1 + i\gamma/2)$. At $L \ll (pF_1)^{1/2}$, one can retain only the leading terms in the sine and cosine expansions to obtain the following expression for the propagator in the thin-lens limit:

$$P_0(x, x', L) = \exp\left(-i\pi \frac{x^2}{\lambda F} [1 - i\gamma]\right) P_K(x - x', L), \quad (15)$$

$$F = \frac{F_1}{N} = \frac{R}{2N\delta}.$$

Note that the above-mentioned domain of applicability of this approximation can be written as $L \ll F$. Due to x-ray absorption, the plane wave, after passing through the lens, acquires the Gaussian shape, for which the intensity distribution halfwidth is $a_\gamma = 0.664(\lambda F/\gamma)^{1/2}$. This value can be considered as the lens effective aperture. The expression including the terms on the order of $(L/z_c)^3$ can easily be written to obtain the corrections on the order of L/F to the focal length in the thin-lens approximation.

For $L = L_0 = (pF_1)^{1/2}\pi/2$ and taking into account that $s_z = 1$ and $c_z = i\gamma\pi/4$, one obtains, in the linear approximation in γ , the following expression for the propagator:

$$P(x, x') = \frac{1}{(i\lambda z_c)^{1/2}} \times \exp\left[-i\frac{2\pi}{\lambda z_c} x x' - \gamma \frac{\pi^2}{4\lambda z_c} (x^2 + x'^2)\right]. \quad (16)$$

From this expression, it follows that, when passing through this lens, the wave is modulated by a Gaussian function because of the absorption in lens and then turns to its Fourier transform. In particular, at the lens output, a plane wave has a Gaussian intensity distribution with the halfwidth $s_\gamma = 0.47(\lambda L_0/\gamma)^{1/2}$, and the focal length is L_0 . The quantity s_γ gives the focal spot diameter, whereas the lens effective aperture in this case is $a_\gamma = 0.846(\lambda L_0/\gamma)^{1/2}$. If the absorption is ignored, the propagator will be equal to delta function $\delta(x + x')$ for $L = 2L_0$; i.e., the wave field is restored in the inverted form. Clearly, the lens will have the same properties for

$L = 3L_0, 4L_0$, and so on. However, the absorption diminishes the lens working region with increasing L .

In conclusion, let us estimate the parameters of the system. Consider a compound aluminum lens for photon energies of 25 keV. Let $p = 1$ mm and $R = 0.2$ mm [2]. One has in this case $\gamma = 2.02 \times 10^{-3}$, $F_1 = 116$ m, and $L_0 = 53.4$ cm. Therefore, the critical size of the compound lens is achieved when 534 elements are used. Evidently, L_0 is the minimal attainable focal length for a given radius of curvature of the parabolic surfaces. The focal spot diameter in this case is $s_\gamma = 0.11$ μm , and the effective aperture is $a_\gamma = 97$ μm . Smaller focal length can be obtained by a gradual decrease in the radius of curvature of the surfaces in individual elements.

REFERENCES

1. A. Snigirev, V. Kohn, I. Snigireva, and B. Lengeler, *Nature* **384**, 49 (1996).
2. B. Lengeler, C. G. Schroer, M. Richwin, *et al.*, *Appl. Phys. Lett.* **74**, 3924 (1999).
3. Y. Ohishi, A. Q. R. Baron, M. Ishii, *et al.*, *Nucl. Instrum. Methods Phys. Res. A* **467–468**, 962 (2001).
4. V. V. Protopopov and K. A. Valiev, *Opt. Commun.* **151**, 297 (1998).
5. V. Kohn, I. Snigireva, and A. Snigirev, *Phys. Rev. Lett.* **85**, 2745 (2000).

Translated by V. Sakun

Dilaton-Field Burning in Plasma

V. Ts. Gurovich* and V. N. Folomeev

Institute of Physics, National Academy of Sciences of Kyrgyzstan, Bishkek, 720071 Kyrgyzstan

* e-mail: *astra@freenet.kg*

Received July 24, 2002

We propose a mechanism for the effective transformation of dilaton-field energy in field stars into relativistic-plasma energy and radiation. The mechanism suggests initial transformation of the energy of an inhomogeneous dilaton field into electric-field energy followed by its dissipation into relativistic-plasma energy. The process is similar to the propagation of a relativistic detonation wave through a dilaton stellar atmosphere. © 2002 MAIK “Nauka/Interperiodica”.

PACS numbers: 97.10.Cv; 97.10.Ex; 04.40.Dg; 95.30.Gv; 95.30.Qd

(1) Boson stars formed by various types of scalar fields in their own gravitational field are extensively studied in modern theoretical astrophysics [1]. In the relativistic and nonrelativistic cases, the energy density of such fields can be very high, and the problem of transformation of this energy into radiation naturally arises. One such mechanism was proposed by Tkachev [2]. He considered a model for the generation of radiation by axion fields based on an analogy with the mechanism of laser radiation. Here, we propose an alternative mechanism which uses the dilaton-field energy.

Among the models of boson stars, the models of self-gravitating structures with dilaton fields are known [3]. The nature of these fields allows them to directly interact with electromagnetic fields. The corresponding system of equations admits solitonlike solutions for a longitudinal electrodilaton wave. It was shown that such a soliton could travel through an inhomogeneous dilaton stellar atmosphere formed by its own gravitational field. Passing from a region of high dilaton-field energy density to a region of lower energy density, such a soliton can appreciably increase the electric-field energy. According to the models of such field stars, the energy difference can be significant. The maximum electric-field strength can reach a critical value for the production of electron–positron pairs or can result in substantial Joule heating of the plasma that already exists in the dilaton field. It is important to note that in regions without electromagnetic fields, the dilaton field does not interact with quasi-neutral plasma. This model was demonstrated with simple analytic and semianalytic solutions. The realization of this mechanism in nature can give rise to impulsive energy release in the form of intense plasma heating and radiation in a regime similar to the detonation-wave mechanism. Processes of this kind are being intensively studied (see, e.g., [4] for a review). Note that the motion of this soliton is assumed to be relativistic, and the gravitational field of the boson star is assumed to be weak. Therefore,

the motion of an electrodilaton soliton with dissipation may be considered in terms of special relativity. We assume that an inhomogeneous dilaton-field energy distribution has already been produced by gravity and that only this distribution is important in the problem under consideration.

(2) The Lagrangian of a dilaton-electromagnetic field is given by [5]

$$L = 2\Phi_{;i}\Phi^{;i} - (F_{lm}F^{lm})e^{-2\alpha\Phi}, \quad (1)$$

where Φ is the dilaton-field potential, F_{lm} is the electromagnetic-field tensor, and α is the coupling constant. Equations for Φ and F_{ik} can be derived from (1):

$$[e^{-2\alpha\Phi}F^{ik}]_{;k} = 0, \quad (2)$$

$$\Phi_{;i}^{:i} = -\frac{\alpha}{2}e^{-2\alpha\Phi}(F_{lm}F^{lm}). \quad (3)$$

Let us consider a plane electrodilaton wave which propagates along the x axis and has only the longitudinal component $F^{10} = E_x = E$ by using these equations. Equation (2) yields

$$(e^{-2\alpha\Phi}E)_{;\tau} = 0; \quad (e^{-2\alpha\Phi}E)_{;x} = 0, \quad (4)$$

whence we can determine the constant of motion

$$e^{-2\alpha\Phi}E = E_0 = \text{const}. \quad (5)$$

The quadratic field combination

$$I = F_{lm}F^{lm} = -2E^2 \quad (6)$$

is negative in all special-relativity frames of reference.

The other field equation (3) takes the form

$$\frac{\partial^2\Phi}{\partial\tau^2} - \frac{\partial^2\Phi}{\partial x^2} = \alpha E_0^2 e^{2\alpha\Phi} \quad (7)$$

or, introducing the new variables $2\alpha E_0 x \rightarrow x$ and $2\alpha E_0 \tau \rightarrow \tau$ and the function $\psi = 2\alpha\Phi$, we obtain

$$\frac{\partial^2 \psi}{\partial \tau^2} - \frac{\partial^2 \psi}{\partial x^2} = e^\psi / 2. \quad (8)$$

This is one of the forms of the Liouville equation [6]. There is a general class of solutions for this equation that contains two arbitrary functions $f_1(x - \tau)$ and $f_2(x + \tau)$:

$$\psi = \ln \left[\frac{16 f_1'(x - \tau) f_2'(x + \tau)}{\cosh^2 [f_1(x - \tau) + f_2(x + \tau)]} \right]. \quad (9)$$

The primes denote the derivatives with respect to the arguments of the functions.

The solution for a steady-state soliton traveling with velocity u follows from the general solution with the arbitrary functions

$$f_1(x - \tau) = \gamma(x - \tau), \quad \gamma \equiv \frac{1 + u}{4\sqrt{1 - u^2}}, \quad (10)$$

$$f_2(x + \tau) = \beta(x + \tau), \quad \beta \equiv \frac{1 - u}{4\sqrt{1 - u^2}}. \quad (11)$$

It has the form

$$\begin{aligned} \psi &= -2 \ln \cosh \left(\frac{x - u\tau}{2\sqrt{1 - u^2}} \right), \\ E &= E_0 / \cosh^2 \left(\frac{x - u\tau}{2\sqrt{1 - u^2}} \right). \end{aligned} \quad (12)$$

To analyze the soliton evolution on an inhomogeneous dilaton background, we choose arbitrary functions in the form

$$f_1 = \gamma(x - \tau) + \ln \cosh \mu(\tau - x), \quad (13)$$

$$f_2 = \beta(x + \tau), \quad (14)$$

where γ and β are determined by the initial wave velocity from Eqs. (10) and (11) and μ is an arbitrary constant. The electric-field profile then takes the form

$$\begin{aligned} E/E_0 &= 16\beta[\gamma + \mu \tanh \mu(\tau - x)] / \cosh^2 Q, \\ Q &= [(\gamma + \beta)x - (\gamma - \beta)\tau + \ln \cosh \mu(\tau - x)]. \end{aligned} \quad (15)$$

The profile of this wave is shown in Fig. 1. The numerator in Eq. (15) slowly changes compared to the denominator. It thus follows that the electric soliton reaches its maximum at a given τ near zero of the cosh argument. Since the soliton velocity $u < 1$, the argument of the tangent is always positive in this range. The numerator in Eq. (15) and, hence, the electric field grows with time. This growth ceases as soon as $\tanh[\mu(\tau - x)]$ reaches its asymptotic value equal to 1 (see Fig. 1 for illustra-

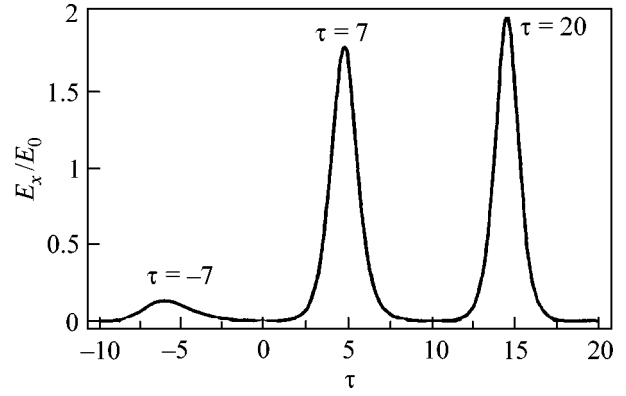


Fig. 1. The growth of the electric soliton in a wave with various asymptotic dilaton-field energy densities ahead of and behind the wave. Solution (15) with $u = 1/\sqrt{3}$ and $\mu = \gamma$ is shown at various times τ . The energy densities, in units of E_0^2 , are 7.4 and 0.2 ahead of and behind the soliton, respectively. At large τ , the solution transforms into a steady-state soliton.

tion). If an infinitely increasing function is substituted for $\tanh[\mu(\tau - x)]$ in Eq. (15), then the electric field will also continue to grow infinitely.

(3) A substantial accumulation of electric-field energy as the wave travels in plasma can result in fast heating of the latter. It is important to make sure that this heating is powered by the dilaton-field energy. To this end, let us consider the above wave traveling in plasma. As was pointed out above, the quasi-neutral plasma outside the region of E localization does not interact with the dilaton field. A current is generated in the electric-field region in plasma and the complete system of equations now takes the form

$$\begin{aligned} \frac{\partial \rho}{\partial t} + \frac{\partial j}{\partial x} &= 0, \quad \frac{\partial}{\partial x}(e^{-2\alpha\Phi} E) = 4\pi\rho, \\ \frac{\partial^2 \Phi}{\partial t^2} - \frac{\partial^2 \Phi}{\partial x^2} &= \alpha e^{-2\alpha\Phi} E^2, \end{aligned} \quad (16)$$

where ρ is the charge density and j is the conduction current. To further simplify the problem, we assume that the plasma conductivity σ is constant and that $j = \sigma E$. We seek a solution in the form of a steady-state wave that depends on the argument $\xi = x - ut$. Choosing E_c and ρ_0 as the characteristic electric-field strength and charge density, respectively, we introduce the following dimensionless quantities:

$$\begin{aligned} e &= E/E_c, \quad \Psi = 2\alpha\Phi, \quad \delta = \rho/\rho_0, \\ \eta &= \frac{2\alpha E_c}{\sqrt{1 - u^2}} \xi, \quad \zeta = \frac{2\pi\sigma\sqrt{1 - u^2}}{uE_c}. \end{aligned} \quad (17)$$

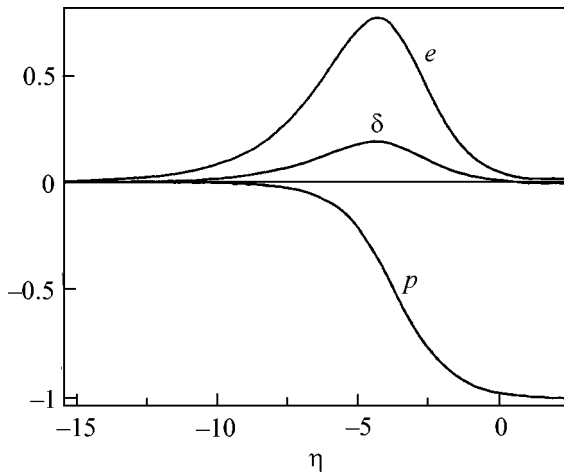


Fig. 2. An electro-dilaton soliton with dissipation. The dimensionless conductivity ζ and the constant C in Eq. (19) were chosen to ensure the total transformation of dilaton-field energy into plasma thermal energy behind the soliton ($p \rightarrow 0$).

The system of equations (16) then takes the form

$$\frac{d^2\Psi}{d\eta^2} = -\frac{1}{2}e^{-\Psi}e^2, \quad \frac{d}{d\eta}(\zeta e - \delta) = 0, \quad (18)$$

$$\frac{d}{d\eta}(e^{-\Psi}e) = \delta.$$

This system has the first integral

$$\frac{p}{2\zeta} + \frac{1}{4\zeta^2} \ln(1 - 2\zeta p) = \frac{1}{2}e^{-\Psi} + C, \quad (19)$$

where $p = d\Psi/d\eta$ and C is the integration constant. Its analysis allows the transformation of dilaton-field energy into plasma thermal energy to be traced. As in the nondissipative case (see (12)), $\Psi \rightarrow -\infty$ ahead of and behind this soliton and the corresponding asymptotic values of p follow from Eq. (19) for $e^{-\Psi} \rightarrow 0$. In these regions, the dilaton-field energy density is determined only by the derivatives of the dilaton potential; i.e., it is proportional to p^2 .

When dissipation is switched off ($\zeta \rightarrow 0$), it follows from Eq. (19) that the asymptotic values of p are equal in magnitude. This equality implies that the asymptotic values of the dilaton-field energy density ahead of and behind the soliton are equal. Otherwise, the transformation of dilaton-field energy into electric energy and back into dilaton energy would be reversible. In the presence of dissipation ($\zeta \neq 0$), the asymptotic value of p ahead of the soliton is larger than its value behind the soliton, implying energy losses through dissipation. Figure 2 shows our numerical

solution to the system of equations (18), which confirms the above analysis. The conductivity ζ was chosen in such a way that all of the dilaton-field energy transformed into thermal energy. Note that the wave carries a finite charge. If this solution is assumed to evolve from a quasi-neutral system, then the corresponding negative charge should be assumed to remain outside the soliton-like solution.

(4) A more complex dissipation mechanism, in particular, the production of electron-positron pairs in an intense field E , can be considered in terms of this model. However, it was first necessary to demonstrate the very fact of the transformation of dilaton-field energy into plasma thermal energy using a simple example.

The realization of this mechanism greatly depends on the experimental confirmation of the direct interaction between the dilaton and electromagnetic fields in Lagrangian (1). We are grateful to the referee who pointed to the paper by Chiba and Kohri [7], in which this problem was addressed. However, note the following. If the dilaton charge $h^2e^{2b\Phi}$ is substituted in Lagrangian (1) for the electromagnetic field, then all of the above conclusions regarding the increase in the energy of the soliton as it moves in an inhomogeneous field remain valid. This concentrated dilaton-field energy can be transferred through a different channel when the dilaton interaction with other fields is included. Radiation can be generated, for example, by the mechanism from [2].

We thank H. Kleinert and H.J. Schmidt with whom we formulated the original problem [8]. We are grateful to A. Starobinsky and V. Usov for the discussion of the model. This study was supported by the ISTC Project no. KR-677.

REFERENCES

1. E. Mielke and F. Schunck, gr-qc/9801063; Gen. Relativ. Gravit. **33**, 805 (2001).
2. I. Tkachev, Sov. Astron. Lett. **12**, 305 (1986); I. Tkachev, Phys. Lett. B **191**, 41 (1987).
3. Zhi-jian Tao and Xan Xue, Phys. Rev. D **45**, 1878 (1992); P. Fiziev, S. Yazadjiev, *et al.*, gr-qc/0001103.
4. V. Berezhinsky, astro-ph/0107306.
5. R. Gregory and J. Harvey, Phys. Rev. D **47**, 2411 (1993); T. Matos, D. Nunez, and H. Quevedo, Phys. Rev. D **51**, R310 (1995).
6. J. Liouville, J. Math. Pures Appl. **18**, 71 (1853).
7. T. Chiba and K. Kohri, Prog. Theor. Phys. **107**, 631 (2002); T. Chiba, gr-qc/0110118.
8. H. Kleinert, H. J. Schmidt, *et al.*, gr-qc/0206043.

Translated by V. Astakhov

Dynamics of a Longitudinal-and-Transverse Acoustic Wave in a Crystal with Paramagnetic Impurities

A. A. Zabolotskii

Institute of Automation and Electrometry, Siberian Division, Russian Academy of Sciences, Novosibirsk, 630090 Russia

e-mail: zabolotskii@iae.nsk.su

Received October 1, 2002

The evolution of longitudinal-and-transverse acoustic pulses propagating along an external magnetic field through a system of resonant paramagnetic impurities with effective spin $S = 1/2$ is studied theoretically. It is shown that, when the group velocities of longitudinal and transverse waves are equal and the impurity concentration is sufficiently small, the initial system of equations is reduced to new evolution equations, which are integrable within the framework of the inverse scattering problem approach. These equations qualitatively describe the new coherent dynamics of acoustic pulses. © 2002 MAIK “Nauka/Interperiodica”.

PACS numbers: 62.65.+k; 72.55.+s; 43.35.Rw

Nonlinear coherent optical phenomena associated with soliton and other self-similar solutions [1] were thoroughly studied analytically within the framework of integrable models [2]. When elastic waves propagate through a paramagnetic crystal, solitonlike pulses can form as a result of the effects associated with anharmonic oscillations and dispersion [3], as well as due to the effect of nonlinear coherent interaction of acoustic waves with paramagnetic impurities in the medium, in the conditions of a self-induced acoustic transparency [4, 5].

The evolution of an acoustic pulse in a crystal with paramagnetic impurities has a number of distinctive features making it qualitatively different from the light-wave dynamics in the medium. For example, such features are associated with the fact that the sound wave in a crystal may be of a longitudinal-and-transverse type. The self-induced acoustic transparency was observed at low temperatures in crystal samples with paramagnetic impurities [6]. In other experiments [7, 8], this effect was observed in Fe^{2+} impurities in MgO and LiNbO_3 crystal matrices.

The theory of self-induced acoustic transparency for a transverse pulse propagating in the direction parallel to magnetic field in a spin system with $S = 1/2$ was developed, e.g., in [4, 5]. In this theory, the equations describing the acoustic-pulse dynamics under a number of simplifying assumptions were reduced to both non-integrable and well-known simple integrable models.

The main purpose of this paper is the study of the new acoustic-pulse dynamics with allowance for significant changes in the transverse and longitudinal field components. For this purpose, a new general integrable model that describes the one-dimensional dynamics of

pulses propagating in a crystal with paramagnetic impurities with spin $S = 1/2$ is proposed.

Let us derive the equations describing the dynamics of a longitudinal-and-transverse wave in a crystal with paramagnetic impurities (cf. [5]). We assume that a homogeneous static external magnetic field \mathbf{B} is directed along the z axis. The contribution of the Zeeman interaction of the magnetic moment $\hat{\mu}^{(a)}$ located at point a to the general Hamiltonian is $\hat{H}_a = -\hat{\mu}^{(a)} \mathbf{B}$. The components $\hat{\mu}^{(a)}$ are expressed through the spin components $\mathbf{S}^{(a)}(\mathbf{r}_a)$, where \mathbf{r}_a is the radius vector of the a th spin:

$$\hat{\mu}_j^{(a)} = -\sum_k \mu_B g_{jk} \hat{S}_k^{(a)}.$$

Here, μ_B is the Bohr magneton and g_{jk} are the components of the Landé tensor.

Assume that the x , y , and z coordinate axes directed along the principal axes of the Landé tensor coincide with the crystal symmetry axes. Then, in the unstrained unperturbed medium, the Landé tensor is diagonal: $g_{jk} = g_{jk}^{(0)} = g_{jj} \delta_{jk}$, where δ_{jk} is the delta function. To describe the crystal strain caused by the acoustic wave, we introduce linear corrections to the Landé tensor:

$$g_{jk} = g_{jk}^{(0)} + \sum_{p,q} \left(\frac{\partial g_{jk}}{\partial \mathcal{E}_{pq}} \right)_0 \mathcal{E}_{pq} + \dots, \quad (1)$$

where \mathcal{E} is the elastic strain tensor of the crystal at the point where the spin is located. The derivatives are taken at the point where the strain is zero. The strain

tensor components are expressed through the components of the displacement vector $\mathbf{U} = (U_x, U_y, U_z)$:

$$\mathcal{E}_{pq} = \frac{1}{2} \left(\frac{\partial U_p}{\partial x_q} + \frac{\partial U_q}{\partial x_p} \right).$$

The spin–phonon interaction is described by the Hamiltonian involving the first-order terms of the expansion in \mathcal{E}_{pq} powers. We consider the evolution of the field along the z axis parallel to the vector \mathbf{B} . In this case, the symmetry transformations include the mirror reflections about the planes $x = 0$, $y = 0$, and $z = 0$. With allowance for these conditions, the expressions for \hat{H}_s and \hat{H}_{int} take the form

$$\hat{H}_s = \int n \hbar \omega_B S_z d^3 \mathbf{r}, \quad (2)$$

$$\langle \hat{H}_{\text{int}} \rangle = \int \sum_{\gamma} \frac{n \hbar \omega_B}{g} f_{\gamma} \mathcal{E}_{\gamma z} S_{\gamma} d^3 \mathbf{r}. \quad (3)$$

Hereafter, γ sequentially represents x , y , and z ; $S_{\gamma} = \text{Tr} \{ \hat{s}_{\gamma}, \hat{\rho} \}$, where $\hat{\rho}$ is the density matrix and \hat{s}_{γ} are the Pauli matrices; $\omega_B = g \mu_B B / \hbar$ is the frequency of Zeeman splitting of the Kramers doublet, where $g = g_{xx} = g_{yy} = g_{zz}$; $n(\mathbf{r}) = \sum_j \delta(\mathbf{r} - \mathbf{r}_j)$ is the concentration of paramagnetic impurities; the integrals are taken over the crystal volume; and $f_{\gamma} = \partial g_{zz} / \partial \mathcal{E}_{\gamma z}$ are the spin–phonon coupling constants [8].

Without regard for anharmonicity, under the aforementioned symmetry conditions the acoustic-field dynamics in the crystal can be described by the Hamiltonian

$$\hat{H}_a = \frac{1}{2} \int \left\{ \frac{p_x^2 + p_y^2 + p_z^2}{n_0} + \sum_{\gamma} \lambda_{\gamma} \left(\frac{\partial U_{\gamma}}{\partial z} \right)^2 \right\} d^3 \mathbf{r}, \quad (4)$$

where n_0 is the average density of the crystal, p_j ($j = x, y, z$) are the momentum density components caused by the dynamic displacements, and λ_{γ} are the elements of the elastic constant tensor of the crystal [9]. The number of phonons is assumed to be large, so that the classical description of the acoustic field dynamics is valid.

The equations describing the evolution of the effective spin and the acoustic field have the form

$$i \hbar \frac{\partial \hat{\rho}}{\partial t} = [\hat{H}, \hat{\rho}], \quad (5)$$

$$\frac{\partial \mathbf{U}}{\partial t} = \frac{\partial H}{\partial \mathbf{p}}, \quad \frac{\partial \mathbf{p}}{\partial t} = - \frac{\partial H}{\partial \mathbf{U}}. \quad (6)$$

Here, $H = H_a + \langle \hat{H}_{\text{int}} \rangle$. The interaction between the spin and the field of an elastic pulse is described by the classical Hamilton equations for a continuous medium.

Using Eqs. (2)–(6), we obtain a system of evolution equations for $\mathcal{E}_{\gamma z}$:

$$\frac{\partial^2 \mathcal{E}_{\gamma z}}{\partial t^2} - v_{\gamma}^2 \frac{\partial^2 \mathcal{E}_{\gamma z}}{\partial z^2} = \frac{n G_{\gamma} \partial^2 S_{\gamma}}{n_0 \partial z^2}. \quad (7)$$

Here, $G_{\gamma} = \hbar \omega_B f_{\gamma} / g$, $v_{\gamma} = \sqrt{\lambda_{\gamma} / n_0}$,

$$\frac{\partial S_x}{\partial t} = - \left(\omega_B + \frac{G_z \mathcal{E}_{zz}}{\hbar} \right) S_y + \frac{G_y \mathcal{E}_{yz}}{\hbar} S_z, \quad (8)$$

$$\frac{\partial S_y}{\partial t} = \left(\omega_B + \frac{G_z \mathcal{E}_{zz}}{\hbar} \right) S_x - \frac{G_x \mathcal{E}_{xz}}{\hbar} S_z, \quad (9)$$

$$\frac{\partial S_z}{\partial t} = \frac{1}{\hbar} (G_x \mathcal{E}_{xz} S_y - G_y \mathcal{E}_{yz} S_x). \quad (10)$$

Let us obtain the most general integrable reduction of the basic system of equations (7)–(10) without considering losses. Assume that the phase velocities of waves are equal: $v_x = v_y = v_z = v$. This situation takes place in elastically isotropic crystals, such as alkali metal halides with central interaction forces between the atoms [10].

The reduction must describe the dynamics of acoustic pulses with durations on the order of $\pi \omega_B^{-1}$ or smaller. With this condition, the slow envelope approximation does not apply.

In real media, the concentration of paramagnetic impurities can often be considered as small. Then, it is possible to apply the unidirectional propagation approximation similar to that used in [11] for deriving the reduced Maxwell–Bloch equations for a two-level optical medium. In this case, we can write the following formal approximate equality: $\partial_z \approx -v^{-1} \partial_t + \mathcal{O}(\epsilon)$, where ϵ is a perturbation. The normalized impurity concentration is of the same order of smallness as the derivative $\partial_{\tilde{z}} = \partial_z + v^{-1} \partial_t$ of the acoustic field amplitudes. The derivative with respect to z on the right-hand sides of Eqs. (7) can be replaced by $v^{-1} \partial_t$ with an accuracy of $\mathcal{O}(\epsilon^2)$.

If the propagation of acoustic pulses is unidirectional, system (7) is reduced to the form

$$\frac{\partial \mathcal{E}_{\gamma}}{\partial \tilde{z}} = \frac{n G_{\gamma}}{2 v^2 n_0} \frac{\partial S_{\gamma}}{\partial t}. \quad (11)$$

From Eqs. (8)–(11), we derive the relation

$$\mathcal{E}_{xz}^2 + \mathcal{E}_{yz}^2 + \left(\mathcal{E}_{zz} + \frac{\omega_B \hbar}{G_z} \right)^2 = I_0^2(t). \quad (12)$$

Here, the real function $I_0(t)$ is determined by the boundary conditions. With allowance for Eq. (12), new

integrable system of equations (8)–(11) can be represented as

$$\frac{\partial}{\partial \vartheta} \mathbf{S} = [\mathbf{F}, \mathbf{S}], \quad \frac{\partial}{\partial \chi} \mathbf{F} = \frac{\partial}{\partial \vartheta} \hat{\mathbf{J}} \mathbf{S}. \quad (13)$$

Here, $F_x = G_x \mathcal{E}_{xz} I_0^{-1}$, $F_y = G_y \mathcal{E}_{yz} I_0^{-1}$, and $F_z = (G_z \mathcal{E}_{zz} + \hbar \omega_B) I_0^{-1}$ are the components of the vector \mathbf{F} ; S_γ are the components of the vector \mathbf{S} ; $\hat{\mathbf{J}} = \text{diag}(1, a, b)$, where $a = f_y^2/f_x^2$ and $b = f_z^2/f_x^2$; $\vartheta = \int_0^t I_0(t') dt'$; and $\vartheta = \tilde{\chi} n G_x^2 (2\hbar n_0 v^2)^{-1}$.

System (13) can be represented as the condition that the following linear systems of equations are compatible:

$$\partial_\vartheta \Phi = \begin{pmatrix} -i\lambda F_z & \gamma_0 F_x + \gamma_1 F_y \\ \tilde{\gamma}_0 F_x + \tilde{\gamma}_1 F_y & i\lambda F_z \end{pmatrix} \Phi, \quad (14)$$

$$\partial_\chi \Phi = \begin{pmatrix} i\eta \lambda S_z & \beta_0 S_x + \beta_1 S_y \\ \tilde{\beta}_0 S_x + \tilde{\beta}_1 S_y & -i\eta \lambda S_z \end{pmatrix} \Phi. \quad (15)$$

Here,

$$\gamma_0 = \frac{1}{4} \left[\sqrt{\frac{b}{a}} \mu - 2 \sqrt{\frac{a}{b}} (b-1) + \sqrt{\frac{b}{a}} (a-1) \right],$$

$$\tilde{\gamma}_0 = -\frac{1}{4} \left[\sqrt{\frac{b}{a}} \mu - \sqrt{\frac{b}{a}} (a-1) \right],$$

$$\tilde{\gamma}_1 = i \frac{\sqrt{b} [(a-1)^2 - \mu^2]}{16\sqrt{a} a \lambda},$$

$$\gamma_1 = i \frac{(a + \mu - 1) \left[2(b-1) \sqrt{\frac{a}{b}} - \sqrt{\frac{b}{a}} (a + \mu - 1) \right]}{16a\lambda},$$

$$\beta_0 = \frac{2a(b-1) \sqrt{\frac{a}{b}} + a \sqrt{\frac{b}{a}} (a + \mu - 1)}{2(1 + a - \mu)},$$

$$\tilde{\beta}_1 = i \frac{\sqrt{\frac{b}{a}} [(a-1)^2 - \mu^2]}{8\lambda(1 + a - \mu)}, \quad \tilde{\beta}_0 = \frac{\sqrt{ab}(a - \mu - 1)}{2(1 + a - \mu)},$$

$$\beta_1 = -i \frac{(a + \mu - 1) \left[2(b-1) \sqrt{\frac{a}{b}} + \sqrt{\frac{b}{a}} (a + \mu - 1) \right]}{8\lambda(1 + a - \mu)},$$

and $\eta = (1 + a + \mu)[2(4\lambda^2 - 1)]^{-1}$, $\mu = \sqrt{16a\lambda^2 + (1-a)^2}$.

As reductions, system (13) has new integrable systems of equations corresponding to $a \neq 1$, $b = 1$ and to $a = 1$, $b \neq 1$. For $a = 1$ and $b = 1$, system (13) formally coincides with the model of a symmetric chiral field on the O_3 group [2]. It should be emphasized that system (13) cannot be reduced to an integrable model of an asymmetric chiral field [12]. Since system (13) is difficult to analyze, we proceed with considering its simple though nontrivial reduction.

Let the z axis be a fourfold symmetry axis; i.e., consider the case $a = 1$, $b \neq 0$. For $a = 1$, system (13) has the following Lax representation:

$$\partial_\tau \Phi = \begin{pmatrix} -i\lambda F_3 (\lambda + \beta) E \\ -\lambda E^* & i\lambda F_3 \end{pmatrix} \Phi \equiv \hat{L} \Phi, \quad (16)$$

$$\begin{aligned} & \partial_\chi \Phi \\ & = \frac{1}{(2\lambda - 1)} \begin{pmatrix} -i\lambda S_z & -\sqrt{b}(\lambda + \beta) S \\ \sqrt{b}\lambda S^* & i\lambda S_z \end{pmatrix} \Phi \equiv \hat{A} \Phi. \end{aligned} \quad (17)$$

Here, λ is the spectral parameter, $\tau = \vartheta \sqrt{b}$, $E = F_x - iF_y$, $F_z = \sqrt{b} F_3$, $S = S_x - iS_y$, and $\beta = (1 - b)/2\sqrt{b}$.

We solve the problem on the entire axis for $E(\tau) \rightarrow 0$ and $\tau \rightarrow \pm\infty$ under the assumption that, at the initial and final instants, the spin system is in the stable ground state: $S_z(\tau, \chi) = -1$, $S(\tau, \chi) = 0$, and $\tau \rightarrow \pm\infty$. We assume that the acoustic pulse $E(\tau, 0)$ introduced in the crystal has an area sufficiently large for the soliton formation.

Spectral problem (16) differs in its symmetry properties from previously investigated similar problems associated with solving the integrable Heisenberg and Landau–Lifshits equations [13] or the Raman scattering and four-wave mixing equations [14]. Therefore, it is necessary to develop an apparatus for the inverse problem method, as applied to this model with allowance for its specificity.

The solutions to spectral problem (16) possess the following involution:

$$\Phi = \hat{M} \Phi(\lambda^*)^* \hat{M}^{-1}, \quad \hat{M} = \begin{pmatrix} 0 & (\lambda + \beta)/\lambda \\ -1 & 0 \end{pmatrix}. \quad (18)$$

In view of Eqs. (18), the Jost functions Ψ^\pm , being the solutions to problem (16) with the asymptotic behavior

$$\Psi^\pm = \exp(-i\lambda \sigma_3 \tau), \quad \tau \rightarrow \pm\infty, \quad (19)$$

can be represented in the form

$$\Psi^\pm = \begin{pmatrix} \psi_1^\pm - \psi_2^{\pm*} \frac{\lambda + \beta}{\lambda} \\ \psi_2^\pm & \psi_1^{\pm*} \end{pmatrix}.$$

These solutions are related to the scattering matrix \hat{T} :

$$\Psi^- = \Psi^+ \hat{T}, \quad \hat{T} = \begin{pmatrix} a^* & b(\lambda + \beta)/\lambda \\ -b^* & a \end{pmatrix}. \quad (20)$$

The Jost functions have standard analytic properties (see, e.g., [15]); $a(\lambda)$ is holomorphic in the upper half-plane of λ , where its zero values correspond to soliton solutions.

Represent the Jost functions in the form

$$\Psi^+(\tau) = e^{-i\lambda\sigma_3\tau} + \int_{\tau}^{\infty} \begin{pmatrix} \lambda K_1(\tau, s) & (\lambda + \beta)K_2(\tau, s) \\ -\lambda K_2^*(\tau, s) & \lambda K_1^*(\tau, s) \end{pmatrix} e^{-i\lambda\sigma_3 s} ds. \quad (21)$$

Substituting the components of these functions from Eq. (21) into Eqs. (18) and integrating the resulting equations with respect to λ from $-\infty$ to ∞ with the weighting function $e^{-i\lambda y}(2\pi\lambda)^{-1}$, we obtain the Marchenko equations for the right end of the axis ($y \geq \tau$):

$$K_2^*(\tau, y) = F_0(\tau + y) + i \int_{\tau}^{\infty} K_1(\tau, s) \partial_y F_0(s + y) ds, \quad (22)$$

$$K_1^*(\tau, y) = - \int_{\tau}^{\infty} K_2(\tau, s) (\beta + i\partial_y) F_0(s + y) ds. \quad (23)$$

Here,

$$F_0(y) = \int_{\mathcal{C}} \frac{b}{a}(\chi) \frac{1}{2\pi\lambda} e^{-i\lambda y} d\lambda, \quad (24)$$

where \mathcal{C} is a contour including the real axis and passing above all poles in the upper complex half-plane.

From Eqs. (21) and (16), we obtain the relation

$$K_2(\tau, \tau)[1 + F_3(\tau)] = E^*(\tau)[1 - iK_1(\tau, \tau)]. \quad (25)$$

Using Eq. (25) and the condition $F_3 + EE^* = 1$, we obtain the relation between the potential E and the kernels $K_{1,2}$:

$$E(\tau) = \frac{2[1 - iK_1(\tau, \tau)]K_2^*(\tau, \tau)}{[1 + iK_1^*(\tau, \tau)][1 - iK_1(\tau, \tau)] + |K_2(\tau, \tau)|^2}. \quad (26)$$

Let us find a single-soliton solution associated with a single eigenvalue λ . Represent the kernel F corresponding to the eigenvalue λ in the form

$$F_0(y) = C_0(\chi) \exp(-i\lambda y), \quad (27)$$

where $C_0 = -ib(\chi; \lambda)/(\lambda \partial_{\eta} a(\chi; \eta)|_{\eta=\lambda})$.

The dependence of the scattering data on χ is determined by the formula [15]

$$\partial_{\chi} \hat{T} = -\hat{T} e^{-i\sigma_3 \lambda \tau} \hat{A}(\tau = -\infty, \chi) e^{i\sigma_3 \lambda \tau} + e^{-i\sigma_3 \lambda \tau} \hat{A}(\tau = \infty, \chi) e^{i\sigma_3 \lambda \tau} \hat{T}. \quad (28)$$

For the chosen initial and boundary conditions corresponding to the soliton dynamics, Eq. (28) yields

$$\frac{b(\lambda)}{\partial_{\eta} a(\eta)|_{\eta=\lambda}}(\chi) = -S_0 \exp\left(\frac{-2i\chi\lambda}{2\lambda - 1}\right), \quad (29)$$

where S_0 is a constant. For simplicity, we set $\xi = 0$. Using Eqs. (26)–(29), we obtain a single-soliton solution for the model under consideration with $\lambda = i\eta$:

$$E(\tau, \chi) = \frac{2S_0\eta^{-1}\mu(\tau, \chi)[1 - \gamma_1|\mu(\tau, \chi)|^2]e^{i\phi_s}}{1 + |\mu(\tau, \chi)|^2[|S_0|^2\eta^{-2} - \gamma_1 - \gamma_1^*] + |\mu(\tau, \chi)|^4|\gamma_1|^2}, \quad (30)$$

where

$$\mu(\tau, \chi) = \exp\left(2\tau\eta - \frac{4\eta\chi}{1 + 4\eta^2} + \frac{4i\eta^2\chi}{1 + 4\eta^2}\right),$$

$$\phi_s = \arg\left[\frac{1 + \gamma_1^*|\mu(\tau, \chi)|^2}{1 + \gamma_1|\mu(\tau, \chi)|^2}\right], \quad \gamma_1 = \frac{|S_0|^2(\eta^2 + i\eta\beta)}{4\eta^4},$$

and the y and x components of the transverse field have different signs at any instant of time. The soliton solution describes intense energy transfer between all components of the acoustic field with allowance made for relation (12). From solution (30), it also follows that the asymmetry associated with the deviation of b from unity gives rise to a nonlinear addition to the soliton phase ϕ_s . This addition describes a nonlinear rotation of the polarization of a transverse field.

In the general case, apart from the soliton solutions, it is necessary to take into account solutions of other types, such as radiation solutions associated with the continuous spectrum of problem (16). For example, for a small initial acoustic pulse $|E| \ll 1$ and $S_z(0, \chi) = 1$, soliton solutions do not exist, and the field dynamics are associated with the continuous spectrum of problem (16) alone. Consider some estimates for the medium parameters and the power of soliton acoustic pulses that can be generated in a medium of this kind. As an example, we consider a MgO crystal with Fe^{2+} paramagnetic impurities at the temperature $T = 4$ K. Let the magnetic field be such that $\omega_B = 10^{12} \text{ s}^{-1}$. In this case, the condition $\tau_p \sim \omega^{-1}$ is valid for pulse durations of ~ 100 ps. The condition $\omega_B = 10^{12} \text{ s}^{-1}$ corresponds to magnetic field strengths attainable in laboratory conditions. For the parameters of the medium, we have [6] $G_{\gamma} \sim 10^{-13} \text{ Erg}$, $n \sim 10^{19} \text{ cm}^{-3}$, $n_0 \sim 3\text{--}4 \text{ g/cm}^3$, $v \approx 5\text{--}10 \times 10^5 \text{ cm/s}$, and

$\lambda_\gamma \approx 5-10 \times 10^{11}$ dyn/cm². In these conditions, the intensity of the soliton signal may reach $I \sim 10^6$ W/cm².

System (13) describes the complex dynamics of three field components and can be used to describe new physical phenomena, including a strong interaction of several fields. For example, consider the phenomenon of electromagnetically induced transparency (EIT) [16], which was observed in multilevel optical systems. In the presence of a strongly varying linear dispersion, the EIT leads to a considerable decrease in the group velocity of light in the medium down to values that may be comparable with or smaller than the velocity of sound in this medium. Such a decrease in the group velocities of light was observed experimentally in crystals with implanted rare-earth ions and in other media. A decrease in the resonance absorption, along with the strong linear dispersion, suggests new mechanisms of the resonance interaction of light with acoustic waves. In [17], it was stated that, owing to the strong linear dispersion associated with the EIT, the phase matching between electromagnetic and acoustic waves is possible in a dielectric optical waveguide with implanted three-level ions. In [18], the interaction of an electromagnetic field with acoustic phonons was described using a Hamiltonian similar to that used above for describing the coupling between the spin states and acoustic phonons. A resonant optical medium can be modeled by an effective two-level medium. The ponderomotive force related to the local density variations in the optical medium makes a contribution to the acoustic-field dynamics, and the expression for this contribution corresponds to the right-hand sides of Eqs. (7). In such a scheme, it is necessary to take into account not only the transverse electromagnetic field, but also the longitudinal acoustic field, whose contribution to the dynamics of optical medium manifests itself as a nonlinear phase modulation. With a model analogous to model (13), it is possible to study the Brillouin scattering processes for picosecond acoustic pulses.

In closing, it should be noted that the new integrable model (13) can also be used in the theory of gravitation.

REFERENCES

1. A. I. Maimistov and A. M. Basharov, *Nonlinear Optical Waves* (Kluwer Academic, Dordrecht, 1999).
2. V. E. Zakharov, S. V. Manakov, S. P. Novikov, and L. P. Pitaevskii, *Theory of Solitons: the Inverse Scattering Method* (Nauka, Moscow, 1980; Consultants Bureau, New York, 1984).
3. H.-Y. Hao and H. J. Maris, *Phys. Rev. B* **64**, 064302 (2001).
4. G. A. Denisenko, *Zh. Éksp. Teor. Fiz.* **60**, 2269 (1971) [*Sov. Phys. JETP* **33**, 1220 (1971)].
5. S. V. Voronkov and S. V. Sazonov, *Zh. Éksp. Teor. Fiz.* **120**, 269 (2001) [*JETP* **93**, 236 (2001)].
6. V. A. Golenishchev-Kutuzov, V. V. Samartsev, N. K. Solovarov, and B. M. Khabibulin, *Magnetic Quantum Acoustics* (Nauka, Moscow, 1997).
7. N. S. Shiren, *Phys. Rev. B* **2**, 2471 (1970).
8. V. V. Samartsev, B. P. Smol'akov, and R. Z. Sharipov, *Pis'ma Zh. Éksp. Teor. Fiz.* **20**, 644 (1974) [*JETP Lett.* **20**, 296 (1974)].
9. L. D. Landau and E. M. Lifshits, *Course of Theoretical Physics, Vol. 7: Theory of Elasticity*, 4th ed. (Nauka, Moscow, 1987; Pergamon, New York, 1986).
10. C. Kittel, *Introduction to Solid State Physics*, 5th ed. (Wiley, New York, 1976; Nauka, Moscow, 1978).
11. J. D. Gibbon, P. J. Coudrey, J. K. Eilbeck, and R. K. Bullough, *J. Phys. A: Math. Gen.* **6**, 1237 (1973).
12. I. V. Cherednik, *Teor. Mat. Fiz.* **47**, 755 (1981).
13. A. E. Borovik and S. I. Kulinich, *Pis'ma Zh. Éksp. Teor. Fiz.* **39**, 320 (1984) [*JETP Lett.* **39**, 384 (1984)].
14. A. A. Zabolotskii, *Physica D (Amsterdam)* **40**, 283 (1989).
15. L. A. Takhtadzhyan and L. A. Faddev, *Hamiltonian Methods in the Theory of Solitons* (Nauka, Moscow, 1986; Springer, Berlin, 1987).
16. S. E. Harris, J. E. Field, and A. Imamoglu, *Phys. Rev. Lett.* **64**, 1107 (1990).
17. A. B. Matsko, Yu. V. Rostovtsev, H. Z. Cummins, and M. O. Scully, *Phys. Rev. Lett.* **84**, 5752 (2000).
18. A. B. Matsko, V. V. Rostovtsev, M. Flieschhauer, and M. O. Scully, *Phys. Rev. Lett.* **86**, 2006 (2001); V. Kovalev, *Phys. Rev. Lett.* **88**, 239301 (2002).

Translated by E. Golyamina

Universality and Scaling of Unstable Plastic Flow

M. A. Lebyodkin, L. R. Dunin-Barkovskii, and T. A. Lebedkina

Institute of Solid State Physics, Russian Academy of Sciences, Chernogolovka, Moscow region, 142432 Russia

e-mail: lebedkin@issp.ac.ru; dbarkov@issp.ac.ru; tlebyod@issp.ac.ru

Received October 4, 2002

The statistics of the jumplike plastic deformation of a Cu–Be alloy under the conditions of a low-temperature unstable plastic flow is studied experimentally. At a high strain rate, the parameters of the load jumps are found to be related by power laws, which corresponds to a scale-invariant behavior. A comparison with the data obtained for another mechanism of plastic instability, namely, the Portevin–Le Chatelier effect, points to the existence of universal laws governing the dynamics of a dislocation ensemble in the conditions of plastic instability. © 2002 MAIK “Nauka/Interperiodica”.

PACS numbers: 62.20.Fe; 46.35.+z; 81.05.Bx; 05.65.+b

The plastic flow of a solid is an example of a nonlinear dynamical phenomenon that occurs in an extended dissipative system represented by an ensemble of defects in a crystal structure. The dynamics of such systems obeys unified laws and, in particular, exhibit self-organization at different scale levels in space and/or time [1]. Therefore, studies of the plastic flow from the viewpoint of the self-organization of the dislocation motion, i.e., the motion of the main plasticity carriers, have attracted considerable interest in the last few years [2, 3]. In some cases, collective processes in a dislocation ensemble manifest themselves at the macroscopic level in the form of jumplike deformation curves reflecting the complex evolution of the flow stress [3, 4]. The corresponding self-organization in time is accompanied by a spatial self-organization, namely, by the localization of the plastic flow in the deformation bands, which may be stationary or may propagate along the crystal in the form of solitary waves [3]. Such a complex space–time behavior suggests that the jumplike deformation curves be analyzed in terms of the theory of dynamical systems.

Recent studies (see, e.g., [5–9]) of the deformation curves by the methods of statistical, dynamical, and multifractal analyses have revealed complex correlations between the plastic processes that occur in the course of the jumplike plastic deformation of alloys as a result of the dynamic interaction of dislocations with impurity atoms, i.e., in the conditions of the Portevin–Le Chatelier effect [3]. It was found that, at low strain rates, the character of flow corresponds to a dynamic chaos [10], while, at higher strain rates, a transition to self-organized criticality takes place [11]. At the same time, the plastic instability can be of a different microscopic origin, which makes it possible to study both universal and unique dynamic manifestations of physically different mechanisms. In this paper, we study the statistics of the low-temperature instability for the jum-

plike plastic deformation of Cu–Be polycrystalline specimens exhibiting a great number of load jumps at liquid helium temperatures.

The typical experimental technique used for such investigations includes the tension (compression) of a specimen at a constant strain rate $\dot{\epsilon}_a$ with the load applied to the specimen being the measured quantity (in some sense, this technique is opposite to the conventional physical experiment in which the external action is preset and the response of the system is measured). The deformation with a given strain rate $\dot{\epsilon}_a$ is a result of the plastic deformation of the specimen with a rate $\dot{\epsilon}$ and the elastic deformation of the specimen–loading machine system with a rate $\dot{\sigma}/M$ (where σ is the mechanical stress and M is the rigidity of the system): $\dot{\epsilon}_a = \dot{\epsilon} + \dot{\sigma}/M$. This relation explains the jumplike character of the deformation in an unstable plastic flow: a dislocation avalanche leads to the relation $\dot{\epsilon} \gg \dot{\epsilon}_a$, and the load applied to the specimen drastically jumps because of the elastic response of the machine; in its turn, this jump leads to the termination of the avalanche process and to the repetition of the load increase cycle and appearance of instability.

Polycrystalline specimens 0.5 mm in diameter and 30 mm in length were cut out of a wire made of an alloy with the composition Cu–12 at. % Be–0.2 at. % Co. The specimens were subjected to tension at 4.2 K ($M \approx 6.2 \times 10^6$ N/m) in their initial state or after their homogenization by annealing at 800°C with a subsequent quenching. The strain rate was varied in the range $\dot{\epsilon}_a = 2.7 \times 10^{-6}$ – 5.4×10^{-2} s⁻¹. The stress–time curves $\sigma(t)$ (t is time) were recorded in a digital form with a frequency of 5–50 Hz. The microstructural state of the crystals changes with deformation, which is reflected by a change in the rate of strain hardening (Fig. 1).

Therefore, the statistical samples were accumulated at the stage of steady-state jumplike plastic deformation ($\varepsilon \geq 5\text{--}10\%$), and the amplitude of load jumps was normalized to the running average (the details of the experimental technique can be found in [8, 12]).

Although the microstructural state and the shape of the stress–time curves cannot be exactly the same for different specimens, the experimental results allow us to determine some common features. At low strain rates, the jumplike stress–time curves have a regular character (see Fig. 1), which manifests itself in the existence of a definite scale of load jumps. Correspondingly, the histograms of the amplitude and duration distributions of the jumps have a peaked form. As the strain rate increases, the distributions become asymmetric: the position of the maximum gradually moves toward the ordinate axis (the probability of small load jumps increases), and at strain rates higher than $\sim 10^{-3} \text{ s}^{-1}$, the histograms are described by monotonically decreasing functions.

The normalized probability density functions obtained for the amplitudes δ and durations τ of load jumps at high strain rates for annealed specimens are adequately described by the power laws $n_\delta \sim \delta^{-x}$ and $n_\tau \sim \tau^{-y}$ (Fig. 2a). Hence, the quantities δ and τ are related as $\delta \sim \tau^h$ (Fig. 2b), where h characterizes the singularity of the stress–time curve at the instant of jump (in the case $h < 1$, a jump with the duration $\tau \rightarrow 0$ has a finite magnitude). For different specimens, the exponents were found to vary within 1–1.5, and the set of exponents for each specimen satisfied the relation $y = h(x - 1) + 1$ (see, e.g., caption to Fig. 2) that follows from simple scaling considerations [13]. The absence of the characteristic scale of deformation processes, which manifests itself in the power-law statistics, points to the possibility of self-organized critical dynamics of the dislocation system. Deviations from the power laws are observed at the edges of the ranges within which the characteristics of the load jumps vary. Presumably, these deviations can be attributed to the lack of statistics for rare large jumps and to the limited sensitivity of measurements. Note that the approximation of the dependence for the durations in Fig. 2a is less convincing than that for the amplitudes. Generally speaking, even in the numerical modeling of the dynamics of self-organized criticality, the distributions of τ exhibit a more noticeable scatter [11]. In the experiment, this is due to the lower accuracy of the τ measurements. An independent verification of the assumption about the self-organized criticality can be provided by the behavior of the energy spectrum of the stress–time curve. According to [13], if the condition $2/h + x \leq 3$ is satisfied, the low-frequency part of the spectrum is described by the dependence $S(f) \sim 1/f^2$, which agrees well with the experimental observations. Therefore, despite the scatter of data and the narrow range of argu-

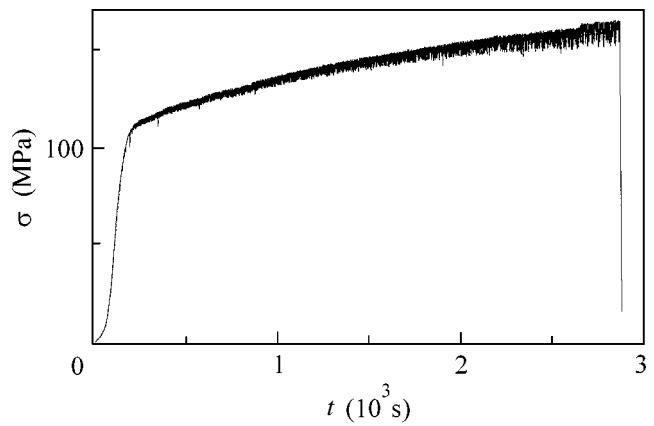


Fig. 1. Stress–time curve obtained for an annealed Cu–Be specimen ($\dot{\varepsilon}_a = 2.7 \times 10^{-4} \text{ s}^{-1}$ and $T = 4.2 \text{ K}$).

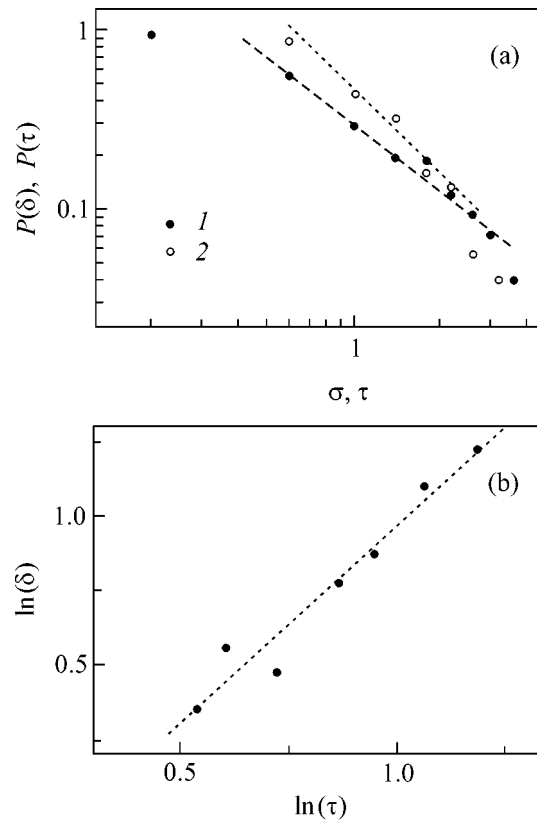


Fig. 2. (a) Normalized probability density functions for the (1) amplitudes δ and (2) durations τ of stress jumps at $\dot{\varepsilon}_a = 2.7 \times 10^{-3} \text{ s}^{-1}$ and (b) the relation between the parameters of stress jumps (the data are averaged for close values of τ). The corresponding estimates of the exponents are $x \approx 1.2$, $y \approx 1.4$, and $h \approx 1.3$ (notation is given in the text).

ment variations in the experimental dependences, the assumption about the self-organized criticality seems to be quite plausible.

One more characteristic feature is associated with the effect of the microstructural state of the crystals. The transition from the histograms with a maximum to monotonic distributions is observed for all specimens; however, in the case of annealed crystals, it occurs at smaller values of $\dot{\epsilon}_a$. By contrast, the monotonic distributions obtained for the initial specimens noticeably deviate from the power laws even for the highest strain rates (see [12]). Since the annealing leads to the relaxation of internal stresses and to crystal softening, this observation agrees well with the fact that, at the initial deformation stage ($\epsilon \leq 5\%$) in the annealed crystals, the asymmetry of distributions is greater than is observed after the strain hardening.

Thus, at certain conditions, the curve statistics obtained for the jumplike plastic deformation of Cu–Be exhibits a scale invariance, giving evidence of the self-organization of the dislocation dynamics. The comparison with the data for the Portevin–Le Chatelier effect showed that the types of distributions and the transitions between them upon varying experimental conditions are qualitatively similar for the two mechanisms of plastic instability [7–9]. This result points to the existence of general laws that govern the instability dynamics. However, the manifestation of the scale-invariant behavior depends on the material and microstructure of the specimens and on the deformation conditions. Therefore, it is of interest to consider the experimental data from the viewpoint of similarity of and difference between the physical mechanisms responsible for the analogous statistical properties of the jumplike plastic deformations. In fact, the scale symmetry is often associated with a universal behavior for which the scaling factors are determined by the fundamental properties of the system and, specifically, by its dimension and symmetry and by the form of the nonlinear dynamical law.

The dislocation glide is discontinuous: it consists of the motion and arrests at localized obstacles. In the case of a thermally activated dislocation motion, the dependence $\sigma(\dot{\epsilon})$ observed at a constant temperature is a monotonically increasing function, because the dislocation waiting time at obstacles is inversely proportional to the strain rate, $t_w \sim 1/\dot{\epsilon}$, and decreases with increasing σ . In alloys, an additional resistance to plastic flow may be caused by the diffusion of impurity atoms toward immobile dislocations. This component of σ decreases with increasing $\dot{\epsilon}$ because of a decrease in the number of impurity atoms that have an opportunity to reach a dislocation. Because of the competition between these two contributions, the dependence $\sigma(\dot{\epsilon})$ becomes *N*-shaped with a negative slope in some interval of $\dot{\epsilon}$. If the strain rate $\dot{\epsilon}_a$ provided by the loading machine corresponds to this interval, an instability similar to relaxation oscillations takes place, as, e.g., in the Gunn effect in a medium with a negative differential conductivity [14]. These concepts lie at the basis of the

models of the Portevin–Le Chatelier effect. The low-temperature jumplike plastic deformation observed in a number of materials, including pure substances, has a different microscopic origin. The theoretically best understood mechanism is the mechanism of thermomechanical instability caused by the relation between the strain rate and the heat release. Namely, at liquid helium temperatures, the energy dissipation that accompanies the dislocation motion may cause considerable local heating in the strained crystal. Since the heating contributes to the activation of dislocations, an avalanche process may take place. An alternative hypotheses was also discussed in the literature, such as, e.g., the nonthermic mechanism based on the concept that the dislocation pile-ups mechanically break through the obstacles. However, these hypotheses were not adequately treated theoretically. From the experiments, it was found that the low-temperature instability is also associated with the *N*-like sensitivity of the flow stress to the strain rate [15] (this also follows from the thermal hypothesis [16]). Therefore, despite the difference in the microscopic nature, the plastic instability mechanisms under consideration can be associated with the same type of nonlinearity typical of the excited media.

In the ideal case of a homogeneous deformation, the instability of the relaxation oscillation type should correspond to periodic load jumps with the same amplitude and duration. The complex behavior of real specimens is caused by the inhomogeneity of plastic flow. Therefore, along with the *N*-shaped response function, the character of the spatial correlation between local strains in the specimen is of fundamental significance. In the case of the Portevin–Le Chatelier effect, the correlation is mainly determined by the elastic stresses associated with the field of elastic strains compensating the incompatibility between the plastic strains in the inhomogeneous flow [7, 8]. Presumably, this mechanism also manifests itself in the low-temperature deformation, because the effect produced by the annealing of specimens on the experimental histograms points to the important role of plastic relaxation of internal stresses. At the same time, it is evident that, at low temperatures, the formation of spatial scales strongly depends on the heat transfer processes. Along with other features of the conditions for dislocation motion and multiplication at low temperatures, this factor may be responsible for the difference in the spatial patterns of the strain localization. For example, at a low strain rate, each load jump observed in the conditions of the Portevin–Le Chatelier effect is usually associated with the formation of a single deformation band (the elastic stresses provide the correlation only at small distances because of the exponential dependence of the plastic strain rate on stress). By contrast, at low temperature, a multiple shear generation is observed in different parts of the specimen.

A possible explanation of the experimental results lies in the consideration of the competition between the characteristic length and time scales, which are deter-

mined by the properties of material and by the deformation conditions [9]. The arguments presented here are of a general character and combine different mechanisms of spatial correlation. When the plastic instability occurs in some part of the crystal, the strain rate in this region (deformation band) becomes higher than in the rest of the crystal and, hence, gives rise to a strain gradient. At a low $\dot{\epsilon}_a$, the inhomogeneity considerably decreases within the time interval between successive load jumps, so that the correlation between them is insignificant and their parameters are distributed near the average ones, which approximately correspond to the relaxation oscillations. At high strain rates, the time between the jumps is insufficient for the relaxation of the strain gradients (remind that $\dot{\epsilon}_a$ was varied within several orders of magnitude). As a result, the correlation length increases and the stress is always close to the critical value for the initiation of a plastic burst at some point, which is typical of the self-organized criticality. This can lead to a repeated formation of new bands and a hierarchical distribution of the load jump parameters without any characteristic scale. Note that, in the case of the Portevin–Le Chatelier effect, an increase in the strain rate is accompanied by the transition from the localization to the propagation of the deformation bands along the crystal [3]. This agrees well with the assumption that the correlation length increases. For the low-temperature deformation, such data are as yet not available. The similarity of the shape (see [7, 17]) and statistics of the stress–time curves obtained for both instability mechanisms is indirect evidence in favor of the possible propagation of the deformation bands in the low-temperature deformation conditions.

Thus, the data obtained from this study characterize the plastically strained crystal as a system in which complex dynamical regimes are possible, and the transitions between these regimes can be controlled by varying the experimental conditions. More definite conclusions concerning the universal properties of plastic instability can presumably be obtained by applying the methods of dynamical and multifractal analyses used earlier for analyzing the Portevin–Le

Chatelier effect [9]. The results of such investigations will be reported elsewhere.

This work was supported by the Russian Foundation for Basic Research (project nos. 01-02-16461, 01-02-16476, 00-15-96703, and 02-02-06352) and INTAS (project no. YSF 01/1-47).

REFERENCES

1. G. Nicolis and I. Prigogine, *Self-Organization in Non-Equilibrium Systems* (Wiley, New York, 1977; Mir, Moscow, 1979).
2. G. A. Malygin, *Usp. Fiz. Nauk* **169**, 979 (1999).
3. L. P. Kubin, C. Fressengeas, and G. Ananthakrishna, in *Dislocations in Solids*, Ed. by F. R. N. Nabarro and J. P. Hirth (Elsevier, 2001), Vol. 11.
4. O. V. Klyavin, *Physics of the Crystal Plasticity at Helium Temperatures* (Nauka, Moscow, 1987).
5. M. A. Lebyodkin, Y. Bréchet, Y. Estrin, and L. P. Kubin, *Phys. Rev. Lett.* **74**, 4758 (1995).
6. G. Ananthakrishna, C. Fressengeas, M. Grosbras, *et al.*, *Scr. Metall. Mater.* **32**, 1731 (1995).
7. M. A. Lebyodkin and L. R. Dunin-Barkovskii, *Zh. Éksp. Teor. Fiz.* **113**, 1816 (1998) [*JETP* **86**, 993 (1998)].
8. M. A. Lebyodkin, L. R. Dunin-Barkovskii, Y. Bréchet, *et al.*, *Acta Mater.* **44**, 2529 (2000).
9. M. S. Bharathi, M. A. Lebyodkin, G. Ananthakrishna, *et al.*, *Phys. Rev. Lett.* **87**, 165508 (2001); *Acta Mater.* **50**, 2813 (2002).
10. D. Ruelle and F. Takens, *Commun. Math. Phys.* **20**, 167 (1971).
11. P. Bak, C. Tang, and K. Wiesenfeld, *Phys. Rev. A* **38**, 364 (1988).
12. M. A. Lebyodkin, L. R. Dunin-Barkovskii, V. S. Bobrov, and V. Gröger, *Scr. Metall. Mater.* **33**, 773 (1995).
13. J. Kertész and L. B. Kiss, *J. Phys. A* **23**, L433 (1990).
14. J. Ganne, *Usp. Fiz. Nauk* **89**, 147 (1966).
15. S. N. Komnik and V. V. Demirski, *Cryst. Res. Technol.* **19**, 863 (1984).
16. G. A. Malygin, *Fiz. Met. Metalloved.* **63**, 864 (1987).
17. Z. Troyanová, V. Gröger, J. Stelzhammer, and G. Bischof, *Mater. Sci. Eng. A* **234–236**, 449 (1997).

Translated by E. Golyamina

Charge Transfer Near the Néel Temperature in $\text{La}_2\text{CuO}_{4+x}$

O. E. Parfenov¹, A. A. Nikonov¹, and S. N. Barilo²

¹ Russian Research Centre Kurchatov Institute, pl. Kurchatova 1, Moscow, 123182 Russia
e-mail: parfenov@issph.kiae.ru

² Institute of Solid-State and Semiconductor Physics, Belarussian Academy of Sciences,
ul. Brovki 17, Minsk, 220072 Belarus

Received October 8, 2002

The electrical resistance and the thermoelectric power in the ab plane of a weakly oxygen-doped $\text{La}_2\text{CuO}_{4+x}$ crystal ($0.001 < x < 0.007$) and its static magnetic susceptibility were studied in the vicinity of antiferromagnetic transition. The electrical resistance and the thermoelectric power behave anomalously near the Néel temperature, indicating that the transport is strongly affected by the establishment of long-range antiferromagnetic order. Analysis of the obtained data allows the conclusion to be drawn that the doping gives rise to a conduction band as a result of the overlap between the wave functions of deep impurity states that are strongly renormalized due to the correlation and polaron effects. © 2002 MAIK “Nauka/Interperiodica”.

PACS numbers: 74.25.Fy; 74.72.Dn

Antiferromagnetic ordering of copper spins in the dielectric phase and spin fluctuations in the metallic state are universal features of the cuprate high- T_c superconductors. For an understanding of the nature of the superconducting state, it is important to know how strong is the interaction of charge carriers with the copper spin subsystem. However, no direct experimental data have been obtained thus far on the interaction of charge carriers in the CuO_2 plane with copper spins. In [1], the deviation from the linear temperature dependence of the resistivity $\rho_{ab}(T)$ in the ab plane of the metallic phase of high- T_c superconductors was considered as a manifestation of the charge spin scattering upon opening a pseudogap in the spectrum of magnetic excitations. It has now become clear [2] that the pseudogap effects primarily relate to the electronic spectrum, so that the separation of charge and spin degrees of freedom in the x - T domain of existence of the pseudogap is not a trivial problem, because the initial states are renormalized in the presence of a high hole concentration in CuO_2 .

Clearly, the influence of the magnetic subsystem on the transport properties manifests itself most strongly in the vicinity of the Néel temperature (T_N), where changes in the spin lattice are the strongest. The surprising thing is that, despite the numerous measurements of electrical resistance along the CuO_2 planes in various single-crystal high- T_c superconductors ($\text{La}_2\text{CuO}_{4+x}$ [3], $\text{La}_{2-y}\text{Sr}_y\text{CuO}_4$ [4], $\text{YBa}_2\text{Cu}_3\text{O}_{6+x}$ [5], and $\text{Bi}_2\text{Sr}_2\text{ErCu}_2\text{O}_8$ [6]), no anomalies were observed for $\rho_{ab}(T)$ near T_N in the appropriate temperature and concentration regions. An important question then arises as to whether the absence of the manifestations of spin ordering in the electrical resistance is evidence of

a weak interaction between the charge carriers and copper spins (in particular, charge carriers may have zero spin or the conduction may occur beyond the CuO_2 planes) or it is an experimental artifact.

This work is devoted to the solution of this question. The temperature dependence of $\rho_{ab}(T)$ was measured near the T_N temperatures of $\text{La}_2\text{CuO}_{4+x}$ single crystals. It is known [7] that $\rho_{ab}(T)$ shows only a weak inflection caused by a change in the conductivity activation energy. For this reason, our measurements of $\rho_{ab}(T)$ were sufficiently accurate for the local conductivity activation energy $E_{ab}(T) = d\ln(\rho_{ab}(T))/dT$ to be determined. Together with the electrical resistance in the ab plane, the thermoelectric power $\alpha_{ab}(T)$ was also measured to separated the contributions to $\rho_{ab}(T)$ from changes in the electronic spectrum and from the scattering mechanism. The $\text{La}_2\text{CuO}_{4+x}$ system was chosen for our measurements not only because it is the simplest system among the high- T_c superconducting cuprates [3] but also because T_N for this system can be determined rather easily from the maximum of magnetic susceptibility [8] due to the hidden weak ferromagnetism of these systems.

Sample quality is highly important for measuring transport properties, because the presence of uncontrolled impurities and defects or the inhomogeneous dopant distribution may shunt the effect. We used high-quality $\text{La}_2\text{CuO}_{4+x}$ single crystals grown under quasi-equilibrium conditions from a solution in melt [9]. The sample orientation and the oxygen content were monitored by single-crystal diffractometry [8]. The results presented in this work were obtained for the samples cut from the same $\text{La}_2\text{CuO}_{4+x}$ single crystal. Note that the room-temperature resistivity of the samples with

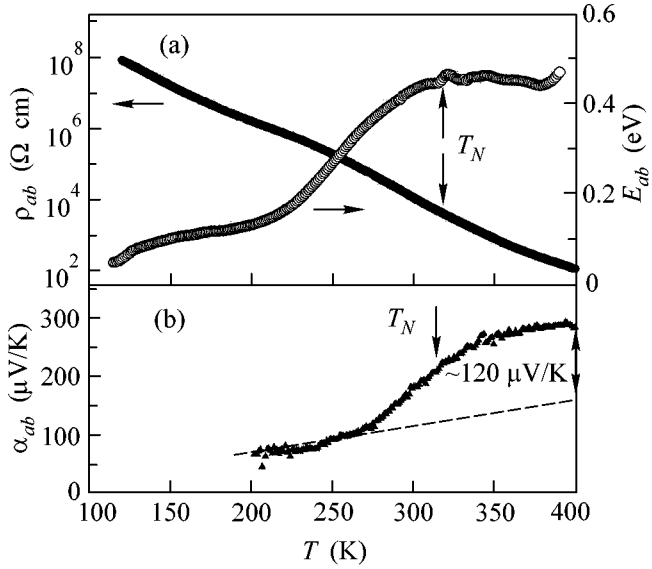


Fig. 1. (a) Electrical resistance $\rho_{ab}(T)$, activation energy $E(T)$, and (b) thermoelectric power $\alpha_{ab}(T)$ in the ab plane of the sample with $T_N = 318$ K and $x \approx 0.0011$.

$x < 0.001$ was higher than 10 m Ω cm. On the one hand, this restricted measurements of transport properties at a low doping level but, on the other hand, indicated the high quality of the crystals used. Measurements of the transport properties were carried out by the standard contact dc methods [10]. Ohmic contacts were obtained by firing silver paste into the samples with a characteristic size of $3 \times 1 \times 0.5$ mm.

The doping with oxygen was performed by annealing at an oxygen partial pressure from 2×10^{-5} to 1 atm and temperatures < 950 K to avoid the formation of oxygen vacancies [11], which irreversibly deteriorate crystal. The following relation was found between the oxygen content in the samples and the oxygen pressure in annealing: $x \approx 7p^{1/6}$, where p is the oxygen pressure in atm. As shown in [11], this dependence is evidence that the degree of oxidation of the extra-stoichiometric oxygen in $\text{La}_2\text{CuO}_{4+x}$ is two; i.e., one excessive oxygen atom creates two holes in the CuO_2 plane.

Our measurements showed that, as regards the transport properties, the domain of existence of the antiferromagnetic phase in $\text{La}_2\text{CuO}_{4+x}$ can conventionally be divided into three regions of oxygen concentration: the “dielectric” region at $0 \leq x \leq 0.0015$ and $T_N > 310$ K, the “semiconductor” region at $0.0015 < x < 0.006$ and $240 \text{ K} < T_N < 310$ K, and the “electronic decay” region at $0.006 < x < 0.012$ and $T_N < 240$ K. In this work, only the dielectric (Fig. 1) and semiconductor (Figs. 2, 3) regions are considered, because the microscopic decay in the third region occurs above T_N , and the observed effects require separate consideration. The dependences of ρ_{ab} , E_{ab} , and α_{ab} on the average dis-

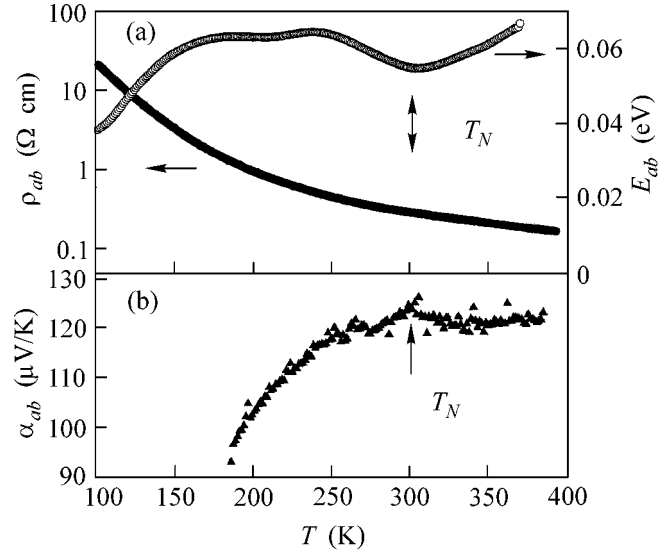


Fig. 2. (a) Electrical resistance $\rho_{ab}(T)$, activation energy $E(T)$, and (b) thermoelectric power $\alpha_{ab}(T)$ in the ab plane of the sample with $T_N = 300$ K and $x \approx 0.0015$.

tance $D(x) \approx 3.8/(2x)^{1/2}$ \AA between the impurity centers in the ab plane at $T = 370$ K are shown in Fig. 4.

When characterizing the behavior of transport properties of $\text{La}_2\text{CuO}_{4+x}$ in the dielectric region, the following should be taken into account. At temperatures higher than T_N (Figs. 1a, 4a), the activation energy $E_{ab} \approx 0.5$ eV is high, nearly constant, and depends exponen-

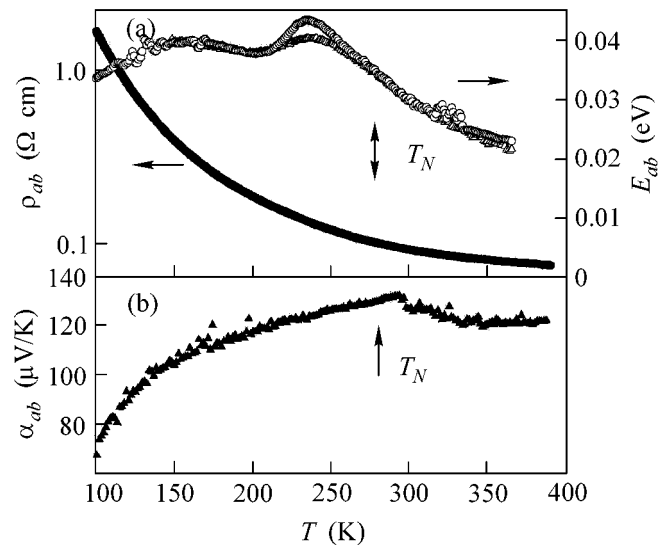


Fig. 3. (a) Electrical resistance $\rho_{ab}(T)$, activation energy $E(T)$, and (b) thermoelectric power $\alpha_{ab}(T)$ in the ab plane of the sample with $T_N = 275$ K and $x \approx 0.0025$. A hysteretic “peak” caused by the electronic decay processes is seen for $E(T)$ near 240 K. The hysteresis is not seen on the scale used in this figure.

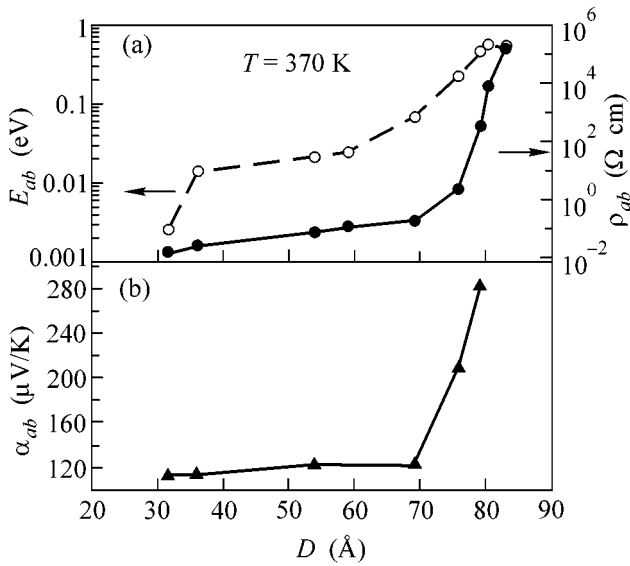


Fig. 4. (a) Electrical resistance ρ_{ab} , resistivity activation energy E , and (b) thermoelectric power α_{ab} at $T = 370$ K as functions of the average distance $D(x)$ between impurity centers in the ab plane.

tially on the distance between the impurity centers (Fig. 4a); i.e., one can write

$$\rho_{ab}(x, T) \sim \exp(AD(x) + E_{ab}/kT), \quad (1)$$

where A is a constant. Taking into account the high activation energy and the metallic behavior of thermoelectric power (Fig. 1b), one can state that such a behavior of electrical resistance is typical of the nonadiabatic high-temperature hopping of small polarons between nearest neighbors [12]. In this case, $A = 2/a$, where a is the characteristic localization radius of a charge carrier. Indeed, using Eq. (1) and the obtained data (Fig. 4a), we can estimate the carrier localization radius at $a \sim 1$ Å. By the term “polaron” one should mean a hole bonded to an acceptor (extra-stoichiometric oxygen), as it follows from the exponential dependence of resistivity on $D(x)$ (Fig. 4a). At the same time, according to [12], $E \approx W_p/2$, where W_p is the polarization energy, which can be estimated as

$$W_p = \frac{e^2}{2\epsilon_p a}, \quad (2)$$

where $1/\epsilon_p = 1/\epsilon_\infty - 1/\epsilon_0$ is the difference of the inverse optical and static dielectric constants and e is the elementary charge. According to [3], $1/\epsilon_p \approx 1/6$ at $x \approx 0$. At small x , W_p in our samples reaches a value of ≈ 1 eV, which is consistent, according to Eq. (2), with the smallness of the charge localization radius.

At the Néel temperature, the resistivity curve is bent due to a decrease in the activation energy $E_{ab}(T)$ in the antiferromagnetic phase (Fig. 1a). It is conceivable that this is an indication that the radius of localized states

increases, according to Eq. (2), by several times upon the ordering of copper spins.

The thermoelectric power $\alpha_{ab}(T)$ changes linearly with temperature at $T < 250$ K and $T > 350$ K in the dielectric region and decreases by approximately 120 μ V/K near the T_N temperature (Fig. 1b). Such a behavior can be explained by the polaron hopping transport [12] in the presence of charge-carrier interaction with a magnetic lattice. For the polaron transport, a contribution from the polaron kinetic energy to the thermoelectric power is ignored, so that the thermoelectric power can be written in the thermodynamic approximation [10] as a change in the entropy upon the transfer of charge $-e$:

$$e\alpha_{ab}(T) = \Delta S_c + \Delta S_s + \Delta S_o, \quad (3)$$

where ΔS_c , ΔS_s , and ΔS_o are changes in the configurational, spin, and orbital entropies, respectively. The spin and orbital contributions $\Delta S_s/e = \Delta S_o/e = k/e \ln 2 \approx 60$ μ V/K disappear upon the three-dimensional ordering of the Cu^{2+} spins below T_N [13], if the spin–spin and spin–orbit interactions are taken into account. We observed this not only in the dielectric (Fig. 1b) but also in the semiconductor (Figs. 2b, 3b) regions. The contribution of ΔS_c to $\alpha_{ab}(T)$ changes with temperature almost linearly in the regime of nearest-neighbor hopping between impurity centers [12, 14] for a broad, compared to the temperature range used, energy distribution of acceptor levels.

As the concentration of the extra-stoichiometric oxygen increases, the dependence of the resistivity and thermoelectric power on the temperature (Figs. 2, 3) and oxygen concentration (Fig. 4) weakens. We treat the bends in the plots of thermoelectric power, resistivity, and its activation energy vs. $D(x)$ (Fig. 4) as a manifestation of the electronic transition from the dielectric to the semiconductor phase.

In the semiconductor region above T_N , the thermoelectric power is equal to ≈ 120 μ V/K and does not change with temperature and oxygen concentration (Figs. 2–4); i.e., the contribution to $\alpha_{ab}(T)$ comes only from ΔS_s and ΔS_o . This indicates that the carrier spins remain free above T_N , despite the strong antiferromagnetic fluctuations. The lack of activation contribution to $\alpha_{ab}(T)$ allows one to state, when characterizing the kinetic properties of the semiconductor region, that transport occurs near the Fermi level and the resistivity activation energy has a purely kinetic character and is mainly determined by the polaron shift W_p . In other words, we have the polaron hopping conduction, as in the dielectric region, but the conduction is due not to small but to large polarons. Indeed, for the sample with $T_N = 300$ K one has $W_p \approx 2E_{ab} \approx 0.1$ eV and, according to Eq. (2), $a \approx 7$ Å; i.e., the hole localization region is larger than the lattice constant.

We assume that the charge-carrier transport in the semiconductor region proceeds through the impurity

band, although not over the free states, as in the dielectric phase, but over the occupied states. Theoretically, this process is quite realistic. Due to the strong polaron effect, the energy of Coulomb repulsion between two carriers on the same center can be strongly lowered [15], so that the upper and lower Hubbard bands overlap. In the case of low doping, when the resonant broadening is smaller than the “classical” broadening, the impurity states are localized, and conduction has the hopping character. In the Hubbard model, the density $N(E)$ of impurity states near the Fermi level E_F is approximately symmetric about its position. Then the fact that the contribution to the thermoelectric power from the configurational entropy is not observed experimentally in the semiconductor region is easily understood. For instance, according to [12, 14], $\Delta S_c \sim d \ln N(E)/dE|_{E_F} \approx 0$, and only the term $\Delta S_s + \Delta S_o$ remains in Eq. (3).

The electrical resistance anomaly near T_N (Fig. 2a) differs substantially from the anomaly in the dielectric region. Upon doping, it disappears as the boundary of electronic decay region is approached (Fig. 3a). The changes in the form of $E(T)$ dependence are likely caused by a change in the transport regime from the nonadiabatic hopping of small bound polarons between the free acceptor states to the hopping of large polarons between the occupied states of impurity band. Therefore, our measurements show that the resistivity anomalies near T_N are caused by the polaron effect.

Our measurements of electrical resistance of the $\text{La}_2\text{CuO}_{4+x}$ crystals with $T_N \leq 310$ K roughly correlate with the data reported in [3]. However, the conclusion drawn in [3] about the applicability of the shallow-impurity model to $\text{La}_2\text{CuO}_{4+x}$ is incompatible with our measurements of thermoelectric power and with the data on electrical resistance in the dielectric region. We believe that the deep-impurity model [16, 17], according to which the impurity conduction band is formed deep inside the charge-transfer gap (≈ 2 eV) through the overlap of impurity wave functions strongly renormalized due to the correlation and polaron effects, is the most realistic model for the explanation of the transport properties of $\text{La}_2\text{CuO}_{4+x}$.

We are grateful to A.A. Zakharov and A.A. Chernyshov for attention to the work and helpful discussions. This work was supported by the State Contract no. 107-1(00)-II) on the program “Microlayering.” In Minsk, the work was supported in part by INTAS (grant no. 96-0410).

REFERENCES

1. T. Ito, K. Takenaka, and S. Uchida, *Phys. Rev. Lett.* **70**, 3995 (1993).
2. J. Orenstein and A. J. Millis, *Science* **288**, 468 (2000).
3. M. A. Kastner, R. J. Birgenau, G. Shirane, and Y. Endoh, *Rev. Mod. Phys.* **70**, 897 (1998).
4. Y. Ando, A. N. Lavrov, S. Komiya, *et al.*, *Phys. Rev. Lett.* **87**, 17001 (2001).
5. A. N. Lavrov, Y. Ando, K. Segawa, and J. Takeya, *Phys. Rev. Lett.* **83**, 1419 (1999).
6. T. Kitajima, T. Takayanagi, T. Takemura, and I. Terasakii, *J. Phys.: Condens. Matter* **11**, 3169 (1999).
7. É. L. Nagaev, *Physics of Magnetic Semiconductors* (Nauka, Moscow, 1979).
8. A. A. Nikonov and O. E. Parfenov, *Pis'ma Zh. Éksp. Teor. Fiz.* **72**, 797 (2000) [*JETP Lett.* **72**, 550 (2000)].
9. S. N. Barilo, D. I. Zhigunov, S. V. Shiryaev, *et al.*, *Poverkhnost*, No. 3, 20 (2002).
10. A. F. Ioffe, *Physics of Semiconductors* (Akad. Nauk SSSR, Leningrad, 1957; Infosearch, London, 1960).
11. F. Cordero and R. Cantelli, *Physica C (Amsterdam)* **312**, 213 (1999).
12. I. G. Austin and N. F. Mott, *Adv. Phys.* **18**, 41 (1969).
13. J. R. Cooper, B. Alavi, L. W. Zhou, *et al.*, *Phys. Rev. B* **35**, 8794 (1987).
14. T. E. Whall, *J. Phys. C* **14**, L887 (1981).
15. S. D. Baranovskii and V. G. Karpov, *Fiz. Tekh. Poluprovodn. (Leningrad)* **21**, 3 (1987) [*Sov. Phys. Semicond.* **21**, 1 (1987)].
16. A. O. Gogolin and A. S. Ioselevich, *Zh. Éksp. Teor. Fiz.* **98**, 681 (1990) [*Sov. Phys. JETP* **71**, 380 (1990)].
17. K. M. Rabe and R. N. Bhatt, *J. Appl. Phys.* **69**, 4508 (1991).

Translated by V. Sakun

Magnetic Bloch States and Hall Conductivity of a Two-Dimensional Electron Gas in a Periodic Potential without Inversion Center

V. Ya. Demikhovskii and A. A. Perov

Nizhni Novgorod State University, Nizhni Novgorod, 603950 Russia

Received October 15, 2002

Quantum states of 2D electrons are studied in a periodic potential without inversion center in the presence of a magnetic field. It is shown that the energy spectrum in magnetic subbands is not symmetric about the center of magnetic Brillouin zone $E(\mathbf{k}) \neq E(-\mathbf{k})$. Singularities (phase branching points) of the electron wave function, which determine the quantization law of Hall conductivity σ_{xy} , are studied in the \mathbf{k} space. It is found that a sharp change takes place in the number of points in the magnetic Brillouin zone and in the corresponding values of topological invariants determining the Hall conductivity of filled subbands. It is noted that the longitudinal conductivity of a lattice without inversion center placed in a magnetic field is not invariant with respect to a change in sign of the electric field, and a photovoltaic effect must arise in an ac electromagnetic field. © 2002 MAIK "Nauka/Interperiodica".

PACS numbers: 73.20.-r; 73.43.Cd

It is known that a uniform magnetic field and a periodic potential essentially differ in the character of their action on an electron. In particular, a magnetic field forms discrete levels (Landau levels), whereas a periodic potential leads to the formation of energy bands. As a result, the spectrum of an electron moving in a magnetic field exhibits an extremely interesting and rich structure, which received the name Hofstadter butterfly [1, 2].

Magnetic quantum states of a Bloch electron were studied in detail in the tight- and weak-binding approximations for potentials $V(\mathbf{r})$ differing in symmetry (see, for example, [3, 4] and also [5–7]). A number of experimental works were also devoted to this problem [8]. In this case, however, it was always assumed that the periodic potential possess symmetry about the inversion of coordinates, that is, $V(\mathbf{r}) = V(-\mathbf{r})$.

In a zero magnetic field and a periodic potential with or without an inversion center, the Bloch electron energy is invariant with respect to a change in sign of quasi-momentum $E(\mathbf{k}) = E(-\mathbf{k})$. This symmetry is a consequence of the invariance of the stationary Schrödinger equation with respect to time reversal. In a magnetic field, the $t \rightarrow -t$ symmetry is violated. Therefore, it is natural to assume that the energy of a Bloch electron moving in crystal without an inversion center in the presence of a magnetic field will not be an even function of the quasi-momentum determined in the magnetic Brillouin zone (MBZ). Because of this, it may be expected that a crystal without inversion center in the \mathbf{k} space, that is, $E(\mathbf{k}) \neq E(-\mathbf{k})$, possesses unusual physical properties in a static magnetic field.

It should be noted that the symmetry of energy spectrum in the \mathbf{k} space in crystals without inversion center can also be violated as a result of spin-orbit interaction. Even in zero magnetic field, the electron energy in such crystals depends on the spin orientation, and the Kramers degeneracy $E(\mathbf{k}, 1/2) = E(-\mathbf{k}, -1/2)$ takes place. This fact leads to a number of observable effects, one of which is the circular photovoltaic effect in a 2D electron gas [9]. However, such effects are always small on the Brillouin zone scale because of the smallness of spin-orbit interaction [10]. Below, we will show that the energy spectrum of magnetic subbands of a spinless particle can undergo drastic changes in the entire MBZ in the absence of inversion center in the periodic potential.

The Hamiltonian of an electron in a uniform magnetic field and in the field of a two-dimensional periodic potential will be written in the form

$$\hat{H} = \hat{H}_0 + V(x, y), \quad (1)$$

where

$$\hat{H}_0 = \frac{1}{2m^*} \left(\hat{\mathbf{p}} - \frac{e\mathbf{A}}{c} \right)^2 \quad (2)$$

is the Hamiltonian of an electron in a uniform magnetic field. Here, c is the velocity of light, e is the electron charge, and m^* is the effective mass. From here on, the vector potential \mathbf{A} of the magnetic field is taken in the Landau gauge $\mathbf{A} = (0, Hx, 0)$, so that $\mathbf{H} \parallel z$. The model

periodic potential of a lattice without inversion center will be written in the form

$$V(x, y) = V_1 \cos^2(\pi x/a) \cos^2(\pi y/a) + V_2 [\sin(2\pi x/a) + \sin(2\pi y/a)], \quad (3)$$

where a is the period of the potential (see Fig. 1). Here, the parameter V_2 determines the degree of violation of the spatial inversion symmetry of lattice (3). At $V_2 = 0$, the symmetry about inversion is restored. In what follows, we will assume that amplitude V_1 is fixed.

The character and structure of the eigenstates of Hamiltonian (1) are determined by the magnetic flux through a unit cell of the lattice [11]. If this flux (measured in terms of flux quanta Φ_0) is equal to a rational number

$$\frac{\Phi}{\Phi_0} = \frac{p}{q} = \frac{|e|Ha^2}{2\pi\hbar c}, \quad p, q \text{ are integer numbers}, \quad (4)$$

then the wave function is an eigenfunction of the magnetic translation operator and obeys the Bloch–Peierls conditions

$$\Psi_{\mathbf{k}}(x, y) = \Psi_{\mathbf{k}}(x + qa, y + a) e^{-ik_x qa} e^{-ik_y a} e^{-2\pi i p y/a}. \quad (5)$$

Here, vectors $\mathbf{a}_m = \{m_1 qa, m_2 a\}$, (m_1, m_2 are integer numbers) specify the positions of sites of the so-called magnetic lattice of the crystal and $-\pi/qa \leq k_x \leq \pi/qa$, $-\pi/a \leq k_y \leq \pi/a$.

If the inequalities

$$\hbar\omega_c \gg V_1, V_2; \quad l_H \ll a \quad (6)$$

are fulfilled (here, l_H and ω_c are magnetic length and cyclotron frequency, respectively), the electron quantum states can be calculated within the framework of the perturbation theory, that is, without taking into account the interaction between the Landau levels. Simple estimates show that, at $a = 80$ nm, condition $p/q = 3$ is fulfilled in magnetic field $H \approx 2 \times 10^4$ Oe, and conditions (6) will be true for amplitudes $V_1, V_2 \approx 1$ meV. The wave function of an electron in the μ th magnetic subband obeying Eq. (5) can be expanded in oscillator functions ϕ_N of the N th Landau level [3]

$$\begin{aligned} & \Psi_{\mathbf{k}, \mu}^N(x, y) \\ &= \sum_{n=1}^p C_{n\mu}^N(\mathbf{k}) \sum_{l=-\infty}^{+\infty} \phi_N \left[\frac{x - x_0 - lqa - nqa/p}{l_H} \right] \\ & \quad \times e^{ik_y y} e^{ik_x(lqa + nqa/p)} e^{2\pi i y(lp + n)/a}, \end{aligned} \quad (7)$$

where $x_0 = c\hbar k_y / |e|H = k_y l_H^2$. Note that condition (5) will be fulfilled if the expansion coefficients in Eq. (7) obey the relationships

$$C_{n+p, \mu}^N(\mathbf{k}) = C_{n\mu}^N(\mathbf{k}). \quad (8)$$

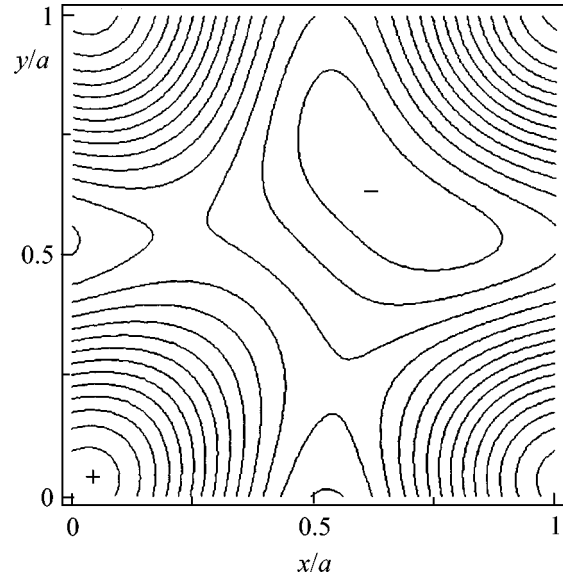


Fig. 1. Lines of constant potential values $V(x, y)$ (Eq. (3)) in a crystal lattice unit cell at $V_2/V_1 = 0.1$. Signs “+” and “-” correspond to the maximum and minimum of the potential.

In the representation of symmetrized linear combinations of Landau functions (7), the stationary Schrödinger equation $\hat{H}\Psi = E\Psi$ takes the form

$$H_{nm}^N(\mathbf{k}) C_{m\mu}^N(\mathbf{k}) = [E_N^0(p/q)\delta_{nm} + V_{nm}^N(p/q, \mathbf{k})] C_{m\mu}^N = E_{\mu}^N(\mathbf{k}) C_{n\mu}^N(\mathbf{k}), \quad (9)$$

where $E_N^0 = \hbar\omega_c(N + 1/2)$. Matrix V_{nm}^N of dimension $(p \times p)$ in Eq. (9) has the following structure:

$$V_{nm}^N = \begin{pmatrix} D_1 & M_1 & 0 & \dots & \dots & 0 & M_p^* \\ M_1^* & D_2 & M_2 & 0 & \dots & \dots & 0 \\ \dots & \dots & \dots & \dots & \dots & \dots & \dots \\ \dots & 0 & M_{n-1}^* & D_n & M_n & 0 & \dots \\ \dots & \dots & \dots & \dots & \dots & \dots & \dots \\ M_p & 0 & \dots & \dots & 0 & M_{p-1}^* & D_p \end{pmatrix} \quad (10)$$

with diagonal elements

$$D_n = \left[\frac{V_1}{4} \cos\left(2\pi n \frac{q}{p} + \frac{qk_y a}{p}\right) \right. \quad (11a)$$

$$\left. + V_2 \sin\left(2\pi n \frac{q}{p} + \frac{qk_y a}{p}\right) \right] \exp\left(-\frac{\pi q}{2p}\right) L_N^0\left(\frac{\pi q}{p}\right)$$

and off-diagonal elements

$$M_n = \frac{1}{2} \left[\frac{V_1}{4} - iV_2 \right] \exp\left(i \frac{k_x qa}{p}\right) \exp\left(-\frac{\pi q}{2p}\right) L_N^0\left(\frac{\pi q}{p}\right)$$

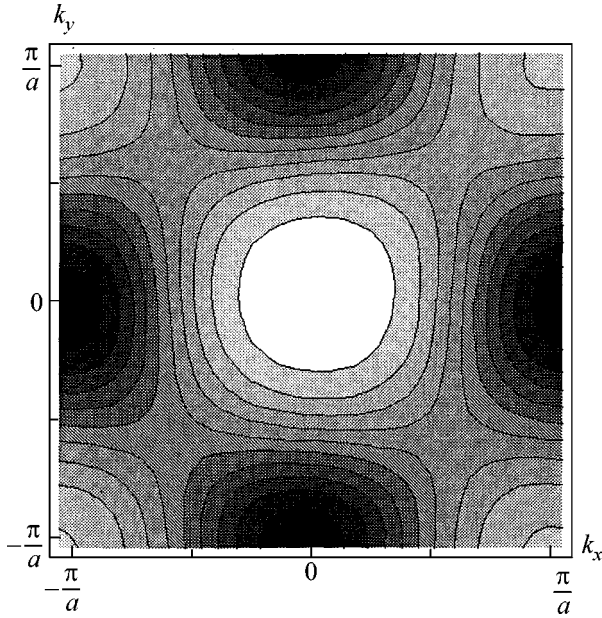


Fig. 2. Isoenergetic lines $E_1^1(\mathbf{k}) = \text{const}$ in the lowest magnetic subband related to the first Landau level $N = 1$ at $V_2/V_1 = 0.1$, $p/q = 3/1$.

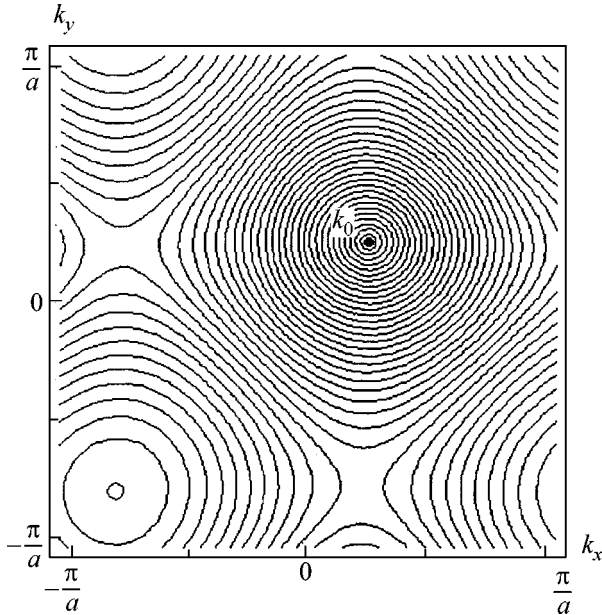


Fig. 3. Isoenergetic lines $E_1^0(\mathbf{k}) = \text{const}$ in the lowest magnetic subband of the zero Landau level $N = 0$ at $(V_2/V_1)^{cr} = 0.051706$, $p/q = 3/1$. The value of $E_1^0(\mathbf{k}_0)$ reaches a maximum at the point \mathbf{k}_0 at which magnetic subbands touch each other.

$$+ \frac{V_1}{8} \cos\left(2\pi\left[n + \frac{1}{2}\right]\frac{q}{p} + \frac{qk_y a}{p}\right) \exp\left(i\frac{k_x q a}{p}\right) \quad (11b)$$

$$\times \exp\left(-\frac{\pi q}{p}\right) L_N^0\left(\frac{2\pi q}{p}\right),$$

where $L_N^0(\xi)$ is a Laguerre polynomial. Thus, the periodic potential leads to the splitting of Landau levels into p magnetic subbands for rational values of the number of magnetic flux quanta. It should be noted that the system of Eqs. (9) determined according to Eqs. (10) and (11) is not periodic in p/q with a period of 1, as it takes place for the standard Harper's equation [2].

The energy spectrum and the eigenvector components $C_{n\mu}^N(\mathbf{k})$ can be calculated analytically for simple rational values of p/q . Our calculations of energy spectrum demonstrated the absence of an inversion center in the \mathbf{k} space for functions $E_\mu(\mathbf{k})$ assigned to different magnetic subbands. A typical arrangement of isoenergetic lines in the MBZ in the lowest of the three magnetic subbands ($p/q = 3/1$) split off from the first Landau level $N = 1$ is shown in Fig. 2. Here, the light areas correspond to larger energy values in the subband.

It should be noted that, as the magnetic field direction is inverted ($\mathbf{H} \rightarrow -\mathbf{H}$), the spectrum, as expected, changes in the following way:

$$E_\mu(\mathbf{k}, \mathbf{H}) = E_\mu(-\mathbf{k}, -\mathbf{H}).$$

At the same time, energies

$$E_\mu\left(k_x, \frac{\pi}{a}\right) = E_\mu\left(k_x, -\frac{\pi}{a}\right);$$

$$E_\mu\left(\frac{\pi}{qa}, k_y\right) = E_\mu\left(-\frac{\pi}{qa}, k_y\right),$$

and the corresponding partial derivatives $\partial E/\partial k_\alpha$ ($\alpha = x, y$) are equal at the opposite boundaries of the MBZ. At the center and at the boundaries, $\partial E/\partial k_\alpha$ are nonzero. The structure of energy spectrum must evidently depend on parameter V_2 . In particular, we found that, at a certain critical value of V_2 , the energy gap separating two neighboring subbands disappears, and surfaces $E_\mu^N(\mathbf{k})$ touch each other at a certain \mathbf{k}_0 lying on the diagonal of MBZ. Figure 3 displays the plot of isoenergetic lines for the lowest magnetic subband $E_1^0(\mathbf{k})$ split off from the zero Landau level $N = 0$ at $p/q = 3/1$ and the critical value of the ratio $(V_2/V_1)^{cr} = 0.051706$. With a further increase in parameter V_2 , this degeneracy disappears, and the neighboring subbands remain separated by an energy gap. Below, it will be shown that at the critical value V_2 , that is, at the point of gap collapse a sudden change takes place in the singularities of the eigenvector $C_{n\mu}^N(\mathbf{k})$ of the system of Eqs. (9) in the \mathbf{k} space, as well as in the topological invariants determining the Hall conductivity of the corresponding subbands.

Coefficients $C_{n\mu}^N(\mathbf{k})$ can be chosen proportional to the algebraic adjunct $D_{jn}(\mathbf{k})$ of any (for example, j th) row of the secular determinant of the system of Eqs. (9)

at $E = E_\mu(\mathbf{k})$. According to [12], the components of a normalized eigenvector can be presented in the form

$$C_n^{(j)}(\mathbf{k}) = R_n^{(j)}(\mathbf{k}) \exp(i\phi_n^{(j)}(\mathbf{k})),$$

$$R_n^{(j)}(\mathbf{k}) = \left(D_{nn}(\mathbf{k}) / \sum_{s=1}^p D_{ss}(\mathbf{k}) \right)^{1/2}, \quad n \neq j. \quad (12)$$

In Eqs. (12), $D_{mn}(\mathbf{k})$ is the algebraic adjunct to the matrix element $[H_{nn}^N - E_\mu^N]$, and the phase $\phi_n^{(j)}(\mathbf{k})$ is determined by the relationships

$$\cos \phi_n^{(j)} = \frac{\text{Re} D_{jn}}{|D_{jn}|}, \quad \sin \phi_n^{(j)} = \frac{\text{Im} D_{jn}}{|D_{jn}|}, \quad n \neq j. \quad (13)$$

It can be shown that component $C_j^{(j)}(\mathbf{k})$ is a purely real function, and it vanishes at some special points \mathbf{k}_m of the extended magnetic Brillouin zone $-\pi/qa \leq k_x \leq \pi/qa$, $-\pi p/qa \leq k_y \leq \pi p/qa$. The other components $C_n^{(j)}(\mathbf{k}_m)$ ($n \neq j$) have no definite limit at $\mathbf{k} \rightarrow \mathbf{k}_m$, and \mathbf{k}_m are phase branching points for these components. Note that the notion of extended MBZ was introduced by Usov [12]. From here on, the superscript in parentheses will specify the representation number (that is, the row number), and we will omit the indices of magnetic subband μ and Landau level N .

The properties of the spectrum and wave functions of magnetic Bloch states in a periodic potential without an inversion center must essentially affect the transport and optical characteristics of a 2D electron gas. Below, we will consider the specific features of the quantization law of 2D Hall conductivity in crystals with broken inversion symmetry. The Hall conductivity of the fully occupied magnetic subbands separated by energy gaps was calculated in [3, 13]. In works by Novikov *et al.* [14], the topological nature of the singularities of eigenfunctions corresponding to magnetic subbands was discussed. Kohmoto showed that the quantized Hall conductivity of a magnetic subband is determined by the topological singularities of wave function [15], and in terms of e^2/h units this conductivity is equal to the first Chern number taken with the opposite sign. However, Kohmoto gave no explicit equations for the calculations of conductivity. This problem was solved by Usov [12], who found interrelation between the Hall conductivity σ_{xy} of a subband and wave-function singularities (phase branching points in the \mathbf{k} space). The explicit equation for the conductivity of the μ th magnetic subband corresponding to the N th Landau level takes the form [12]

$$\sigma_{xy} = -\frac{e^2}{h} \left[\frac{1}{p} + \frac{q}{p} \sum_{\mathbf{k}_m} S(\mathbf{k}_m) \right]. \quad (14)$$

This equation is a direct consequence of the Kubo formula. Integer numbers $S(\mathbf{k}_m)$ of a given subband deter-

mine the phase incursion $\phi_n^{(j)}(\mathbf{k})$ for coefficients $C_n^{(j)}(\mathbf{k})$ in Eq. (7) (in 2π units) in tracing the points \mathbf{k}_m in the negative direction (clockwise).

We performed calculations of the Hall conductivity of magnetic subbands at $p/q = 3/1$ in the potential given by Eq. (3). To calculate the components of eigenvectors of the Hamiltonian given by Eq. (1), we selected the representation of the first row in the secular determinant of the system of Eqs. (9). Sections and singularities of function $C_1^{(1)}(\mathbf{k})$ in the extended MBZ for the lowest of the three magnetic subbands of the zero Landau level are given in Figs. 4a, 4b. The main computational parameters are given in the caption to the figure. The values of the ratio V_2/V_1 in Figs. 4a and 4b are, respectively, lower and higher than the critical value.

The two singularities where $C_1^{(1)}(\mathbf{k}) = 0$ (see Fig. 4a) are marked with letters *A* and *B*. When tracing each of these points along the path shown in the figure, the phases of each of the components $C_2^{(1)}(\mathbf{k})$ and $C_3^{(1)}(\mathbf{k})$ change by $+2\pi$. Thus, $S(\mathbf{k}_A) = S(\mathbf{k}_B) = 1$, and, according to Eq. (14), $\sigma_{xy} = -e^2/h$. The Hall conductivities of the other magnetic subbands can be calculated in a similar way. These conductivities are zero for the computational parameters indicated in Fig. 4a.

When the quantities V_2 are changed, singularities *A* and *B* shift in the extended Brillouin zone, and small changes in V_2 correspond to small displacements of singularities. In accordance with the topological nature of Eq. (14), the conductivity σ_{xy} changes only at the moment of tangency (degeneracy of the spectrum at point \mathbf{k}_0) of the neighboring subbands. As the parameter V_2 reaches the critical value, two neighboring (in our case, lower and middle) magnetic subbands of the zero level under consideration touch each other at a certain point of the MBZ. Singularities *A* and *B* disappear immediately [that is, now $C_1^{(1)}(\mathbf{k})$ does not vanish at these points]. Note that these points do not annihilate and do not go into the boundary of the extended MBZ. Simultaneously, a new singularity appears at the point where the component $C_1^{(1)}(\mathbf{k})$, designated in Fig. 4b as point *C*, vanishes. The position of the local minimum of $C_1^{(1)}(\mathbf{k})$ (the nucleus of singularity *C*) is marked with an arrow in Fig. 4a. In tracing point *C* along the contour indicated in Fig. 4b, the phase of each of the components $C_2^{(1)}(\mathbf{k})$ and $C_3^{(1)}(\mathbf{k})$ changes by -2π , and, as a consequence of Eq. (14), the contribution to the conductivity of the Landau level $N = 0$ from the lowest magnetic subband related to this level is zero. It can be shown that a contribution to the conductivity equal to $-e^2/h$ will be given now by the middle magnetic subband $E_2(\mathbf{k})$, which touches the lowest $E_1(\mathbf{k})$ at the critical value V_2^{cr} . At the same time, it is evident that the

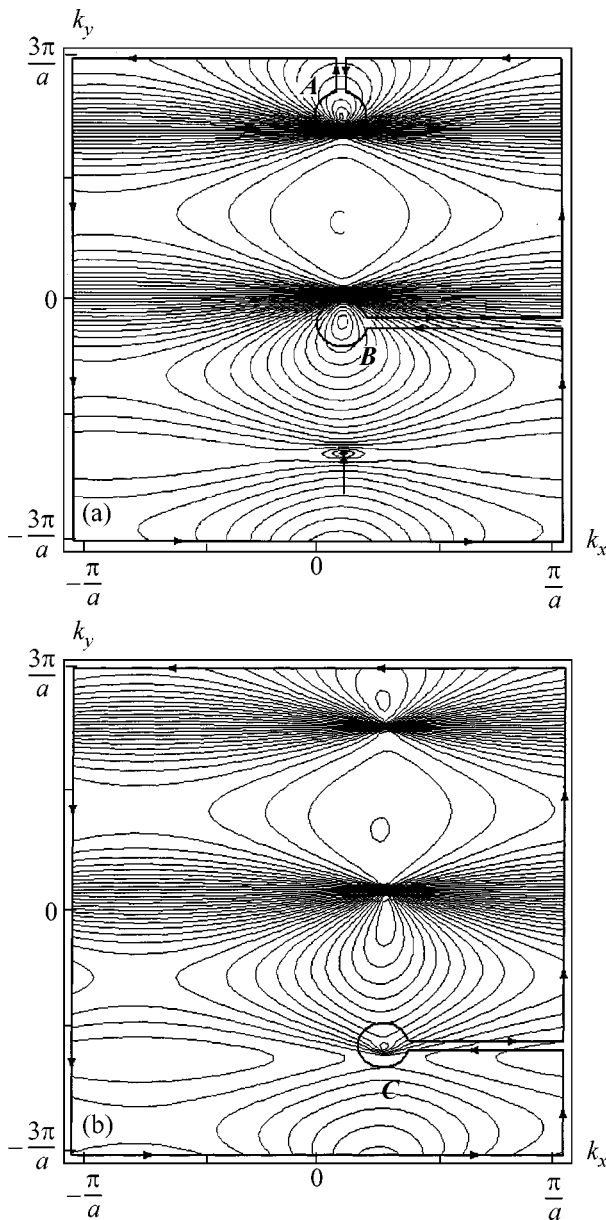


Fig. 4. Contourplots and singularities of the real function $C_1^{(1)}(\mathbf{k})$ in an extended MBZ for $N=0$, $p/q=3/1$: (a) $V_2/V_1 = 0.02$; (b) $V_2/V_1 = 0.06$.

change in the amplitude of the potential V_1 at $V_2 = 0$ cannot lead to a change in the quantization law for Hall conductivity. Thus, in crystals without an inversion center, a new quantization rule is fulfilled for the Hall conductivity, and its value changes abruptly at a certain critical value of parameter V_2 .

Note in conclusion that the absence of spectrum symmetry in the \mathbf{k} space must lead to a number of other observable effects. Thus, it can be expected that the longitudinal conductivity σ_{xx} will not be invariant about a change in sign of a constant electric field E because of the absence of an inversion center in the \mathbf{k} space. A photovoltaic effect similar to that described in [9] must arise in the situation under consideration in an ac electromagnetic field. These effects will be considered in a separate publication.

This work was supported by the Russian Foundation for Basic Research (project no. 01-02-17102), by the Ministry of Education of the Russian Federation (project nos. E00-3.1-413 and PD02-1.2-147), and by the Program "Russian Universities."

REFERENCES

1. M. Ya. Azbel, Zh. Éksp. Teor. Fiz. **46**, 929 (1964) [Sov. Phys. JETP **19**, 634 (1964)].
2. D. R. Hofstadter, Phys. Rev. B **14**, 2239 (1976).
3. D. J. Thouless, M. Kohmoto, M. P. Nightingale, *et al.*, Phys. Rev. Lett. **49**, 405 (1982).
4. H. Silberbauer, J. Phys.: Condens. Matter **4**, 7355 (1992).
5. V. Ya. Demikhovskii and A. A. Perov, Fiz. Tverd. Tela (St. Petersburg) **40**, 1134 (1998) [Phys. Solid State **40**, 1035 (1998)]; Zh. Éksp. Teor. Fiz. **114**, 1795 (1998) [JETP **87**, 973 (1998)].
6. V. Ya. Demikhovskii and A. A. Perov, Phys. Low-Dimens. Semicond. Struct. **7/8**, 135 (1998).
7. V. Ya. Demikhovskii, A. A. Perov, and D. V. Khomitsky, Phys. Lett. A **267**, 408 (2000).
8. T. Schlösser, K. Ensslin, J. P. Kotthaus, *et al.*, Semicond. Sci. Technol. **11**, 1582 (1996); C. Albrecht, J. H. Smet, K. von Klitzing, *et al.*, Phys. Rev. Lett. **86**, 147 (2001).
9. S. D. Ganichev, E. L. Ivchenko, S. N. Danilov, *et al.*, Phys. Rev. Lett. **86**, 4358 (2001).
10. Yu. A. Bychkov and É. I. Rashba, Pis'ma Zh. Éksp. Teor. Fiz. **39**, 66 (1984) [JETP Lett. **39**, 78 (1984)].
11. E. M. Lifshits and L. P. Pitaevskii, *Course of Theoretical Physics*, Vol. 5: *Statistical Physics* (Nauka, Moscow, 1978; Pergamon, New York, 1980), Part 2.
12. N. A. Usov, Zh. Éksp. Teor. Fiz. **94** (12), 305 (1988) [Sov. Phys. JETP **67**, 2565 (1988)].
13. P. Streda, J. Phys. C **15**, L717 (1982).
14. B. A. Dubrovin and S. P. Novikov, Zh. Éksp. Teor. Fiz. **79**, 1006 (1980) [Sov. Phys. JETP **52**, 511 (1980)]; S. P. Novikov, Dokl. Akad. Nauk SSSR **257**, 538 (1981).
15. M. Kohmoto, Ann. Phys. (N.Y.) **160**, 343 (1985).

Translated by A. Bagatur'yants

Anisotropic Multicomponent Terahertz Photoconductivity in Quantum Hall Systems

N. G. Kalugin^{*},¹, Yu. B. Vasil'ev^{**}, S. D. Suchalkin^{**}, G. Nachtwei^{*},
B. E. Sagol^{*}, G. Hein^{***}, and K. Eberl^{****}

^{*} Institut für Technische Physik, TU-Braunschweig, D-38106 Braunschweig, Germany
e-mail: n.kalugin@tu-bs.de

^{**} Ioffe Physicotechnical Institute, Russian Academy of Sciences, St. Petersburg, 194021 Russia

^{***} PTB-Braunschweig, D-38116 Braunschweig, Germany

^{****} Max-Planck-Institut für Festkörperforschung, 70569 Stuttgart, Germany

Received October 17, 2002

The decay times of the terahertz photoconductivity signal are studied for samples in the quantum Hall regime. The photoconductivity signal has both the longitudinal components caused by the photoinduced change in the longitudinal resistance and the transverse components due to the photoinduced transverse current. The signal kinetics are qualitatively different for samples with relatively low ($500000\text{ cm}^2/\text{Vs}$ and lower) and relatively high ($900000\text{ cm}^2/\text{Vs}$ and higher) charge-carrier mobilities. © 2002 MAIK “Nauka/Interperiodica”.

PACS numbers: 72.40.+w; 73.43.-f

Studies of photoconductivity and cyclotron absorption of terahertz electromagnetic radiation in two-dimensional (2D) electron systems in the quantum Hall (QH) regime have attracted the attention of researchers since the time of discovery of the QH effect [1]. Two-dimensional electron systems effectively interact with terahertz radiation [2–17], because the characteristic scale of energy gaps between the Landau levels in the QH regime is about 10 meV. The unique feature of the terahertz spectroscopy consists in the absence of the interband generation of electron–hole pairs, so that the radiation absorption leads to a redistribution of electrons in energy without changing the total number of electrons in the 2D electron system. This provides a possibility for the most correct study of the electron excitation processes and the subsequent electron relaxation under the QH conditions. In this paper, we present the results of studying the terahertz photoconductivity kinetics in the QH regime.

Samples used in our experiments were made on the basis of GaAs/AlGaAs heterostructures characterized by the following mobilities $\mu_{4,2\text{K}}$ and densities n_s of 2D electrons: structure A with $\mu_{4,2\text{K}} = 1.9 \times 10^5\text{ cm}^2/\text{Vs}$ and $n_s = 3.11 \times 10^{11}\text{ cm}^{-2}$; structure B with $\mu_{4,2\text{K}} = 5 \times 10^5\text{ cm}^2/\text{Vs}$ and $n_s = 2 \times 10^{11}\text{ cm}^{-2}$; structure C with $\mu_{4,2\text{K}} = 9 \times 10^5\text{ cm}^2/\text{Vs}$ and $n_s = 2 \times 10^{11}\text{ cm}^{-2}$; and structure D with $\mu_{4,2\text{K}} = 16 \times 10^5\text{ cm}^2/\text{Vs}$ and $n_s = 3.57 \times 10^{11}\text{ cm}^{-2}$. The structures were used to fabricate the devices in the form of Hall bridges (270 μm wide and

2 mm long) and in the form of meanders (with a width of 100 μm and an effective length of 60 mm, so that the resulting area of the sample was $2 \times 3\text{ mm}$). The terahertz radiation source was a *p*-Ge pulsed cyclotron resonance laser (pulse duration was less than 1 μs) with a wavelength tuned by a magnetic field within 100–160 μm [18–21]. The measured signal was the voltage drop between the potential contacts induced by a terahertz radiation pulse in magnetic fields corresponding to filling factors near $\nu = 2$. Figure 1 shows the dependence of the photoresponse (PR) of a meander-shaped sample B on magnetic field for different positions of the *p*-Ge laser line. This dependence shows the presence of two PR mechanisms. In addition to the double PR peak that is associated with the bolometric response of the system and is “fixed” to the edges of the QH plateau, a single peak whose position depends on the photon energy of laser radiation is observed. The position of this peak varies linearly with magnetic field, in compliance with the value of the cyclotron mass $m_c = 0.067m_0$ (m_0 is the free electron mass); i.e., a cyclotron resonance peak is observed in the PR.

In the course of the experiments, it was found that samples with low and high mobilities exhibit not only different transport characteristics but also qualitatively different dynamics of the photoconductivity signal. The time dependences of the PR, which are typical of the samples made on the basis of structures A and B, are presented in Figs. 1 and 2a. We observed two PR components with different decay times. The initial rapidly decreasing (with the decay time $t = 2\text{--}3\text{ }\mu\text{s}$ for the Hall bridges and $6\text{--}8\text{ }\mu\text{s}$ for the meanders) part of PR changes sign upon reverting magnetic field. This result

¹ Permanent address: Institute of Physics of Microstructures, Russian Academy of Sciences, Nizhni Novgorod, 603950 Russia.

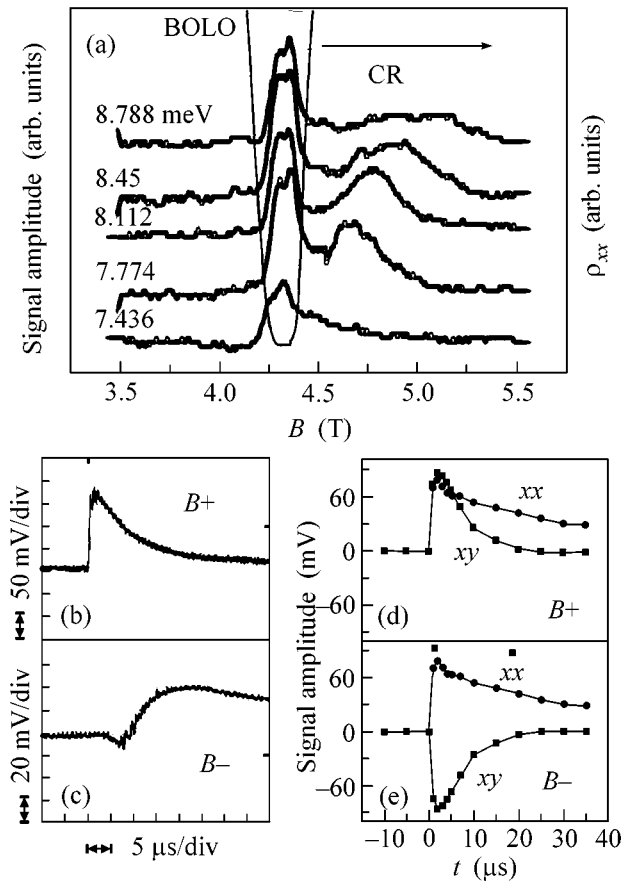


Fig. 1. (a) Magnetic-field dependence of the photoresponse of a meander-shaped sample (structure B) for different positions of the laser line 30 μs after the laser pulse. The maximal laser intensity J_{max} corresponds to a peak power of about 1 W, the bias current is $I_{\text{bias}} = 25 \mu\text{A}$ and $T = 4.2 \text{ K}$. For illustration, the plot also presents the dependence of the longitudinal resistance of the same sample on magnetic field in the absence of laser radiation. (b)–(e) Time dependences of the photoresponse of a meander-shaped sample (structure A): plots (b) and (c) show the dependences of the early photoresponse evolution for two opposite directions of magnetic field $B = 5.9 \text{ T}$ at $I_{\text{bias}} = 25 \mu\text{A}$ and for the photon energy of laser radiation equal to 10.92 meV; plots (d) and (e) present the results of numerical analysis and separation of the Hall (xy) and longitudinal (xx) photoresponse components from the data of plots (b) and (c).

is explained by the fact that, within the first few microseconds after the terahertz radiation pulse, the PR signal mainly results from the drift of photoexcited electrons along the Hall field of the sample; i.e., it is a current flowing in the sample in the transverse direction [20, 21]. It should be stressed that the PR component induced by the transverse current contributes to the voltage drop between the potential contacts. This contribution is associated with the conductivity of 2D electron gas in the QH regime. The equation relating the current density to the electric field has the form $E_x = \rho_{xx}j_x + \rho_{xy}j_y$, where ρ_{xx} and ρ_{xy} are the resistivity tensor components. From this equation, it follows that the

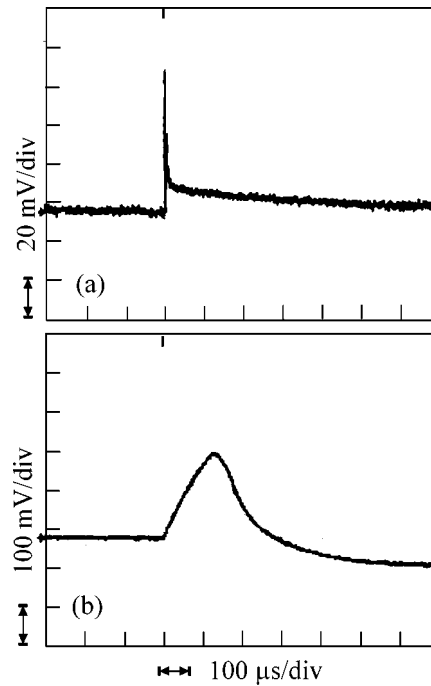


Fig. 2. (a) Time dependences of the cyclotron resonance photoresponse for meander-shaped samples with (a) $\mu_{4.2\text{K}} = 1.9 \times 10^5 \text{ cm}^2/\text{Vs}$ and $n_s = 3.11 \times 10^{11} \text{ cm}^{-2}$ (structure A) and (b) with $\mu_{4.2\text{K}} = 5 \times 10^5 \text{ cm}^2/\text{Vs}$ and $n_s = 2 \times 10^{11} \text{ cm}^{-2}$ (structure C) at $T = 4.2 \text{ K}$ and J_{max} . The values of magnetic field strength, bias current, and photon energy of laser radiation are as follows: (a) 6.17 T, 60 μA , and 10.68 meV, respectively; (b) 5.25 T, 25 μA , and 9.126 meV, respectively.

transverse current also makes a contribution to the longitudinal electric field.

In addition to this rapidly decreasing component, for samples A and B we observed longitudinal PR components which did not change their sign under the magnetic field reversal; these components are characterized by decay times of 280–350 μs .

In both meanders (structures A and B) and Hall bars, the longitudinal PR component also contains very slow components with decay times of tens or even hundreds of milliseconds. One can assume that they are associated with the heating of crystal lattice or to the elastic deformation of the structure because of the sound pulse that accompanies the pulse of terahertz radiation and propagates in liquid helium from the laser active element.

We did not observe any substantial difference in the time constants for the structures with relatively low mobilities (samples A and B with mobilities of 190000 and 500000 cm^2/Vs , respectively) in the case of both meander-shaped samples and Hall bars. At the same time, the signal intensity associated with the cyclotron resonance was higher in the samples with higher mobilities.

For the structures with high mobilities (C and D), we observed qualitatively different dynamics: unlike samples A and B, which exhibited dynamics similar to those shown in Fig. 2a, samples C and D produced a signal of the type shown in Fig. 2b. The signal was unstable and varied in shape from one laser pulse to the other. The samples operated not as linear devices but in the “switch” mode. An increase in the mobility was accompanied by a decrease in the QH breakdown current and a narrowing of the QH plateau. The explanation for such a behavior is known [22]: in samples with higher mobility, the dimensions of the localization regions become comparable with (or greater than) the sample width, because they can reach tens (or even hundreds) of microns. In such samples, the relaxation to the equilibrium state requires much longer time. Thus, the difference in the photoconductivity kinetics observed for samples with different mobilities can be attributed to the difference in the amplitude and correlation radius of the scattering potential and to the corresponding difference in the conduction mechanisms in the QH regime.

In closing, we note that our experiments have revealed the presence of two PR mechanisms: the bolometric and the cyclotron resonance mechanism. The effect observed by us is a result of the contributions made by the variations of both longitudinal and transverse conductivities under the terahertz radiation. The photoconductivity signal kinetics is qualitatively different for samples with low and high mobilities of charge carriers.

We are grateful to K. von Klitzing, R. Haug, R. Gerhardt, and U. Zeitler for encouraging us in this work and for useful discussions. We thank I.V. Kukushkin for helping us in improving our experimental setup. The work was supported by the German Scientific Community (DFG, the program “Quantum Hall Systems,” project no. Na235/10-1/2). The work of Yu.V. and S.S. was also supported by the Russian Foundation for Basic Research and by the programs “Low-Dimensional Quantum Structures” and “Physics of Solid-State Nanostructures.”

REFERENCES

1. K. von Klitzing, G. Dorda, and M. Pepper, *Phys. Rev. Lett.* **45**, 494 (1980).
2. J. C. Maan, Th. Englert, D. C. Tsui, and A. C. Gossard, *Appl. Phys. Lett.* **40**, 609 (1982).
3. D. Stein, G. Ebert, K. von Klitzing, *et al.*, *Surf. Sci.* **142**, 406 (1984); D. Stein, *Diplomarbeit* (Tech. Univ., Munchen, 1983).
4. R. E. Horstmann, E. J. van den Broek, J. Wolter, *et al.*, *Solid State Commun.* **50**, 753 (1984).
5. M. J. Chou, D. C. Tsui, and A. Y. Cho, in *Proceedings of 18th International Conference on Physics of Semiconductors* (World Sci., Stockholm, 1986), p. 437.
6. Yu. B. Vasilyev, S. D. Suchalkin, Yu. L. Ivanov, *et al.*, *JETP Lett.* **56**, 377 (1992); S. Suchalkin, Yu. Vasilyev, Yu. Ivanov, *et al.*, *Solid-State Electron.* **40**, 469 (1996).
7. R. Merz, F. Keilmann, R. J. Haug, *et al.*, *Phys. Rev. Lett.* **70**, 651 (1993).
8. R. J. F. van Haren, F. A. P. Blom, and J. H. Wolter, *Phys. Rev. Lett.* **74**, 1198 (1995).
9. A. Lorke, J. P. Kotthaus, J. H. English, *et al.*, *Phys. Rev. B* **53**, 1054 (1996).
10. K. Hirakawa, M. Endo, K. Yamanaka, *et al.*, in *Proceedings of 23rd International Conference on Physics of Semiconductors* (World Sci., Berlin, 1996), p. 2543.
11. K. Hirakawa, K. Yamanaka, Y. Kawaguchi, *et al.*, *Phys. Rev. B* **63**, 085320 (2001).
12. B. G. L. Jager, S. Wimmer, A. Lorke, *et al.*, *Phys. Rev. B* **63**, 045315 (2001).
13. Y. Kawano, Y. Hisanaga, H. Takenouchi, *et al.*, *J. Appl. Phys.* **89**, 4037 (2001).
14. I. V. Erofeeva, V. I. Gavrilenko, and S. Komiyama, *Nanotechnology* **12**, 453 (2001).
15. Y. Kawaguchi, K. Hirakawa, M. Saeki, *et al.*, *Appl. Phys. Lett.* **80**, 136 (2002).
16. Y. Kawaguchi, K. Hirakawa, and S. Komiyama, *Appl. Phys. Lett.* **80**, 3418 (2002).
17. R. J. Heron, R. A. Lewis, B. E. Kane, *et al.*, *Appl. Phys. Lett.* **75**, 3150 (1999).
18. Yu. L. Ivanov and Yu. B. Vasilyev, *Sov. Tech. Phys. Lett.* **9**, 264 (1983).
19. K. Unterrainer, C. Kremser, E. Gornik, *et al.*, *Solid-State Electron.* **32**, 1527 (1989).
20. N. G. Kalugin, G. Nachtwei, Yu. B. Vasilyev, *et al.*, *Appl. Phys. Lett.* **81**, 382 (2002).
21. N. G. Kalugin, Yu. B. Vasilyev, S. D. Suchalkin, *et al.*, *Phys. Rev. B* **66**, 085308 (2002).
22. S. Koch, R. J. Haug, K. von Klitzing, *et al.*, *Phys. Rev. B* **46**, 1596 (1992).

Translated by E. Golyamina

Modulation of the Resonant Rayleigh Light Scattering Spectrum of GaAs/AlGaAs Structures with Quantum Wells under Above-Barrier Illumination

N. N. Sibel'din, M. L. Skorikov, and V. A. Tsvetkov

Lebedev Physical Institute, Russian Academy of Sciences, Moscow, 119991 Russia

e-mail: sibel'din@mail.l.lebedev.ru

Received October 18, 2002

It is found that additional illumination by photons with energies above the band gap width in barrier layers leads to a strong (up to 40% in depth at the values of the illumination power used in this work) modulation of the light intensity elastically scattered upon resonant excitation of exciton states in quantum wells of GaAs/AlGaAs structures. Evidently, the effect observed is associated with the redistribution of oscillator strengths of exciton transitions due to the formation of three-particle exciton complexes (trions). These complexes arise through preferred capture of nonequilibrium like charge carriers (in our case, holes). © 2002 MAIK "Nauka/Interperiodica".

PACS numbers: 73.21.Fg; 78.35.+c; 78.67.De

Light scattering arises because of static or dynamic fluctuations of the refractive index of the medium. The scattered light intensity strongly increases when the frequency of the light propagating through the medium is close to the frequency of a certain optical transition in this medium (resonant scattering [1]). Resonant Rayleigh¹ scattering (RRS) upon excitations to heavy-hole exciton states in semiconductor structures with quantum wells (QW) was first observed by Hegarty *et al.* [2, 3] and was explained by the occurrence of lateral fluctuations of the QW width. These fluctuations lead to a spread in the energy position of exciton levels, that is, resonance frequency of exciton transitions. Resonant scattering may serve as a powerful method for studying effects associated with nonuniformities in the spatial distribution of the electron density of states of various types (localized and free excitons, impurity centers, etc.). Currently, this method is rather widely used for studying semiconductors and semiconductor-based nanostructures (see, e.g., [4, 5] and references therein).

External perturbations (magnetic or electric field, deformation of the sample, etc.) can significantly affect the electronic spectrum of a semiconductor or a semiconductor nanostructure and, respectively, affect RRS. Additional illumination of the sample by radiation with a wavelength differing from the scattered light wavelength is one of such perturbations. Much as this takes place in experiments on photorefectance and photoabsorption [6], illumination may lead to a change in internal electric fields, to occupation of electronic states, etc. and, thus, affect the spectrum and intensity of RRS.

¹ That is, elastic scattering by optical nonuniformities with linear sizes much smaller than the light wave length.

In the case of intrawell excitation of excitons in semiconductor structures, additional illumination by radiation with quantum energies above the band gap width in barrier layers can induce the formation or recharging of three-particle exciton complexes (trions) in QW, and the change in their concentration lead to the corresponding transformation of photoluminescence (PL) and PL excitation (PLE) spectra [7, 8]. It should be expected that the RRS spectra will also change under these conditions.

In this work, we report the detection of strong modulation of the RRS intensity upon excitation of heavy-hole excitons in shallow QW of GaAs/AlGaAs structures under additional above-barrier illumination under conditions when illumination leads to the formation of trions in QW. We believe that, the main contribution to the effect observed is associated with the occurrence of an additional channel of electron–phonon interaction upon illumination, namely, with the possibility of direct (resonant) excitation of trions. As a result, RRS arises at the trion transition frequency, and the oscillator strengths of transitions to free exciton states decrease. Hence, the intensity of light scattered at these transitions decreases as well.

The structure under study contained two tunnel-isolated GaAs QW 30 and 40 Å in width separated by an Al_{0.05}Ga_{0.95}As barrier 600 Å in width and confined on both sides by Al_{0.05}Ga_{0.95}As barrier layers 1000 Å thick. The band gap width in barrier layers E_{gb} was about 1.6 eV, and the depth of potential wells for electrons and holes was 45 and 30 meV, respectively. QW with such parameters must have one single-particle size-quantization level for particles of each sort, namely,

electrons, heavy holes, and light holes. However, in fact, their exciton spectrum is more complex than follows from this simple picture [9].

A titanium–sapphire laser tunable in the range 1.49–1.77 eV served as a source of exciting radiation. A He–Ne laser was used for additional above-barrier illumination of the sample. The energy of its quanta (1.96 eV) considerably exceeded E_{gb} . The beams of both lasers were overlapped with each other and focused on the sample surface into a spot about 3 mm in diameter. The maximum radiation intensity incident on the sample was about 1 W/cm² for the Ti–sapphire laser and 10⁻² W/cm² for the He–Ne laser. In most of the experiments, the Ti–sapphire laser power was chosen in such a way that the luminescence excited by both sources was of approximately the same intensity. The exciting or illuminating laser beam was modulated by a mechanical chopper with a frequency of 1 kHz. The secondary radiation (luminescence and scattered light) was collected from the excited sample surface (that is, in reflection geometry), analyzed by an MDR-2 monochromator (relative aperture 1 : 2.5, collimator focal length 400 mm, and grating with 600 lines per mm), and detected by a cooled photomultiplier. The photomultiplier signal was measured using a lock-in detection technique. During the measurements, the sample was in superfluid helium at a temperature of ≈ 2 K.

The specific features of radiative recombination in the structure under study were described previously in [8]. It was found that the recombination radiation spectrum of each QW in the structure excited by the radiation of a He–Ne laser consists of two lines: the high-energy component corresponds to exciton luminescence, and the low-energy component corresponds to trion luminescence. The luminescence spectrum of a narrow (30 Å in width) QW of the structure is shown in Fig. 1a. At the same time, trion lines were absent in the PL spectrum in the case of resonance excitation of free heavy-hole excitons in QW by Ti–sapphire laser radiation. A region of the PLE spectrum of a narrow QW corresponding to this exciton transition is also shown in Fig. 1a. These results demonstrate that the concentration of charge carriers (electrons or holes), which form trions upon binding to excitons, is sufficiently small in the absence of sample illumination. In the case of above-barrier excitation by He–Ne laser radiation, an excess of charge carriers of one sign or another (evidently, holes in our case) appears in the wells because of the difference in the capture efficiency of electrons and holes in QW. Thus, conditions for the formation of trions are created. In the case of simultaneous excitation of the sample by both lasers, the ratio between the intensities of the exciton and trion components of the luminescence spectrum is determined by the rates of kinetic processes (capture of charge carriers in QW, formation of excitons and trions, recombination processes) in nonequilibrium electron–hole system and

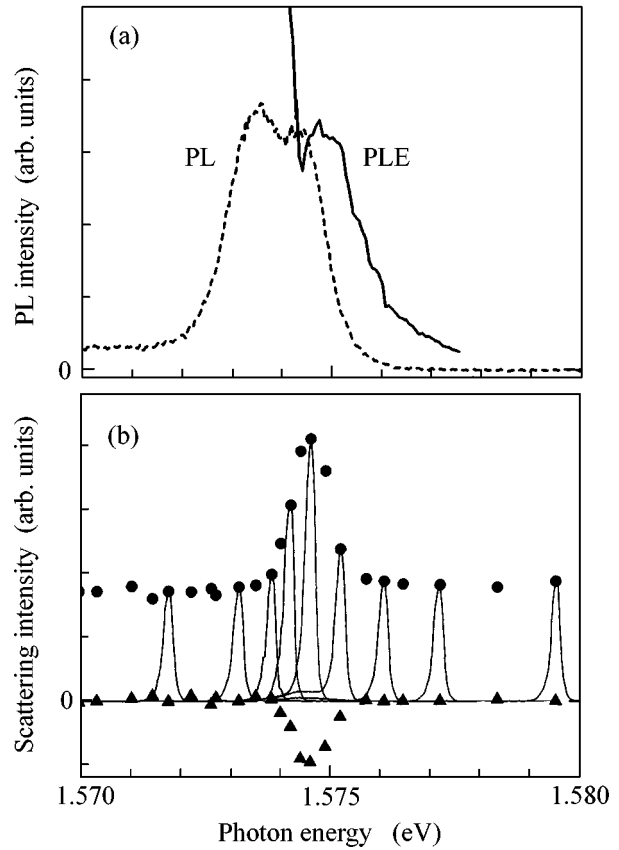


Fig. 1. (a) PL spectrum upon excitation by He–Ne laser radiation (dashed curve) and PLE spectrum in the region of transitions to heavy-hole exciton states (solid curve) of a narrow QW of the structure. (b) Intensity of resonant Rayleigh light scattering in the absence of illumination I_{off} (circles) and its change $\Delta I = I_{on} - I_{off}$ upon switching on illumination by He–Ne laser radiation (triangles) as functions of the exciting light photon energy $\hbar\omega_{exc}$; fine solid lines are secondary emission spectra for some values of $\hbar\omega_{exc}$.

depends on the density of excitation by each of these lasers [8].

Several secondary emission spectra of a narrow QW of the structure obtained upon excitation by Ti–sapphire laser radiation with different energies of light quanta are drawn in Fig. 1b by fine lines. The peak energy position of each spectral line corresponds to the excitation quantum energy $\hbar\omega_{exc}$, and its width is determined by the spectrometer spread function. That is, the contribution from the elastic scattering of the exciting light dominates in all spectra. At the values of $\hbar\omega_{exc}$ that fall in the band of resonance excitation of heavy-hole exciton photoluminescence (Fig. 1a), the secondary emission spectrum also contains a low-energy wing with an intensity considerably lower than the scattering line intensity. This is due to luminescence (at the given amplification, it is manifested substantially in the third and fourth curves at the right). The dependence of the scattered light intensity on $\hbar\omega_{exc}$ is shown by circles in

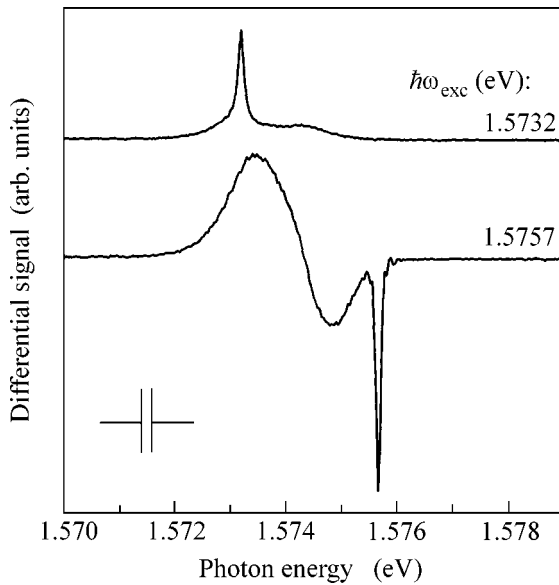


Fig. 2. Differential RRS and PL spectra for two values of the quantum energy of the exciting light.

Fig. 1b (lest the figure be overcharged, the spectra are not given for all values of $\hbar\omega_{\text{exc}}$). The resonance increase in scattering intensity is pronounced in the vicinity of the exciton transition energy. The small (less than 0.2 meV) Stokes shift of the RRS signal maximum with respect to the maximum of the PLE spectrum gives evidence of the high quality of the structure [10]. The light scattering intensity well apart from the resonance is virtually independent of the quantum energy and is determined by nonselective (residual) scattering from the sample surface and elements of the optical system.

When switching on the additional stationary illumination of the sample by He–Ne laser radiation, we observed a rather significant change in the scattered light intensity. The decrease in the scattered light intensity upon illumination at the maximum of the resonance curve was about 40% of the resonance amplitude at the excitation and illumination intensities used in this work. At the same time, the scattering intensity remains virtually unchanged outside the resonance region. The change in the scattered light intensity $\Delta I = I_{\text{on}} - I_{\text{off}}$ under the action of illumination is shown in Fig. 1b by triangles (I_{off} and I_{on} are the intensities, respectively, without and with illumination). It is evident that the dependence of ΔI on $\hbar\omega_{\text{exc}}$ approximately repeats the dependence of I_{off} less the intensity of the background nonresonant scattering.

The light-scattering experiments described above were carried out with the use of modulated exciting radiation of a Ti–sapphire laser and stationary He–Ne illumination. In order to extract weak difference signals more reliably and accurately, that is, for the direct detection of the changes in the scattered light intensity

ΔI arising upon illumination, we used a differential technique that is commonly used in modulation spectroscopy when the illuminating rather than exciting laser beam is modulated. In this case, changes in intensity due to additional illumination will also be observed in luminescence spectra.

Figure 2 displays differential secondary emission spectra of a narrow QW measured at two values of the exciting light photon energy $\hbar\omega_{\text{exc}} = 1.5757$ and 1.5732 eV. The former value is close to the energy position of the free exciton peak in the PLE spectrum, and the second one, to the maximum of the trion PL line (see Fig. 1a). It is evident in Fig. 2 that, in the case of excitation to the free exciton state (lower spectrum), the additional illumination leads to a decrease in the RRS light intensity (narrow peak) accompanied by a drop in the free exciton luminescence line intensity (both signals, RRS and PL, are negative), whereas the trion component of the PL spectrum increases (signal is positive). It was already noted that above-barrier illumination gives rise to an excess of nonequilibrium holes in QW. Excitons created upon resonance excitation are bound with these holes, forming positively charged trions. Therefore, the intensity of exciton luminescence decreases, and that of trion luminescence increases [8].

When excitation is performed in the vicinity of the peak of the trion PL line (upper curve in Fig. 2), a spike related to RRS light as well as lines of exciton and trion luminescence are observed in the differential spectrum, all the signals being positive. Note that the main contribution to the luminescence spectrum arises from direct excitation of the sample by He–Ne illumination. As mentioned above, the equilibrium concentration of charge carriers in QW is too small in order for intrawell excitation by Ti–sapphire laser radiation could result in the formation of a notable amount of trions. On the other hand, in the case of excitation to the states with an energy lower than the free exciton energy (for example, to localized exciton states), the line of free exciton luminescence must have low intensity at low temperatures, because it can appear only as a result of thermal depletion of lower lying states (exciton delocalization).

Thus, the use of the differential technique allows us to find that the scattered light intensity can both decrease and increase upon illumination, depending on $\hbar\omega_{\text{exc}}$.

Figure 3 demonstrates a series of differential spectra obtained at various values of the quantum energy of the exciting Ti–sapphire laser. As the excitation quantum energy decreases, the amplitude of the negative signal (corresponding to the decrease in the intensity of RRS light upon additional illumination) first increases, then starts to drop and changes its sign, when the quantum energy $\hbar\omega_{\text{exc}}$ is in the energy range in which the trion luminescence line is located. The shape of the differential PL spectra at two values of $\hbar\omega_{\text{exc}}$ was described in sufficient detail and explained in the two preceding paragraphs. The results presented in Fig. 3 allow one to

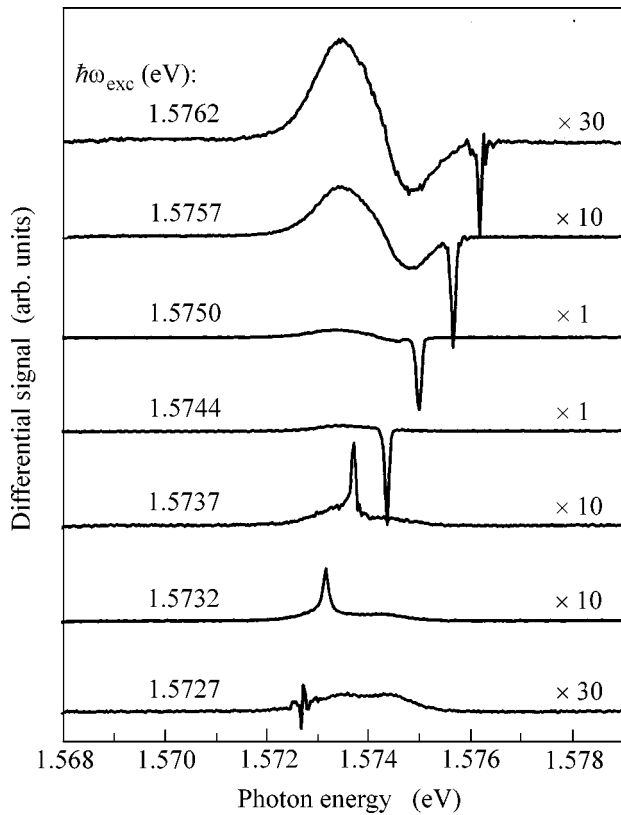


Fig. 3. Dependence of differential secondary emission spectra of a narrow QW of the structure on the quantum energy of the exciting light.

follow how these spectra are transformed as $\hbar\omega_{\text{exc}}$ is changed. The spectral dependence of the amplitude of the differential RRS signal (proportional to the change in the scattered light intensity upon illumination) obtained from the data similar to those given in Fig. 3 is shown in Fig. 4. It is evident that the maximum value of the negative RRS signal more than an order of magnitude exceeds the maximum value of the positive signal.

The results presented here relate to a narrow QW. The results for a wide (40 Å in width) QW of the structure are in a qualitative agreement with the above results and are not presented here to save room. Completing the description of experimental data, we note that the amplitude of the differential RRS signal is directly proportional to the excitation intensity, whereas its dependence on the illumination intensity exhibits more complicated nonmonotonic behavior and needs presently a more careful investigation.

Let us discuss the possible qualitative explanation of the effect observed. The scattered light intensity is characterized by the extinction coefficient h , which is defined as the ratio of the total intensity of light scattered in a unit volume along all the directions to the flux density of the incident light. It is proportional to the

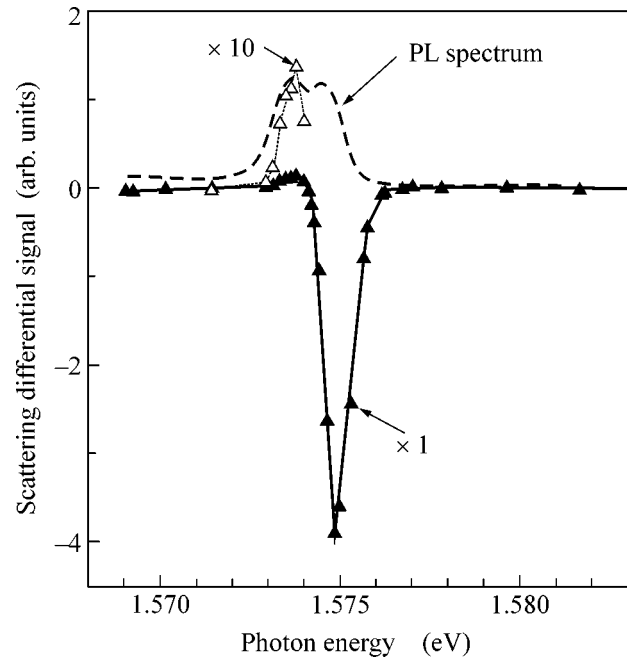


Fig. 4. Dependence of the differential RRS signal amplitude on the quantum energy of the exciting light (black triangles). A portion of curve on a tenfold enlarged scale is shown by light triangles. For comparison, dashed curve shows the PL spectrum of a narrow QW upon excitation of the structure by He-Ne laser radiation.

mean squared fluctuation of the permittivity $\langle(\delta\varepsilon)^2\rangle_V$ in the volume V [11]

$$h = (\omega^4 V / 6\pi c^4) \langle(\delta\varepsilon)^2\rangle_V. \quad (1)$$

The contribution to the permittivity of the crystal from each of the electronic transitions is proportional to its oscillator strength. If fluctuations of ε are due to the fluctuations of exciton transition frequencies [2], then, in the vicinity of the exciton resonance one has $(\delta\varepsilon)^2 \propto f^2$, where f is the oscillator strength of this transition.

Let us denote the oscillator strength of the exciton transition in the absence of illumination (that is, in the absence of charge carriers in QW) by f_0 ; in this case, the oscillator strength of the trion transition equals zero. When illumination is switched on, charge carriers appear in QW. As a result, the possibility of direct resonant excitation of trions arises. Therefore, the trion transition acquires some oscillator strength f_{tr} . By virtue of the sum rule, the oscillator strength of the exciton transition decreases, because an additional channel of electron-photon interaction opens. Let us denote the change in the oscillator strength of the exciton transition by $\Delta f_{\text{ex}} = f_{\text{ex}} - f_0$, where f_{ex} is the exciton oscillator strength in the presence of illumination. As a consequence, resonant Rayleigh light scattering arises in the vicinity of the transition to trion states upon illumination. Its intensity is proportional to $h_{\text{tr}} \propto f_{\text{tr}}^2$, and the RRS intensity in the vicinity of the exciton transition

changes by the value proportional to $\Delta h_{\text{ex}} \propto f_{\text{ex}}^2 - f_0^2 \cong 2f_0\Delta f_{\text{ex}}$ (at small Δf_{ex}). The relative change in the scattered light intensity in the vicinity of the exciton resonance $\Delta h_{\text{ex}}/h_0 \cong 2\Delta f_{\text{ex}}/f_0$, where h_0 is the extinction coefficient in the exciton resonance region in the absence of illumination.

From experimental data at the maximum levels of excitation and illumination (Fig. 1b), we obtain $\Delta h_{\text{ex}}/h_0 \approx -0.4$, and an estimation of the change in the oscillator strength of the exciton transition gives $\Delta f_{\text{ex}} \approx -0.2f_0$. Considering that the resonance frequencies and the damping coefficient for exciton and trion transitions are almost similar, we obtain from the above relationships $\Delta h_{\text{ex}}/h_{\text{tr}} \cong 2f_0\Delta f_{\text{ex}}/f_{\text{tr}}^2$. From the differential RRS spectrum (Fig. 4), we obtain $\Delta h_{\text{ex}}/h_{\text{tr}} \approx -28$. From here, with the use of the above value of Δf_{ex} , the estimation of f_{tr} gives $f_{\text{tr}} \approx 0.12f_0$.

Thus, f_{tr} comprises approximately 60% of Δf_{ex} ; that is, most of the oscillator strength of the exciton transition is transferred to trions. Evidently, this means that, under conditions when illumination can result in the formation of trions, the effect of redistribution of oscillator strengths of transitions in the exciton region of the spectrum considered above makes the main contribution to the strong photomodulation of the intensity of resonant Rayleigh light scattering. However, in fact, the real situation is more complicated. Thus, excess charge carriers that appear upon illumination do not fill QW uniformly and are accumulated in the regions with larger local well width. This means that the resonant photogeneration of trions can proceed only in these regions. Therefore, besides energy fluctuations of exciton transitions, fluctuations arise in the oscillator strengths that are spatially correlated with the former ones. This must also affect the scattering intensity. In addition, the nonuniformity of the charge carrier distribution in the well plane give rise to electric fields, which can change the local values of ϵ . Other effects that can lead to a change in the RRS intensity are also possible.

Thus, strong photomodulation of the resonant Rayleigh light scattering has been observed experimentally in this work in the region of exciton transitions in quantum wells under illumination of the structure by radiation with quantum energies that exceed the band-gap width in barrier layers. The effect observed has been explained by redistribution of oscillator strengths of

exciton and trion transitions due to accumulation of excess holes in wells and the possibility of direct (resonant) photogeneration of trions arising in this case. Note that an analogous effect should also be observed in the resonant light reflection spectra.

We are deeply grateful to L. V. Keldysh for a fruitful discussion, B. Etienne for presenting structures, and N. V. Zamkovets and B. D. Kopylovskii for technical help. This work was supported by the Russian Foundation for Basic Research (project no. 02-02-17033), Ministry of Industry, Science, and Technology of the Russian Federation (Program "Physics of Solid-State Nanostructures"), Program of Support for Scientific Schools (project no. 00-15-96568), and Program of the Russian Academy of Sciences "Low-Dimensional Quantum Structures."

REFERENCES

1. R. Loudon, *The Quantum Theory of Light* (Clarendon Press, Oxford, 1973; Mir, Moscow, 1976), Chap. 11.
2. J. Hegarty, M. D. Sturge, C. Weisbuch, *et al.*, *Phys. Rev. Lett.* **49**, 930 (1982).
3. J. Hegarty, L. Goldner, and M. D. Sturge, *Phys. Rev. B* **30**, 7346 (1984).
4. V. A. Kosobukin and A. V. Sel'kin, *Fiz. Tverd. Tela* (St. Petersburg) **42**, 1863 (2000) [*Phys. Solid State* **42**, 1914 (2000)].
5. V. Savona, E. Runge, and R. Zimmermann, *Phys. Rev. B* **62**, R4805 (2000).
6. J. I. Pankove, *Optical Processes in Semiconductors* (Prentice-Hall, Englewood Cliffs, N.J., 1971; Mir, Moscow, 1973).
7. O. V. Volkov, V. E. Zhitomirskii, I. V. Kukushkin, *et al.*, *Pis'ma Zh. Éksp. Teor. Fiz.* **67**, 707 (1998) [*JETP Lett.* **67**, 744 (1998)].
8. N. N. Sibeldin, M. L. Skorikov, and V. A. Tsvetkov, *Nanotechnology* **12**, 591 (2001).
9. E. A. Mulyarov, N. N. Sibel'din, M. L. Skorikov, *et al.*, *Pis'ma Zh. Éksp. Teor. Fiz.* **70**, 613 (1999) [*JETP Lett.* **70**, 621 (1999)].
10. V. I. Belitsky, A. Cantarero, S. T. Pavlov, *et al.*, *Phys. Rev. B* **52**, 16665 (1995).
11. L. D. Landau and E. M. Lifshits, *Electrodynamics of Continuous Media*, 2nd ed. (Nauka, Moscow, 1982; Pergamon, New York, 1984), Chap. 15.

Translated by A. Bagatur'yants

Ultrahigh-Frequency NMR of Tm^{3+} Ions in Single Crystals of Thulium Ethylsulfate in High Magnetic Fields

D. I. Abubakirov¹, V. V. Naletov¹, M. S. Tagirov¹, D. A. Tayurskii^{1,2,*}, and A. N. Yudin¹

¹ Department of Physics, Kazan State University, ul. Lenina 18, Kazan, 420008 Tatarstan, Russia

² Physics Department, Faculty of Science, Kanazawa University, 920-1192 Kanazawa, Japan

* e-mail: dtayursk@mi.ru

Received October 21, 2002

Resonant transitions predicted earlier between low-lying electron–nuclear sublevels of the Tm^{3+} ground state were observed at frequencies up to 700 MHz in a dielectric Van Vleck paramagnet—thulium ethylsulfate single crystal. It is shown that, due to the distortion of the 4f-electron shell of a rare-earth ion in an applied magnetic field, the parameters of electron–nuclear interaction become field-dependent. © 2002 MAIK “Nauka/Interperiodica”.

PACS numbers: 75.10.Dg; 76.30.Kg; 76.60.-k

1. Van Vleck (polarization) paramagnetism is most often observed in crystals containing non-Kramers rare-earth (RE) ions, i.e., RE ions with an even number of electrons in the unfilled 4f shells. The crystal electric field removes degeneracy of the ground $2S+1L_J$ multiplet of these ions to generate Stark splitting on the order of 10–100 cm^{-1} . In this case, the ground electronic state is a singlet or a nonmagnetic doublet, so that all magnetic properties of Van Vleck paramagnets are caused by the Zeeman splitting, which, as a rule, can be calculated using second-order perturbation theory [1, 2]. However, in rather strong magnetic fields ($H > 20$ kOe), conditions for the applicability of the perturbation theory are broken, and a number of new physical effects arise [3]. Among them, field-induced structural phase transitions in the dielectric VV paramagnets TmPO_4 [4] and LiTmF_4 [5] and the appearance of coupled 4f-electron–phonon excitations in thulium ethylsulfate crystals $\text{Tm}(\text{C}_2\text{H}_5\text{SO}_4)_2 \cdot 9\text{H}_2\text{O}$ (TmES) [6] are noteworthy. Strong magnetic fields also give rise to the coupled 4f-electron–nuclear states in dielectric VV paramagnets [3, 7]. It should be noted that the transition frequencies between the electron–nuclear sublevels of the ground singlet in TmES crystals fall, practically, within the EPR X-band, whereas the transition probabilities are induced by the matrix elements of nuclear spin operators. In this connection, one can speak about “ultrahigh-frequency” NMR in a strong magnetic field, contrary to the enhanced NMR at moderate fields [2]. It is the purpose of this work to observe and investigate ultrahigh-frequency Tm^{3+} NMR in a TmES single crystal in magnetic fields up to 3 T.

2. Theoretical studies of the effect of strong magnetic fields on the properties of Tm^{3+} ion in TmES single crystals [3] amount to the diagonalization of the

Hamiltonian of an isolated RE ion (in doing so, the spin–spin interaction between the ions is, naturally, ignored, because this is a good approximation for ethylsulfates, where the separations between the RE ions are about 7 Å)

$$\mathcal{H} = \mathcal{H}_{cr} + \mathcal{H}_{eZ} + \mathcal{H}_{nZ} + \mathcal{H}_{hf}, \quad (1)$$

where the Hamiltonian of crystal electric field in the common notation is written as [8]

$$\mathcal{H}_{cr} = \alpha B_{20} O_2^0 + \beta B_{40} O_4^0 + \gamma (B_{60} O_6^0 + B_{66} O_6^6). \quad (2)$$

The Zeeman interaction of the 4f shell, the nuclear Zeeman interaction, and the hyperfine interaction (with a constant A_{hf}) have the usual form

$$\begin{aligned} \mathcal{H}_{eZ} &= g_I \mu_B \mathbf{HJ}, & \mathcal{H}_{nZ} &= -\gamma_I \hbar \mathbf{HI}, \\ \mathcal{H}_{hf} &= A_{hf} \mathbf{JI}. \end{aligned} \quad (3)$$

The wave functions of electron–nuclear states, the transition frequencies, and the magnetic moment of the Tm^{3+} ion were calculated as functions of the magnitude and direction of an applied magnetic field. Further development of the theory required experimental verification of these dependences. First of all, it was necessary to observe the transitions between the ground-state electron–nuclear sublevels.

3. To measure the ^{169}Tm NMR spectra of a TmES single crystal in the frequency range from 18 to 700 MHz at a temperature of 4.2 K, a stationary bridge-type laboratory-assembled spectrometer with a matched resonant circuit was used. The static magnetic field and the perpendicular rf magnetic field were oriented in the plane perpendicular to the crystallographic axis c . To eliminate the effect of the demagnetizing field, the sample was shaped like a sphere of diameter 4

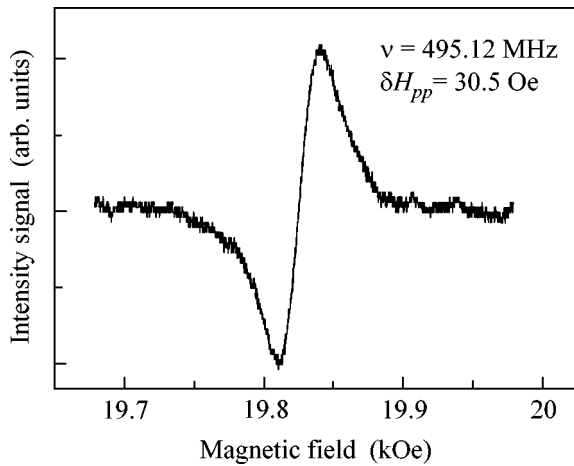


Fig. 1. Derivative of the ^{169}Tm NMR absorption signal in TmES. The frequency of applied rf magnetic field and the peak-to-peak width are indicated. Magnetic field is oriented perpendicular to the crystal symmetry axis c ; temperature is 4.2 K.

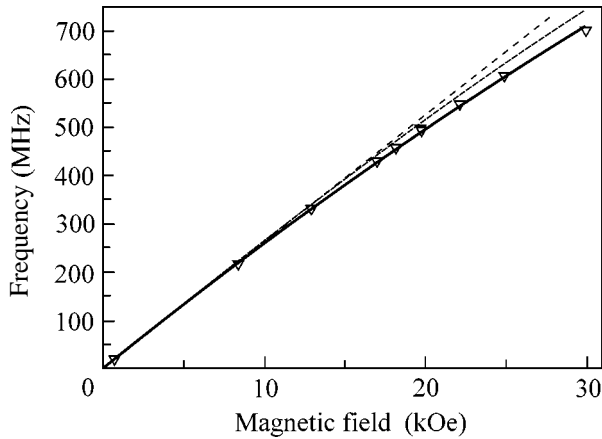


Fig. 2. Field dependences of the transition frequencies between the Tm^{3+} ground-state electron–nuclear sublevels in TmES at liquid helium temperature: ∇ are the experimental points; dotted line is for the results of the perturbation theory of boosted NMR [2]; dot-and-dash line is for the refined data given in [3, 7] for strong magnetic fields without taking into account a change in the hyperfine interaction parameters; and solid line is for the results of the theoretical calculations in this work (for details, see text).

mm. The transition frequency was determined from the absorption signal minimum upon scanning an amplitude-modulated magnetic field. The observed spectrum width monotonically increased with increasing static field and reached approximately 50 Oe at 30 Oe. The ratio of magnetic field to the solenoid current was calibrated against the EPR signal of a DPPH sample placed in the immediate vicinity of the sample under study.

The ^{169}Tm NMR signal in TmES at a frequency of 495 MHz is shown in Fig. 1. The measured field depen-

dence of the transition frequencies between the Tm^{3+} ground-state electron–nuclear sublevels in the TmES single crystal at liquid helium temperature is shown in Fig. 2 (points). Note that the observed dependence does not coincide with the one calculated in [3, 7] (Fig. 2, dot-and-dash line), where, for a more clear presentation of the changes induced by strong magnetic fields in the properties of electron–nuclear spin systems of dielectric VV paramagnets, the changes in the hyperfine field at the nucleus because of the electron-shell distortion and electron-density redistribution were ignored. Thus, we arrive at the conclusion that magnetic fields higher than 2 T distort noticeably the unfilled $4f$ shell of the RE ion, and one should not ignore the corresponding changes in a hyperfine magnetic field at nucleus in the calculations.

4. The standard scheme for analyzing the hyperfine interaction effects for the RE elements (the quadrupole effects are disregarded because the nuclear spin of ^{169}Tm is $I = 1/2$) is as follows (see, e.g., [8]). A magnetic field produced by $4f$ electrons with orbital angular momenta \mathbf{l}_i and spins \mathbf{s}_i

$$\begin{aligned} \mathbf{H}_{4f} &= -2\mu_B \sum_{i \in 4f} \{r_i^{-3} [\mathbf{l}_i - \mathbf{s}_i + 3\mathbf{r}_i(\mathbf{r}_i \mathbf{s}_i)/r_i^2]\} \\ &= -2\mu_B \langle r_i^{-3} \rangle \mathbf{N} \end{aligned} \quad (4)$$

within the ground $^{2S+1}L_J$ multiplet, where the total angular momentum is a good quantum number, can be represented in the form

$$\mathbf{H}_{4f} = -2\mu_B \langle r_i^{-3} \rangle \langle J \| N \| J \rangle \mathbf{J}, \quad (5)$$

where the reduced matrix elements $\langle J \| N \| J \rangle$ can easily be tabulated for different electronic $4f^n$ configurations [8]. As a result, the Hamiltonian of hyperfine interaction can be written as

$$\mathcal{H}_{hf} = 2\mu_B \gamma_I \hbar \langle r_i^{-3} \rangle (\mathbf{N} \mathbf{I}) = A_{hf} (\mathbf{J} \mathbf{I}). \quad (6)$$

The crystal electric field reduces rotational symmetry and distorts electronic shells of the RE ion in crystal, as compared to the free atom. As a result, the magnetic hyperfine interaction is affected [11], and the hyperfine constant A_{hf} becomes anisotropic, according to the symmetry of local environment of the RE ion. For this reason, Eq. (6) is replaced by the expression

$$\mathcal{H}_{hf} = (\mathbf{J} \tilde{\mathbf{A}} \mathbf{I}). \quad (7)$$

For RE ethylsulfates with a magnetic ground state, the principal values of hyperfine interaction tensor $\tilde{\mathbf{A}}$, as obtained from the experimentally measured hyperfine structure of EPR line, may differ from each other more than tenfold [8]. For the VV ions, i.e., ions with a non-magnetic ground state (e.g., the Tm^{3+} ion in TmES), paramagnetic resonance is unobservable, so that the principal values of hyperfine interaction tensor can be estimated only in an indirect way. Namely, one can

measure the so-called paramagnetic shift [2] by enhanced NMR at moderate fields. This shift is anisotropic and its value depends on both the hyperfine interaction magnitude and the degree of Stark wave-function mixing due to the electronic Zeeman interaction. Thereafter, one can perform numerical calculations using the explicit form of RE wave functions in crystal field. The estimates, made by us using the data of works [9] gave the following principal values of hyperfine interaction tensor for Tm^{3+} in axially symmetric crystal field in TmES [10]: $A_{\parallel} \approx -241$ MHz and $A_{\perp} \approx -388$ MHz (the estimate of A_{hf} made for a free trivalent Tm^{3+} ion from the Tm and Tm^{2+} measurements gave -393.5 MHz [8]). Note that the perturbative theory developed for enhanced NMR at moderate fields [2] predicts that the tensor components of paramagnetic shift are field-independent, as shown in Fig. 2 by the dotted line. One can see that, at strong magnetic fields, all experimental points lie systematically below this straight line. This poses the problem of analyzing the effect of strong magnetic fields on the electron–nuclear interaction in VV paramagnets.

5. A sufficiently strong magnetic field, for which the Zeeman energy of the RE ion is comparable to the Stark splitting energies of its ground multiplet, further reduces the symmetry of the local environment. Switching on such a magnetic field can be regarded as the inclusion of a low-symmetry term in the crystal-field Hamiltonian, with the magnitude of this term depending on the magnetic field strength. It then becomes clear that the hyperfine interaction should change in a sufficiently high magnetic field. This is primarily due to the fact that the angular dependence of $4f$ -electron density changes. Indeed, the radial distortions of the crystal-field parameters [B_2^0 and B_4^0 in Eq. (2)], which are equal, by the order of magnitude, to tens and hundreds of cm^{-1} , change the mean value $\langle r_i^{-3} \rangle$ by no more than one percent [11]. The magnetic fields in the range considered correspond to the Zeeman energies on the order of a few cm^{-1} .

To illustrate these arguments, we calculated the Tm^{3+} ground-state $4f$ wave functions in a TmES crystal exposed to different magnetic fields. Figure 3 depicts the angular dependences of the Tm^{3+} $4f$ -electron density for the TmES crystals placed in an external magnetic field of 5 T aligned with the x axis in the crystal symmetry plane. One can clearly see that symmetry breaks in the crystallographic plane between the x and y directions. Naturally, the electron-density redistribution should affect the direction and magnitude of the hyperfine magnetic field \mathbf{H}_{hf} at the nucleus. In addition, it is conceivable that the appearance of electron-density anisotropy in the xy plane perpendicular to the crystallographic axis c induces rotation of the nearest surroundings of the VV ion and, as a result, violates the equivalency of two Tm^{3+} ions in a unit cell of the TmES

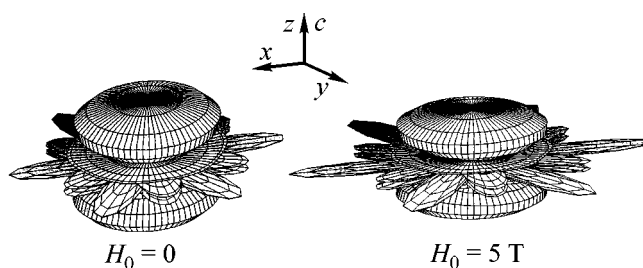


Fig. 3. Angular dependences of the $4f$ -electron density in the crystal electric field of TmES in the absence of magnetic field and in a magnetic field of 5 T oriented in the crystal symmetry plane.

crystal, as it can be seen from the spectra of bound $4f$ -electron–phonon states in TmES [3, 6].

Thus, the transition frequencies between the ground-state electron–nuclear sublevels of a VV ion in strong magnetic fields should be calculated self-consistently with allowance for the magnetic-field-induced distortions in the $4f$ shell [10]. The results of such calculations are presented in Fig. 2 by the solid line. Note also that, inasmuch as the field-induced magnetic moment of the $4f$ -electron shell depends, in principle, on temperature and, simultaneously, determines the hyperfine field at nuclei, the transition frequencies between the ground-state electron–nuclear sublevels can also show temperature dependence [10]. However, the experimental observation of this dependence necessitates substantial modification of the experimental setup.

6. In conclusion, we sum up the main results of this work. A specially designed experimental system has been used to observe the ultrahigh-frequency ^{169}Tm NMR signal in a single crystal of a dielectric VV paramagnet (thulium ethylsulfate) in the frequency range from 18 to 700 MHz in magnetic fields up to 3 T at helium temperature. The resonance signal was observed for the transitions between the Tm^{3+} ground-state electron–nuclear sublevels. The observed field dependence of the transition frequencies is evidence that the applied magnetic field affects the hyperfine interaction parameters. The theoretical method suggested for calculating these effects agrees satisfactorily with the experiment.

We are grateful to A.V. Egorov (Kazan State University) for assistance in experiment preparation, to Prof. M.M. Zaripov (Kazan State University) for the attention to the work, and to Prof. H. Suzuki (Kanazawa University, Japan) for the discussion of results. This work was supported by the Scientific and Educational CRDF center (REC-007) and the Nederlandse Organisatie voor Wetenschappelijk Onderzoek (NWO).

REFERENCES

1. J. H. Van Vleck and A. Frank, Phys. Rev. **34**, 1494 (1929).

2. L. K. Aminov and M. A. Teplov, *Usp. Fiz. Nauk* **147**, 49 (1985) [*Sov. Phys. Usp.* **28**, 762 (1985)]; L. K. Aminov and M. A. Teplov, *Sov. Sci. Rev., Sect. A* **14**, 1 (1990).
3. M. S. Tagirov and D. A. Tayurskiĭ, *Fiz. Nizk. Temp.* **28**, 211 (2002).
4. B. G. Vekhter, A. Z. Kazeĭ, M. D. Kaplan, *et al.*, *Pis'ma Zh. Éksp. Teor. Fiz.* **54**, 575 (1991) [*JETP Lett.* **54**, 578 (1991)].
5. A. V. Klochkov, V. V. Naletov, I. R. Mukhamedshin, *et al.*, *Pis'ma Zh. Éksp. Teor. Fiz.* **66**, 247 (1997) [*JETP Lett.* **66**, 266 (1997)].
6. D. A. Tayurskiĭ and M. S. Tagirov, *Pis'ma Zh. Éksp. Teor. Fiz.* **67**, 983 (1998) [*JETP Lett.* **67**, 1040 (1998)].
7. D. A. Tayurskii, M. S. Tagirov, and H. Suzuki, *Physica B (Amsterdam)* **284–288**, 1686 (2000).
8. A. Abragam and B. Bleaney, *Electron Paramagnetic Resonance of Transition Ions* (Clarendon Press, Oxford, 1970; Mir, Moscow, 1972 and 1973), Vols. 1 and 2.
9. R. Yu. Abdulsabirov, I. S. Konov, S. L. Korableva, *et al.*, *Zh. Éksp. Teor. Fiz.* **76**, 1023 (1979) [*Sov. Phys. JETP* **49**, 517 (1979)]; B. Bleaney, *Proc. R. Soc. London, Ser. A* **370**, 313 (1980).
10. D. A. Tayurskii and H. Suzuki, *J. Phys.: Condens. Matter* (in press).
11. R. E. Watson and A. J. Freeman, *Phys. Rev.* **133**, A1571 (1964).

Translated by V. Sakun

Polariton Dispersion of Periodic Quantum Well Structures¹

A. V. Mintsev¹, L. V. Butov^{1,2}, C. Ell³, S. Mosor³, G. Khitrova³, and H. M. Gibbs³

¹ Institute of Solid State Physics, Russian Academy of Sciences, Chernogolovka, Moscow region, 142432 Russia

² Materials Sciences Division, E. O. Lawrence Berkeley National Laboratory, 94720 Berkeley, California, USA

³ Optical Sciences Center, University of Arizona, 85721 Tucson, Arizona, USA

Received October 24, 2002

We studied the polariton dispersion relations of a periodic quantum-well structure with a period in the vicinity of half the exciton resonance wavelength, i.e., the Bragg structure. We classified polariton modes using an approximation of a large number of quantum wells. The polariton effective masses are found to be very small and equal to 10^{-3} – 10^{-4} of the free-electron mass. © 2002 MAIK “Nauka/Interperiodica”.

PACS numbers: 73.21.Fg; 71.36.+c; 73.20.Mf

Semiconductor structures allow engineering of the light–matter interaction. The band structure and dispersion relation of the coupled mode of exciton and photon, called a polariton, can be controlled by the structure design, thereby opening great opportunities for fundamental studies of exciton and photon physics, as well as for device applications. Recently, considerable attention has been devoted to the study of photon–matter interaction in semiconductor microcavities (MCs) [1] and photonic band-gap materials [2], i.e., structures characterized by light-wavelength size. One of the advantages of polariton-dispersion engineering is the possibility to construct a bosonic quasiparticle with extremely small effective mass m . In particular, due to the small density of states in such a system, a statistically degenerate gas of polaritons may arise even at high temperatures and small densities (the temperature at which a quasi-2D gas of noninteracting bosonic quasiparticles becomes statistically degenerate is $T_0 = \pi\hbar^2 n / 2mk_B$ [3]).

In this paper, we consider the system of polaritons in a periodic quantum-well (PQW) structure with a period close to half the exciton resonance wavelength, i.e., in a Bragg structure. In PQW structures, due to the total confinement of excitons in QWs, the propagation of polaritons through the PQW is possible only because of the electromagnetic transfer of excitation through the barrier layers; in this sense, they are Wannier–Mott excitons for in-plane motion and Frenkel excitons for motion in the growth direction [4]. Before there were any experiments, several unique properties of polaritons in PQW structures had been predicted [4–9]. Ivchenko *et al.* [8] made two related and significant predictions. First, in an infinite Bragg structure with $d = \lambda/2$, the normal light wave is a standing wave characterized by two wave vectors $Q = \pm\pi/d$ with a field $E(z) \propto \sin(\pi z/d)$ with nodes at every QW position. This wave

does not couple to excitons, because the optical transition matrix element $\propto \int dz E(z)\Psi(z)$ is minimal and, therefore, Bragg PQW structures with a large number of QWs poorly emit and absorb resonant light in the normal direction [8]. Second, although it is a poor emitter, the Bragg structure is an excellent reflector: due to constructive interference between the light waves reflected by various QWs, the reflectivity of the Bragg structure is dramatically enhanced; in fact, in reflectivity or transmission, a set of N QWs with $d = \lambda/2$ is equivalent to a single QW (SQW) with a radiative coupling coefficient N amplified times over the value for an SQW [8].

The theoretical predictions initiated intense experimental studies. A strong amplification of the reflectance in Bragg PQW structures was observed in [10]. The enhancement of the signal decay rate in the Bragg structure was observed in the degenerate four-wave-mixing experiments in reflection geometry [11]. Recently, almost 100% reflectivity and the onset of a photonic band gap were observed in a Bragg PQW sample with $N = 100$ QWs [12]. These experiments confirmed that the constructive interference between the light waves reflected by various QWs can be treated as a huge ($\propto N$) enhancement of the radiative coupling coefficient [8]. Further resonant excitation studies revealed that the radiative coupling effects dominate not only the transmission, reflection, and absorption spectra but also the resonance Rayleigh scattering [13, 14].

In this paper, we study polariton-dispersion relations of high-quality Bragg and nearly Bragg PQW structures with $d \approx \lambda/2$. In our experiments, e–h pairs are generated by continuum absorption and lose energy by incoherent processes, populating low-energy carrier and polariton states. As shown in [12], under these conditions the PL spectra of a PQW structure cannot be explained by the radiatively uncoupled incoherent emission of 100 individual QWs but are dominated by

¹ This article was submitted by the authors in English.

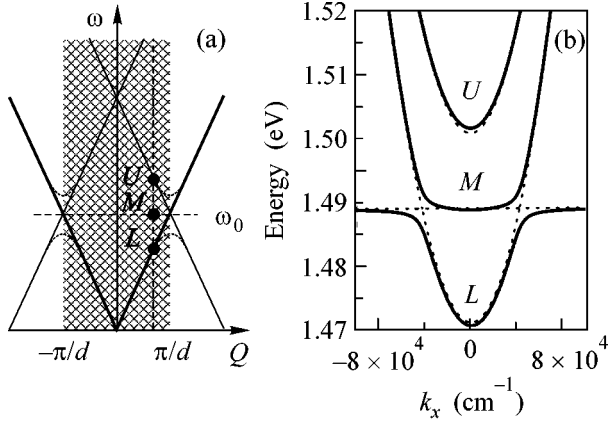


Fig. 1. (a) The scheme showing the dispersions of polaritons in PQW structures. In the infinite periodic structures, the polariton dispersions in the PQW growth direction (dotted lines) are constructed from the photon dispersions (bold lines), their replicas (thin lines), and exciton dispersion (dotted line). The polariton branches obey Eq. (2). The transition from an infinite to finite number of QWs, N , corresponds to the transition from continuous Q to discrete modes. For large N , the energies of the discrete modes (dots) fall on the continuous branch dispersions at $Q_j = \frac{\pi j}{dN}$,

$j = 1, \dots, N$ (vertical dashed line). (b) An example of in-plane dispersions of polariton mode branches calculated using Eq. (2). Dotted lines represent dispersions of the exciton and standing waves of light. The polariton mode dispersions (solid lines) are formed by anticrossing dispersions of the exciton and photon.

the cooperative emission from radiatively coupled QWs, i.e., by polaritonic states. Radiative coupling of the QWs occurs without any external coherent excitation.

The non-AR-coated PQW sample (DBR28) contains $N = 100$ 8.5-nm-thick $\text{In}_{0.04}\text{Ga}_{0.96}\text{As}$ QWs between GaAs barriers (for details, see [12]). The use of low-In-concentration QWs ensures that the background refractive indices of the well and barrier are nearly identical, thereby eliminating the photonic band gap arising from a distributed Bragg-mirror-like reflectivity. A decrease in flux with increasing radius during the growth on a rotating substrate provides an experimental way to continuously scan d . For cw PL studies, the excitation was provided either by an HeNe laser (excitation energy $\hbar\omega = 1.96$ eV) or by a Ti : sapphire laser. The excitation was focused to a 50- μm spot. Experiments were performed in a He_4 cryostat at $T = 1.5$ K.

The theoretical analysis of the polariton mode dispersion is based on the transfer-matrix approach that describes light propagation through a multilayer structure by solving the Maxwell wave equation including the corresponding boundary condition at each interface (LDT). According to [5, 9], the eigenmodes of the self-consistently coupled light-QW-exciton system in an infinite PQW structure obey the dispersion relation

$$\cos(Qd) = \cos(k_z d) - \frac{\Gamma_0 k/k_z}{\omega_0 - \omega - i\Gamma} \sin(k_z d), \quad (1)$$

where Q is the wave vector of light along the PQW growth direction reduced to the first Brillouin zone, $k = \omega/\hbar c$, $k_z = \sqrt{\epsilon_b k^2 - k_x^2}$, k_x is the in-plane polariton wave vector, ω_0 is the exciton resonance energy, and Γ_0 and Γ are, respectively, the radiative and nonradiative exciton damping constants in a single QW. As was shown in [9], for finite number N of QWs, the eigenmodes correspond to the discretized values of the complex wave vector Q . For large N , the values of wave vector tend to become real and equally spaced, and Eq. (1) transforms to

$$\cos(Q_j d) = \cos(k_z d) - \frac{\Gamma_0(\omega_0 - \omega)k/k_z}{(\omega_0 - \omega)^2 + \Gamma^2} \sin(k_z d), \quad (2)$$

where $Q_j = \frac{\pi j}{dN}$, $j = 1, \dots, N$. The roots of Eq. (2) $\omega = \omega(j, k_x)$ correspond to the eigenenergies of the polariton modes. The polariton energies also tend to become real for large N and, therefore, since the imaginary part of energies yields the radiative width of PQW polaritons, polariton states become stationary in the high- N limit, similar to bulk polaritons [7, 9].

The origin of polariton modes in PQW structures can be understood with the schemes shown in Fig. 1. Figure 1a schematically shows the dispersion of polaritons in the PQW growth direction. For infinite N , the polariton dispersions are constructed from the photon dispersions, their replicas, and exciton dispersion. We concentrate below on the energy region close to the exciton resonance. Around ω_0 , there are three PQW polariton branches originating from the folded photon dispersion and exciton dispersion: the upper (U), the middle (M), and the lower (L) one. The splitting between the branches at the anticrossing point at $Q = \pi/d$, proportional to the electromagnetic coupling between the photon and exciton, is small compared to ω_0 and is exaggerated in Fig. 1a. For finite and large N , the energies of the discrete modes fall on the continuous branch dispersions at the momenta $Q_j = \frac{\pi j}{dN}$, $j = 1,$

\dots, N for the j th polariton mode; i.e., the continuous branch and discrete modes obey Eq. (2) with the same r.h.s. We mark the upper j th mode as U_j and so on. Figure 1a presents the case of a Bragg structure with $d = \lambda/2$, i.e., with $\omega_0 = \pi c/d\sqrt{\epsilon_b}$; the modification of the scheme for different d is straightforward. An example of the in-plane dispersions for U , M , and L polariton branches is shown in Fig. 1b. The dispersions were calculated using Eq. (2) for $d/\lambda = 0.501$, $Q_j = 0.99\pi/d$, and $\Gamma_0 = 20 \mu\text{eV}$. The polariton modes are formed by the anticrossing dispersions of the exciton and standing waves of light (Fig. 1b). Note that the mode M_N is a

standing wave with a field $E(z) \propto \sin(\pi z/d)$ with nodes at every QW position $\forall d$ and $\forall k_x$, and its optical transition matrix element is zero.

Figure 2a shows the cw spectra of PL emitted in the direction normal to the PQW structure. Spectra are taken from different positions on the sample corresponding to different periods d , as labeled in Fig. 2a. Figures 2b and 2c present the measured PL energy and intensity of polariton modes at $k_x = 0$ corrected for the exciton energy shift due to a change in the QW thickness. The radiative mode splitting well exceeds the inhomogeneous exciton linewidth. The solid and dashed lines show positions of the eigenmodes at $k_x = 0$ calculated using Eq. (2). The best agreement between the experiment and Eq. (2) is achieved using $\Gamma_0 = 20 \mu\text{eV}$ (dashed lines). The linear fit to the HWHM of reflectivity spectrum vs. N gives $\Gamma_0 = 27 \mu\text{eV}$ [12]. The eigenmodes calculated using Eq. (2) with $\Gamma_0 = 27 \mu\text{eV}$ are also shown in Fig. 2b. All polariton modes observed in the experiment are clearly classified. This confirms that the QW number $N = 100$ is large enough to validate the approximation of Eq. (2) with real and equally spaced Q_j [9].² Figure 2c shows eigenmodes (solid lines), reflection dips (triangles), and absorption peaks (squares) calculated for $N = 100$ PQW using the Lorentzian excitonic susceptibility within an LDT approach [12]. Here, the absorption A is defined as $A = 1 - R - T$, where R is the reflection and T is the transmission. The best agreement between the experiment and the theory is achieved with $\Gamma_0 = 27 \mu\text{eV}$, in agreement with [12]. As expected, PL clearly follows the absorption; thus, the results of the LDT calculations are in good agreement with the experiment.

To measure the dispersion of the PQW polariton modes, we studied angularly resolved PL following experiments in [15], where this method was applied to study the dispersion of polaritons in MCs. The dispersions of polariton modes are revealed via their PL energy vs. $k_x = k \sin \phi$ dependence, where ϕ is the external angle between the emitted photon and the direction normal to the PQW structure. The measured dispersions of polariton modes are presented in Fig. 3. The dashed lines show positions of the eigenmodes calculated using Eq. (2). Dispersions of the polariton modes numerically calculated using LDT for 100 QWs (open squares) are in good agreement with the experimental data (Fig. 3). The calculation based on Eq. (2) has no fitting parameter and uses the value of Γ_0 obtained from the fit to the experimental data in Fig. 2. The main result of the polariton dispersion measurements is that the polariton effective masses are very small. In particular, for the mode M_{N-1} , $m \approx 5 \times 10^{-4} m_0$, they are close to the

² The calculation of the complex wave vectors Q by using the transfer matrix of a finite 100-QW structure [9] shows that there is a finite imaginary part for periods where the corresponding mode is bright. This implies that the large- N approximation is not validated over the whole range of periods.

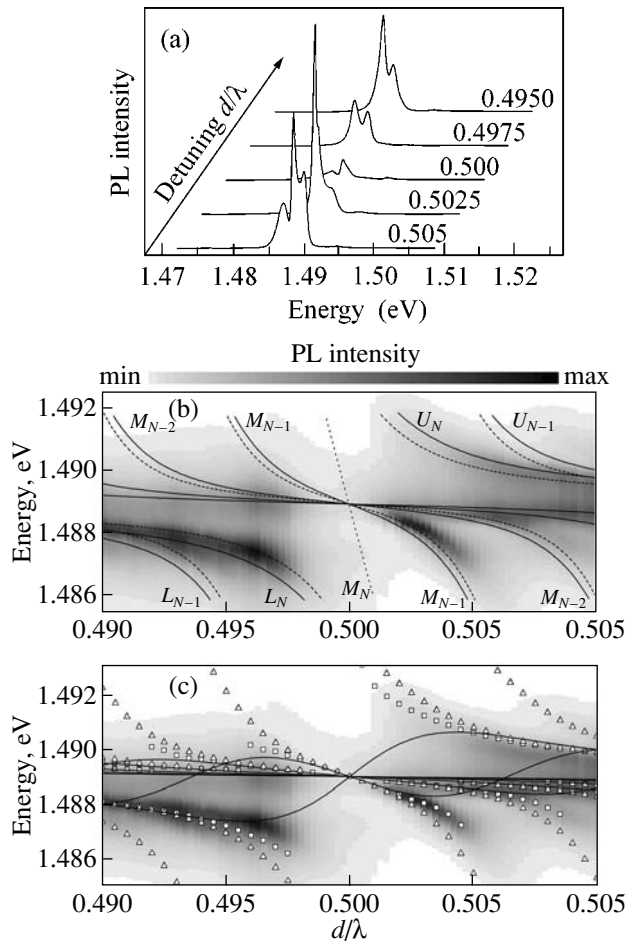


Fig. 2. (a) PL spectra in the normal direction in the reflection geometry for the non-AR-coated $N = 100$ $\text{In}_{0.04}\text{Ga}_{0.96}\text{As}/\text{GaAs}$ PQW structure under cw nonresonant excitation at 1.96 eV. Spectra are taken from different positions on the sample corresponding to different periods d ; $T = 1.5$ K. Poor emission in the normal direction at Bragg resonance, $d = \lambda/2$, reveals the vanishing overlap between the QW excitons and the standing wave of light. (b) The measured PL energy and intensity of polariton modes vs. d (grayscale map). The mode energies calculated using Eq. (2) with $\Gamma_0 = 20 \mu\text{eV}$ ($\Gamma_0 = 27 \mu\text{eV}$) are shown by dashed (solid) lines. The mode classification includes the branch U , M , or L index and the $j = 1, \dots, N$ number (Fig. 1). The optically inactive M_N mode is absent in the PL spectra. (c) Absorption peaks (squares), reflection dips (triangles), and eigenenergies (solid lines) calculated using LDT through a finite non-AR coated 100 QW structure. Note that the functional dependence of A on the period is different for an AR-coated structure.

effective mass of microcavity polaritons. This agreement is natural, because the polariton dispersions are determined by the anticrossing dispersions of an exciton and standing waves of light both for PQWs and MCs. Note that small density-of-states effective mass [$1/m = 2/\hbar^2 \partial E / \partial (k^2)$] is characteristic of most of the polariton modes (Fig. 3).

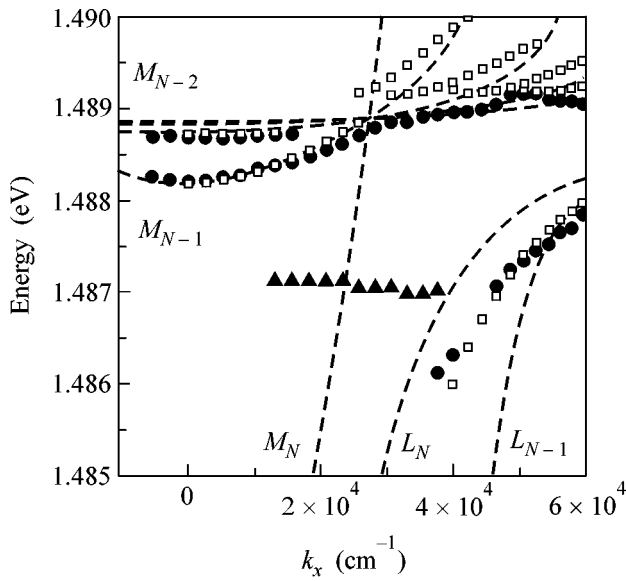


Fig. 3. Measured PL energy of polariton modes (solid points) in non-AR coated $N = 100$ $\text{In}_{0.04}\text{Ga}_{0.96}\text{As}/\text{GaAs}$ PQW structure with $d = 0.5025 \lambda$ vs. k_x under cw nonresonant excitation at 1.495 eV; $T = 1.5$ K. Triangles correspond presumably to the PL of localized states. The mode energies calculated using Eq. (2) with $\Gamma_0 = 20 \mu\text{eV}$ are shown by dashed lines. The polariton effective masses are extremely small; e.g., the quadratic fit to the mode M_{N-1} dispersion at small k_x yields $m \approx 5 \times 10^{-4} m_0$. The calculated absorption peaks using a Lorentzian excitonic susceptibility for the propagation through a 100-QW non-AR coated PQW structure with $\Gamma_0 = 27 \mu\text{eV}$ are shown by open squares.

We notice that the linewidth of the polariton PL from the $N = 100$ PQW sample is sometimes narrower than the linewidth of exciton PL from SQWs grown under as nearly as possible identical conditions. The smallest PL linewidth, ≈ 0.15 meV, observed in $N =$

100 PQW at $d \approx 0.5025 \lambda$ is ≈ 4 times narrower than the exciton PL linewidth in the SQWs. The effect of line narrowing due to the radiative coupling between the QWs clearly dominates over the broadening effects originating from the inhomogeneities of QW thickness, etc.

This work was supported by the Russian Foundation for Basic Research, INTAS (YSF no. 01/2-50), NSF AMOP, JSOP (AFOSR and ARO), and COEDIP.

REFERENCES

1. For a review, see G. Khitrova, H. M. Gibbs, F. Jahnke, *et al.*, *Rev. Mod. Phys.* **71**, 1591 (1999).
2. E. Yablonovitch, *Phys. Rev. Lett.* **58**, 2059 (1987).
3. A. L. Ivanov, P. B. Littlewood, and H. Haug, *Phys. Rev. B* **59**, 5032 (1999).
4. L. V. Keldysh, *Superlattices Microstruct.* **4**, 637 (1988).
5. E. L. Ivchenko, *Fiz. Tverd. Tela (St. Petersburg)* **33**, 2388 (1991) [*Sov. Phys. Solid State* **33**, 1344 (1991)].
6. L. C. Andreani, *Phys. Lett. A* **192**, 99 (1994).
7. D. S. Citrin, *Solid State Commun.* **89**, 139 (1994).
8. E. L. Ivchenko, A. I. Nesvizhskii, and S. Jorda, *Fiz. Tverd. Tela (St. Petersburg)* **36**, 2118 (1994) [*Phys. Solid State* **36**, 1156 (1994)].
9. L. C. Andreani, *Phys. Status Solidi B* **188**, 29 (1995).
10. V. P. Kochereshko, G. R. Pozina, E. I. Ivchenko, *et al.*, *Superlattices Microstruct.* **15**, 471 (1994).
11. M. Hübner, J. Kuhl, T. Stroucken, *et al.*, *Phys. Rev. Lett.* **76**, 4199 (1996).
12. M. Hübner, J. P. Prineas, C. Ell, *et al.*, *Phys. Rev. Lett.* **83**, 2841 (1999).
13. J. P. Prineas, J. Shah, B. Grote, *et al.*, *Phys. Rev. Lett.* **85**, 3041 (2000).
14. B. Grote, C. Ell, S. W. Koch, *et al.*, *Phys. Rev. B* **64**, 045330 (2001).
15. R. Houdre, C. Weisbuch, R. P. Stanley, *et al.*, *Phys. Rev. Lett.* **73**, 2043 (1994).

Realization of the Quantum Fourier Transform and Simulation of a Wave Function on a Quantum Computer with Fixed Continuous Interaction

Yu. Ozhigov

Institute of Physics and Technology, Russian Academy of Sciences, Nakhimovskii pr. 34, Moscow, 117218 Russia

e-mail: ozhigov@ftian.oivta.ru

Received April 1, 2002; in final form, October 21, 2002

A model of a quantum computer with diagonal continuous interaction between qubits is proposed. Such a computer is controlled only by short single-qubit operations. The realization of quantum Fourier transform and simulation of the wave function of a many-particle problem with linear and quadratic potentials on this quantum computer are discussed. This method applies to a wide class of diagonal interactions and to the case, where the interactions of different qubits are different. © 2002 MAIK “Nauka/Interperiodica”.

PACS numbers: 03.67.Lx

1. Quantum computing is an unprecedented test for modern physics, because it requires a level of controlling the behavior of nano-objects that has not been achieved before. Whereas the mathematical theory of quantum calculations is well developed, their physical realizations present a serious challenge to our understanding of the nature. For this reason, it is important to search for such simple realizations of quantum algorithms that are associated with simple technology problems. A computational unit—qubit—is usually represented as a certain characteristic, e.g., spin, charge, or position of some elementary particle.

Two-qubit transformations, which are of fundamental importance for quantum algorithms, are technically very difficult. To realize such a transformation, one must control the degree of entanglement of particles, which is determined by the overlap of the spatial parts of their wave functions. On the other hand, particles participating in calculations must be clearly distinguished, which is possible only if the overlap of their wave functions is sufficiently small. These requirements on the physical realization of quantum calculations are contradictory. In any case, two-qubit transformations are much more difficult than single-qubit ones.

It is reasonable to propose the following approach. Since the interaction between particles with a change in the degree of entanglement follows from the wave equation, two-qubit transformations accompany the natural time evolution of a quantum system. This system can be controlled by single-qubit transformations, which are easily inspected. Thus, calculations will be carried out through acting on the system only by single-qubit pulses, whereas two-qubit transformations will proceed in the background mode and will be uncontrolled. This is the essence of the proposed computa-

tional model with single-qubit control. This model is much more realistic than the abstract quantum computer scheme implying control through two-qubit interaction. Below, this model will be applied to simulate the behavior of a many-particle system with the quadratic interaction specified by a diagonal matrix.

The basic problem in this model with single-qubit control is that two-qubit interaction proceeds uncontrollably, in particular, with irrelevant qubits, which seriously distorts quantum algorithms. Calculations in this model require methods of correcting undesirable transformations by means of single-qubit pulses. To demonstrate the capabilities of this approach, we first apply this model to realize the quantum Fourier transform. Our basic assumption is that the Hamiltonian matrix of two-qubit interaction is diagonal. For convenience and simplicity, we first additionally assume that this interaction decreases with distance as the Yukawa potential.

2. Realization of quantum Fourier transform with single-qubit control. The quantum Fourier transform is the key subroutine in quantum computing, because it is used in many other algorithms [1–3]. Figure 1 shows the simplest scheme of functional elements for realizing this transformation. This scheme was used by Shor for fast quantum factorization [1]. Integer $a = a_0 + a_02 + \dots + a_{l-1}2^{l-1}$ is represented by the basis state $|a_0a_1\dots a_{l-1}\rangle = |a\rangle$. These states form an orthonormalized basis for the input states of the quantum scheme of functional elements. We arrange them from top to bottom. The same convention will be accepted for the output states of the scheme, but bits b_j of the number $b = b_0 + b_02 + \dots + b_{l-1}2^{l-1}$ will be arranged in the reverse order.

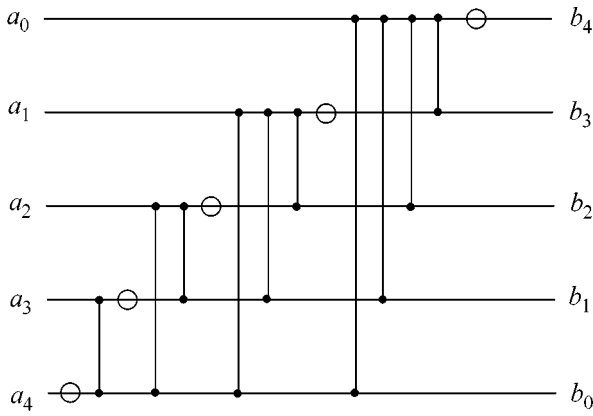


Fig. 1. Quantum scheme of functional elements for the inverse quantum Fourier transform with single- and two-qubit control. Circles are the Hadamard gates, and two-qubit operations have form (1).

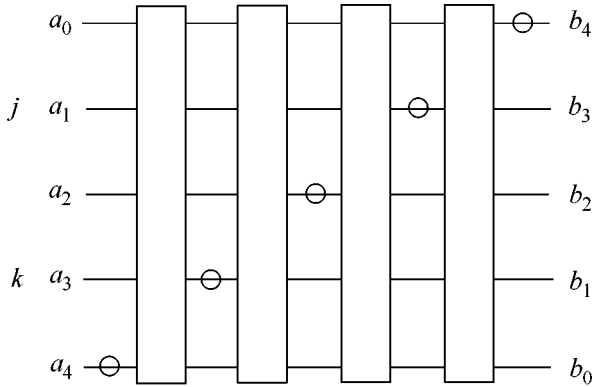


Fig. 2. Scheme for the inverse quantum Fourier transform with continuous interaction given by Eq. (1a) and shown by the rectangles. Circles are the Hadamard gates.

This scheme realizes the inverse quantum Fourier transform in $O(l^2)$ steps, whereas the dimension of the transformation matrix is equal to $N = l^2$. However, this scheme requires two-qubit control and cannot, therefore, be realized directly in the model under consideration. Below, we demonstrate how it can be realized. Let us consider interactions of the form

$$H = \begin{pmatrix} 0 & 0 & 0 & 0 \\ 0 & 0 & 0 & 0 \\ 0 & 0 & 0 & 0 \\ 0 & 0 & 0 & \rho \end{pmatrix}, \quad \rho > 0, \quad (1a)$$

and

$$H = \begin{pmatrix} \rho_1 & 0 & 0 & 0 \\ 0 & \rho_2 & 0 & 0 \\ 0 & 0 & \rho_3 & 0 \\ 0 & 0 & 0 & \rho_4 \end{pmatrix}. \quad (1b)$$

Here, ρ and ρ_i ($i = 1, 2, 3, 4$) have the form $\rho = \rho_0(e^{-br/r})$, where $b = \text{const}$ and r is the separation between qubit particles, and $\rho_1 + \rho_4 \neq \rho_2 + \rho_3$. We arrange l qubits equidistantly in one line. Let the interaction between qubits j and k be specified by the Hamiltonian $H_{j,k}$ given by Eqs. (1). Such Hamiltonians arise, for example, in the Ising model for spin-1/2 particles. The required decrease in interaction with increasing distance can be achieved by putting qubits in a suitable potential well. Taking an appropriate length unit, we can have $b = 1$. We first examine interaction given by Eq. (1a) and then expand the results to case (1b).

2.1. Realization of the quantum Fourier transform without regard for the phase shift. Let the quantum Fourier transform and inverse quantum Fourier transform have the form

$$\begin{aligned} \text{QFT: } |a\rangle &\rightarrow \frac{1}{\sqrt{N}} \sum_{b=0}^{N-1} e^{\frac{2\pi iab}{N}} |b\rangle, \\ \text{QFT}^{-1}: |a\rangle &\rightarrow \frac{1}{\sqrt{N}} \sum_{b=0}^{N-1} e^{-\frac{2\pi iab}{N}} |b\rangle, \end{aligned} \quad (2)$$

respectively. In this case, the inverse transform can be realized by using scheme shown in Fig. 2, where the rectangles are unitary transformations $U = e^{-i\tilde{H}}$ with $\tilde{H} = \sum_{l>j>k\geq 0} \tilde{H}_{j,k}$, where each $\tilde{H}_{j,k}$ is given by Eq. (1a)

with $\rho_0 = \pi$ and $r = j - k$. If the time unit is chosen so that the product of Plank's constant by ρ_0 is equal to π , and the length unit is chosen so that $r = j - k$, U is such transformation of the state vector that is induced by the Hamiltonian under consideration per unit time. Here, it is assumed that single-qubit operations take negligibly short time compared to unity, so that interaction between qubit pairs cannot strongly change the phase during this time. To demonstrate that this scheme really realizes the inverse quantum Fourier transform, we apply the method for calculating amplitudes proposed by Shor in [1]. The output state corresponding to a given basis input state $|a\rangle$ is a linear combination of the basis states $|b\rangle$ with some amplitudes. All absolute values of these amplitudes are equal to $1/\sqrt{L}$, and it is sufficient to control their phases. For simplicity, we introduce the notation $a'_j = a_{l-1-j}$, $j = 0, 1, \dots, l - 1$. In the process of applying our scheme, qubit values with numbers j and $k \leq j$ pass from left to right through the elements shown in Fig. 2. Following this direction, we will take four types of interactions: (i) self-interaction of a'_j and a'_k in the Hadamard operation, (ii) interaction between a'_j and a'_k ($j > k$), (iii) interaction between a'_j and b_k ($j > k$), and (iv) interaction between b_j and b_k ($j > k$) with times 0, k , $j - k$, and $l - 1 - j$, respectively.

The resulting phase is the following sum of the contributions of these interactions:

$$\begin{aligned} & \pi \sum_{l>j>k\geq 0} \frac{a'_j a_k k}{2^{j-k}(j-k)} + \pi \sum_{l>j>k\geq 0} \frac{a'_j b_k (j-k)}{2^{j-k}(j-k)} \\ & + \pi \sum_{l>j\geq 0} a'_j b_j + \pi \sum_{l>j>k\geq 0} \frac{b_j b_k (l-j-1)}{2^{j-k}(j-k)}. \end{aligned} \quad (3)$$

In what follows, the first and last terms will be denoted as A and B , respectively. Their contribution corresponds to the action of the diagonal Hamiltonians on $|a\rangle$ and $|b\rangle$, respectively. After change j to $l-1-j$, the sum of the second and third terms takes the form

$$\begin{aligned} & \pi \sum_{l-1>k+j\geq 0} \frac{a_j b_k 2^{j+k}}{2^{l-1}} + \pi \sum_{l-1\geq j\geq 0} a_{l-1-j} b_k \\ & = 2\pi \sum_{l>k+j\geq 0} \frac{a_j b_k 2^{j+k}}{2^l} \\ & = 2\pi S + 2\pi \sum_{l>k, j\geq 0} \frac{a_j b_k 2^{j+k}}{2^l} = 2\pi S + 2\pi \frac{ab}{2^l}, \end{aligned} \quad (4)$$

where S is an integer. The first term does not change its phase, and we obtain the desired result without regard for the contributions A and B .

2.2. Correction of the phase shift. The contribution of diagonal terms A and B to the phase is calculated as follows. We first consider only term A , which consists of terms $A_{j,k} = c_{j,k} a'_j a'_k$, where $c_{j,k}$ depends only on j and k but is independent of a . In order to suppress all interactions except for the interaction between selected qubits, single-qubit NOT transformation will be applied several times to all qubits excepting selected qubits j and k .

We first consider a pair of unselected qubits with numbers p and q such that $q > p$. Their continuous interaction during time interval Δt provides the term $d_{p,q} \Delta t a'_p a'_q$ in the phase, where $d_{p,q}$ depends only on the degree of a decrease in interaction with increasing distance but is independent of a'_p and a'_q . In particular, for a Yukawa-type decrease, $d_{p,q} = e^{-|q-p|} / |q-p|$. Then, we invert arbitrarily one (let it be q) of these two qubits by applying the NOT operation. Its state becomes $1 - a'_q$. Then, the second interval Δt of continuous interaction introduces term $d_{p,q} \Delta t a'_p (1 - a'_q)$ to the phase. Finally, we recover the content of qubit q by applying the second NOT operation. The resulting phase shift in these four actions is equal to $d_{p,q} \Delta t a'_p$ and depends only on the content of qubit p .

Now, we can compensate this phase shift by one single-qubit transformation. Interaction between a pair of

qubits p and q , one of which (let it be p) is selected and the other is unselected, can be compensated by using only single-qubit operations, namely, two NOT operations for q and a certain phase shift for p .

Next, this method should be modified to simultaneously compensate for all effects of the unselected qubits. For this purpose, we apply the NOT operations to each such qubit with sufficiently short intervals so that the contributions from the unselected qubits to the phase cancel each other. This can be made by two methods: single-qubit operations are applied either at randomly generated times or periodically with different periods for different qubits. Let us discuss the first approach.

2.3. Compensation of the phase shift. For each unselected qubit p , we consider a Poisson process \mathcal{A}_p generating times $0 < t_1^p < t_2^p < \dots < t_{m_p}^p < 1$ with a certain fixed density $\lambda \gg 1$. Let all \mathcal{A}_p be independent. Then, the NOT operations are applied to each qubit p sequentially at times t_m^p . At time 1, the NOT operation is applied to qubit p , if and only if m_p is odd. Thus, each qubit recovers its initial state after this procedure. Interactions between the selected qubits remain unaffected. Let us calculate the contribution from a certain unselected qubit to the phase. This contribution consists of two terms corresponding to the interactions with selected and unselected qubits, respectively. We will calculate them sequentially.

(i) Since the density λ of Poisson process \mathcal{A}_p is high, qubit p is in the state a'_p for about half the time and in $1 - a'_p$ for the remaining half. The interaction of this qubit with some selected qubit j makes the contribution $\frac{1}{2} d_{p,j} a'_p a'_j + \frac{1}{2} d_{p,j} (1 - a'_p) a'_j$, i.e., $\frac{1}{2} d_{p,j} a'_j$.

(ii) Let us consider different unselected qubits $q \neq p$. Since the NOT operations are applied to qubits p and q at independent times and the density λ is high, these qubits are in each of states (a'_p, a'_q) , $(a'_p, 1 - a'_q)$, $(1 - a'_p, a'_q)$, and $(1 - a'_p, 1 - a'_q)$ for about quarter the time.

The resulting contribution is equal to $\frac{1}{4} d_{p,q} [a'_p a'_q + a'_p (1 - a'_q) + (1 - a'_p) a'_q + (1 - a'_p) (1 - a'_q)] = \frac{1}{4} d_{p,q}$.

The total phase shift from the unselected qubits is the following sum of values from (i) and (ii) for all $p \notin \{j, k\}$:

$$\frac{1}{2} \left[\sum_{p \notin \{j, k\}} d_{p,j} a'_j + \sum_{p \notin \{j, k\}} d_{p,k} a'_k \right] + \frac{1}{4} \sum_{p, q \notin \{j, k\}} d_{p,q}$$

This shift can be compensated by single-qubit transformations, because the first two terms depend only on the values of qubits, and the remaining terms are constants.

Thus, we construct the scheme with continuous two-qubit interaction and single-qubit operations that gives phase shift $d_{j,k}a'_ja'_k$. Taking the time interval Δt as a time unit in this procedure, we obtain phase shift $\Delta t d_{j,k}a'_ja'_k$. In order to obtain shift $-\Delta t d_{j,k}a'_ja'_k$, we must first apply the NOT operation to qubit j , carry out the above procedure, apply the NOT operation to qubit j , and add $-\Delta t d_{j,k}a'_k$ by the single-qubit operation. Thus, we can make any addition of the form $ca'_ja'_k$ to the phase, where c is any real number. The appropriate combination of these schemes gives the phase shift

$$\sum_{j,k} c_{j,k} a'_j a'_k \quad (5)$$

for any $c_{j,k}$. Performing these operations before and after the inverse quantum Fourier transform in the procedure discussed in the preceding section, we compensate terms A and B in the phase and obtain the scheme realizing the inverse quantum Fourier transform.

Let us estimate the delay caused by the introduction of the NOT operations with a high density compared to the abstract realization of quantum algorithms on the schemes based on functional elements. We fix the time unit so that one operation in the scheme takes unit time. The NOT operation can be applied with identical short time intervals δt , i.e., at times $k\delta t$ for any integer k with probability $p = 1/\lambda$, where λ is the density of the process. We denote $M = T/\delta t$, where T is the computational time. The error of phase shift caused by the possible imperfection of the random process in this model is equal to $\delta t D$, where D is the variance of the sum of random variables taking values 1 and 0 with the respective probabilities p and $1 - p$, i.e., $O(\sqrt{M})$. Therefore, the resulting error is equal to about T/\sqrt{M} and must be negligibly small. For the quantum Fourier transform, $T = O(\ln N)$, and $M = O(\ln^2 N/\epsilon)$ will be sufficiently large for negligibly small ϵ . Thus, the method of random processes results in a delay that is slightly larger than the quadratic delay, as compared to the standard model, and this is quite admissible for fast algorithms such as quantum Fourier transform. Applying the modifications of the above method to slower quantum algorithms such as the Grover algorithm [7], one must use the method of periodic NOT operations rather than the method of random processes. In this model the NOT transformations are applied to each of qubits j at times $jk\delta t$ for integer k , where δt is the short time interval. In this case, we can repeat the above construction and remove undesirable phase shifts by appropriately choosing δt . This method results in a delay in the form of a factor of about n^2 , as compared to the complexity of the abstract model of quantum functional schemes.

3. Possibility of using various interactions. The proposed technique is easily extended to the general

case of Hamiltonian given by Eq. (1a) with an arbitrary decrease; i.e., the phase shift of form (5) can be generated in this model, and

$$\sum_{l>j>k\geq 0} c_{j,k} a'_j b_k \quad (6)$$

for any $c_{j,k}$.

The application of interaction (1b) per unit time gives phase shift $\rho_1(1 - a'_j)(1 - b_k) + \rho_2(1 - a'_j)b_k + \rho_3 a'_j(1 - b_k) + \rho_4 a'_j b_k$, which can be reduced to the preceding case through the linear shift, because $\rho_1 + \rho_4 \neq \rho_2 + \rho_3$.

Finally, this technique can be directly generalized to the Hamiltonians that can be diagonalized by single-qubit operations.

4. Simulation of physics by continuous interactions. We discuss now an important Feynman's idea [4] of simulating many-particle physical problems on a quantum computer. Zalka [5] and Wiesner [6] proposed the scheme implementing this idea on the basis of the Coppersmith–Deutsch–Shor (see Fig. 1) method for inverse quantum Fourier transform. The method proposed above for realizing the quantum Fourier transform with single-qubit control provides a simple way to simulate the wave function of many-particle problems with linear and quadratic potentials. The corresponding Hamiltonian for s_1 particles has the form

$$H = \sum_{k=1}^s \frac{p_k^2}{2m_k} + \frac{1}{2} \sum_{j,k=1}^s v_{j,k} q_j q_k, \quad (7)$$

where $s = 3s_1$ is the total number of spatial coordinates q_k determining the particle positions, p_k are the momenta, and $v_{j,k}$ are the constants determining the interaction potentials. We will discuss the case $k = 1$, because the general case is fully similar.

It is necessary to approximate the action of operation e^{-iHt} on the wave function ψ_0 , where $H = H_p + H_q$, $H_p = p^2/2m$, $H_q = V(q)$, $p = i^{-1}(\partial/\partial q)$, and potential $V(q)$ is a real quadratic function. Without loss of generality, we can take $t = 1$. A suitable approximation can be obtained in the coordinate or momentum basis of the space of state vectors, and the Hamiltonian is nondiagonal in both bases. To reduce the problem to diagonal Hamiltonians, we take short time interval Δt and represent our time evolution operator in the approximate form

$$e^{-iH} \approx (e^{-iH_q \Delta t} e^{-iH_p \Delta t})^{1/\Delta t}. \quad (8)$$

For example, H_q has the diagonal form in the coordinate basis. Using Fourier transform $f \rightarrow$

$\frac{1}{\sqrt{2\pi}} \int_{-\infty}^{+\infty} e^{-ipq} f(q) dq$, which changes differentiation $\partial/\partial q$ to multiplication by ip , we can represent the action

of the momentum part of the operator as $e^{-iH_p} = \text{FT}^{-1} e^{-ip^2\Delta t/2m}$, where the operator in the middle is diagonal. If the Fourier transform and phase shift $-p^2/2m$ can be realized, the sequential application of such operators from Eq. (8) yields the necessary approximation.

Let the wave function $\psi(q)$ and its momentum representation $\text{FT}(\psi)$ be defined in segments $(-A, A)$ and $(-B, B)$, respectively. Taking small Δq and Δp values, we can approximate this function through

$$\sum_{a=0}^{2A/\Delta q} \psi(q_a) \delta_a,$$

where $\delta_a(q)$ takes the values 1 and 0 on the segment $(q_a, q_a + \Delta q)$ and outside it, respectively. In this case, the Fourier transform can be approximated by the linear operator, whose action on δ_a yields

$$\frac{1}{\sqrt{2\pi}} \Delta q \sum_{b=0}^{2B/\Delta p} e^{-ip_b q_a} \sigma_b(p),$$

where $\sigma_b(p)$ is the one-step momentum function similar to δ_a . Introducing new one-step coordinate and momentum functions as $d_a(q) = \delta_a(q - A)$ and $s_b(p) = \sigma_b(p - B)$, we write the Fourier transform in the form

$$d_a \longrightarrow \frac{1}{\sqrt{2\pi}} \Delta q \sum_{b=0}^{2B/\Delta p} e^{-iba\Delta q\Delta p} s_b, \quad (9)$$

which is very similar to the quantum Fourier transform.

Let us assume that the physical space is grained in the coordinate and momentum representations with grain sizes Δq and Δp , respectively. In this case, the particle under consideration can be located only at points q_a or have only momenta p_b . We associate position q_a , $a = 0, 1, \dots, N = 2^l$ with the basis state $|a\rangle$ in the l -qubit quantum system. For simplicity, we choose the length unit so that $\Delta q = \Delta p = \sqrt{2\pi}/\sqrt{N}$ and $A = B = \sqrt{\pi N/2}$. In this case, Eq. (9) corresponds to the quantum Fourier transform given by Eq. (2), and the phase shift $-p^2\Delta t/2m$ from Eq. (8) corresponds to the phase shift $-\pi b^2\Delta t/mN$. Both operations can be realized by continuous interaction with single-qubit control, because they have the necessary form. Finally, the first of operators (8) can be realized similarly.

When simulating an ensemble of s_1 particles, we must take s_1 copies of quantum register for one particle and perform the above procedure for the united quantum memory.

5. Advantages of the quantum simulation of wave functions. The method proposed above for the quantum simulation of wave functions retains all advantages of the quantum solution proposed for Schrödinger equation in [1, 5, 6]. Namely, this method of realizing the quantum Fourier transform takes time $O(l^2)$ for a

given interaction between qubits. If this operator is used in the approximate form obtained by omitting exponentially small phase shifts, the corresponding modification of the proposed method takes time $O(l)$, with the constant depending on a chosen accuracy.

The main advantage of this method, as applied to the simulation of wave functions, is manifested in many-particle problems. The wave function of a system of s one-dimensional particles at a fixed time has the form $\Psi(x_1, x_2, \dots, x_s)$, where x_j is the coordinate of the j th particle. To store the approximation of this function with grain ϵ and arguments limited by b , the memory of N^ϵ bits is required, where $N = b/\epsilon$. At the same time, the quantum simulation method requires about $\ln N$ qubits for each particle, and the total required memory equals $s \ln N$ qubits, which is equal to almost the logarithm of classical memory.

6. The model of a quantum computer controlled by only single-qubit operations with uncontrolled continuous diagonal two-qubit interaction has been proposed. The simplicity of control is the advantage of this model. The simple method of realizing the quantum Fourier transform and simulating many-particle problems with quadratic potentials has been proposed in this model. Such a quantum computer can simulate free fields and particles, states of a set of harmonic oscillators, and the behavior of complex polyatomic molecules.

It would be important to generalize the proposed method to nondiagonal Hamiltonians. Finally, it would be interesting to select the computational quantum-mechanical problems, where quantum calculations with the qubit representation of wave functions could be effective. For example, such a reformulation implies the presence of a spatial grain, and the traditional field-theory problem of series divergence at high energies will thus be removed. This qubit reformulation generally seems to be more efficient, because it requires memory that increases linearly rather than exponentially with an increase in the number of particles, as in the convenient description of wave functions.

REFERENCES

1. P. W. Shor, *SIAM J. Comput.* **26**, 1484 (1997); lanl e-print quant-ph/9508027.
2. D. S. Abrams and S. Lloyd, lanl e-print quant-ph/9807070.
3. Y. Ozhigov, lanl e-print quant-ph/0201132.
4. R. Feynman, *Int. J. Theor. Phys.* **21**, 467 (1982).
5. C. Zalka, lanl e-print quant-ph/9603026.
6. S. Wiesner, lanl e-print quant-ph/9603028.
7. L. K. Grover, in *Proceedings of STOC* (Philadelphia, PA, USA, 1996), p. 212; lanl e-print quant-ph/9605043.

Translated by R. Tyapaev